Achieving contrapuntal balance at a lake outlet: Restoring salmon spawning habitat with gravel augmentation design

by

Megan Iun

A thesis

presented to the University of Waterloo

in fulfillment of the

thesis requirement for the degree of

Master of Applied Science

in

Civil Engineering (Water)

Waterloo, Ontario, Canada, 2024

© Megan Iun 2024

Author's Declaration

This thesis consists of material all of which I authored or co-authored: see Statement of Contributions included in the thesis. This is a true copy of the thesis, including any required final revisions, as accepted by my examiners.

I understand that my thesis may be made electronically available to the public.

Statement of Contributions

I would like to acknowledge the contributions made by my supervisor Dr. Bruce MacVicar, including his inputs on the design of the tracer study, analysis and interpretation of results, and editorial suggestions.

Elements of the data collection and preparation were completed by staff at Ecofish Research Ltd. Images of the channel collected using a remotely piloted aircraft system was completed by Kelsey Tikka from the University of British Columbia (UBC). These contributions are acknowledged in Chapter 3 where the respective methods are described.

The above notwithstanding, I was the sole author for the results and the final manuscript of this thesis.

Abstract

The degradation of gravel bed rivers in logging and climate-impacted watersheds has led to an increase in salmonid habitat conservation and restoration efforts. Gravel augmentation is one such technique that seeks to restore altered aquatic habitat and sediment transport dynamics in sediment-starved streams by placing gravel pads in the river. The pads act as a sediment source that can be reworked by flow or fauna to suit their ecological needs, thereby allowing the river to "heal" itself without imposing static structural designs on a natural environment. Common points of failure for these projects include: (1) the immediate scour of the gravel pad which can wipe out buried eggs, (2) the infilling of the gravel interstices with fine particles which can limit oxygenated hyporheic flow and choke the buried eggs, and (3) low utilization by the target species due to unsuitable hydraulic conditions for spawning. The risk of the first two hazards can be limited by designing the gravel placements at downstream of lakes, as the upstream lake can buffer peak flows to its outlet stream and trap fine sediment. Much like composing counterpoint in music, a delicate balance is needed between multiple engineering criteria to identify the optimal area along the accelerating channel length where most criteria are fulfilled. Despite this understanding and the common use of lake outlets for these projects in industry, there are few design guidelines tailored for these environments.

This project evaluates the design criteria of a gravel augmentation project for salmon spawning habitat restoration at a lake outlet. A calibrated two-dimensional (2D) hydrodynamic model was developed using TELEMAC-2D. The sediment transport predictions from the model were verified by tracking tracer stones equipped with Radio Frequency Identification (RFID) after one year. The model results were used to identify optimal placement areas.

The 2D model was found to adequately capture the measured depth-averaged velocities when set with appropriate boundary conditions and calibrated with the roughness coefficient. However, the roughness-dependent shear velocity calculation in the model formulation results in a direct dependency of the model outputs on the sole calibration parameter. This relationship is highly sensitive and creates modeling artefacts when using roughness zones to calibrate the model.

The tracer results indicate that the model appears to overpredict sediment transport due to the limitations of the deterministic approach of assessing grain mobility, which is inherently a stochastic process. Although there is likely error associated incorrect assumptions on critical mobility thresholds and representative grain sizes, the relative lack of tracer mobility during the study year limits the

current ability to revise these assumptions. Nevertheless, the results show that the application of 2D hydrodynamic models to sediment transport predictions should be approached with caution and should be accompanied by field validation to ensure confidence in the model conclusions.

Using the model as is, the optimization analysis results suggest that designing to prioritize longevity may require compromising the other design criteria. Conversely, optimizing the design to minimize the risk of fines infilling severely limits the available placement areas. Prioritizing stability may decrease the likelihood of immediate utilization but may be required due to the uncertain availability of funding for re-injecting gravel after the initial construction.

Acknowledgements

During my time at the University of Waterloo, I have lived, worked, and studied on the traditional territory of the Neutral, Anishinaabeg and Haudenosaunee peoples. The University of Waterloo is situated on the Haldimand Tract, the land granted to the Six Nations that includes six miles on each side of the Grand River. Furthermore, the field site for this thesis is located on the unceded and never surrendered territory of the Mowachaht/ Muchalaht First Nation (MMFN). This thesis was completed under a Mitacs Accelerate Fellowship with Ecofish Research Ltd., who are partnering with the Nootka Sound Watershed Society (NSWS) and the MMFN to realize this project. As a settler, it is my hope that this project will contribute to the reclamation of land rights and cultural preservation for the MMFN in this watershed.

This work would not have been possible without the invaluable help from numerous people at the University of Waterloo. I would like to thank my supervisor Dr. Bruce MacVicar for his guidance, support, and mentorship throughout this degree. I would also like to acknowledge Mark Hummel who was very forthcoming with his help when I was assembling the RFID antenna. I would like to extend my gratitude to the past and present members of the River Hydraulics Research Group who I have crossed paths with over my time in this group and who have provided with me help or advice throughout this journey. Of note, thank you to Lukas Mueller and Taylor Kenyon for their help in the field.

I would like to acknowledge Ecofish Research Ltd, who made this research possible by funding the project through a Mitacs partnership and by collecting most of the data used in this thesis. Thank you to David West, Adam Marriner, Pengcheng Li, Daniel Greenacre, Isabelle Girard, Mel Sheng and all the other staff who provided input, expertise or otherwise contributed to the project.

I would like to express my sincere gratitude to everyone who helped with the fieldwork in any capacity—the field staff at Ecofish who helped with collecting and assembling much of the data used to develop the numerical model, Adam from Ecofish and Roger from MMFN who helped us to seed the tracers, and Kelsey Tikka from UBC who helped with finding tracers and flying the drone. All of you were invaluable to the completion of this project. In particularly, I would like to specifically acknowledge Lukas, Kelsey, and Taylor for volunteering their unpaid time to look for rocks in a river while a buzzer incessantly screamed at them. In the same vein, I would like to apologize for

compensating them with only the semblance of a meal at perhaps one of the worst restaurants that any of us has ever experienced.

Finally, I would like to thank my family and friends who mentally and emotionally supported me through this degree. Thank you for showing me love even during the periods when I cannot see a way forward. To all my friends who asked me how my rocks were doing or who used me as a poster child to brag about their friends doing cool things, I appreciate you more than you know. Thank you to my parents who supported my career choices even amidst their constant worry for me. Last but not least, thank you to the Simply Church family who kept me well fed and grounded throughout the last three years with our weekly meals and fellowship.

Table of Contents

Author's Declaration ii

Statement of Contributions iii

Abstract iv

Acknowledgements vi

List of Figures xiii

List of Tables xvii

List of Abbreviations xviii

List of Symbols xxi

Preface 1

Chapter 1 Introduction 2

1.1 Background 2

1.2 Objectives 4

1.3 Research project context 4

1.4 Thesis organization 5

Chapter 2 Literature Review 6

2.1 River restoration 6

2.1.1 Approaches to river restoration 6

2.1.2 Success metrics in process-based restoration 8

2.1.3 Gravel augmentation as a process-based restoration technique 10

2.1.4 Design considerations for gravel augmentation 11

2.2 Salmon spawning habitat 12

2.2.1 Salmon spawning mechanism 13

2.2.2 Salmon spawning habitat quality 13

2.2.3 Geomorphic effects of salmon spawning behaviour 15
2.2.4 Significance of lake outlets for salmon spawning habitat 15
2.3 Hydraulics and sediment transport in accelerating flows 17
2.3.1 Law of the wall and logarithmic velocity profiles under uniform flow 17
2.3.2 Velocity profiles in accelerating flow 18
2.3.3 Reynolds stress 23
2.3.4 Shear velocity 26
2.4 Critical shear stress dependencies 26
2.4.1 Bed slope 26
2.4.2 Bioturbation 27
2.4.3 Epilithic biofilm 28
2.5 Application of numerical models for salmon habitat restoration design 29
2.5.1 Overview of numerical models for hydraulic simulation 29
2.5.2 Applications to salmon habitat restoration 31
2.5.3 Characterizing sediment transport using tracers 32
Chapter 3 Methods 34
3.1 Study area 34
3.1.1 Watershed context 34
3.1.2 Site investigations 35
3.1.3 Study area 36
3.1.4 Hydraulic characteristics 37
3.1.5 Sediment characteristics 37
3.2 Project timeline 38
3.3 Data collection and preparation 39

3.3.1 Discharge 40
3.3.2 Topography 42
3.3.3 Roughness 50
3.3.4 Radio frequency identification tracer stones 52
3.4 Hydrodynamic model 59
3.4.1 TELEMAC-2D 59
3.4.2 Model set-up 60
3.4.3 Model boundary conditions 60
3.4.4 Turbulence model 61
3.4.5 Calibration 61
3.5 Sediment transport model 66
3.5.1 Gravel placement mix 66
3.5.2 Critical shear stress thresholds 67
3.5.3 Shear velocity calculations 69
3.5.4 Critical velocity filters 71
3.5.5 Numerical model validation using tracer stones 72
3.6 Engineering design criteria for spawning gravel enhancement projects 72
3.6.1 Hydraulic habitat suitability index curves 73
3.6.2 Interstitial fines deposition and flushing 75
Chapter 4 Results 76
4.1 Field investigations of sediment transport 76
4.1.1 Existing sediment sources 76
4.1.2 Sediment pathways through a vegetative bed rise 78
4.2 Hydrodynamic model calibration and performance 80

4.2.1 Calibration results for HiFT flow scenario 80
4.2.2 Validation results for the MeFT flow scenario 82
4.3 Sediment transport model 83
4.3.1 Comparison of shear velocity distributions calculation methods 83
4.3.2 Predicted gravel mobility under select design flow rates 85
4.4 Tracer stone recovery 86
4.4.1 Tracer recovery rates 86
4.4.2 Tracer mobility patterns 89
4.4.3 General mobility validation by size class 90
4.4.4 Direct mobility validation by tracer characteristics 91
4.5 Evaluation of engineering design criteria for spawning gravel placement 94
4.5.1 Habitat suitability 94
4.5.2 Fines deposition and flushing 96
4.5.3 Optimal areas for placement 97
Chapter 5 Discussion 100
5.1 Hydraulics 100
5.1.1 Representation of hydraulics in accelerating flow using 2D models 100
5.1.2 Uncertainty on the effect of algal biofilm on hydraulics 101
5.1.3 Uncertainty on the effect of wind-driven currents on hydraulics 102
5.2 Sediment transport 102
5.2.1 Limitations in the classic shear velocity calculation method 102
5.2.2 Proposed method for calculating shear velocity 103
5.2.3 Sensitivity to critical shear stress thresholds 104
5.2.4 Size-dependency for critical shear stress thresholds 104

5.2.5 Implications for engineering applications 107
5.3 Tracer stones 107
5.3.1 Partial tracer mobility 107
5.3.2 Cumulative transport fractions 108
5.3.3 Tracer stone mobility definition 111
5.3.4 Tracer stone monitoring for restoration projects 112
5.4 Uncertainty in the design evaluation 113
5.4.1 Consideration of fines 113
5.4.2 Implications for gravel augmentation at lake outlets 114
5.5 Research gaps for further study 116
Chapter 6 Conclusions 118
6.1 Objective 3: Application of 2D models for lake outlets 118
6.2 Objective 2: Sediment tracer validation 119
6.3 Objective 3: Gravel placement strategy 119
References 121
Appendices 143
Appendix A Additional data and processing 144
Appendix B RPAS Photogrammetry process 148
Appendix C Initial model development and formulation 151
Appendix D Gravel placement scenario 156

List of Figures

Figure 1 Schematic representation of a salmon redd. From Buxton et al. (2015). 13
Figure 2 Progression of velocity profiles transitioning from uniform flow over a smooth horizontal bed to accelerating flow over an inclined plate angled 3º (B, left) and 7º (C, right). From Cardoso et al. (1991). 19
Figure 3 Generalization of velocity profiles in fully turbulent flow. From Sturm (2010). 20
Figure 4 Conceptual model of the dependence of $\boldsymbol{\Pi}$ on $\boldsymbol{\beta}$, $\boldsymbol{Re}$ and $\boldsymbol{b/h}$. From Xiao et al. (2023). 22
Figure 5 Measured Reynolds stress distribution with momentum flux modifications. From Yang and Lee (2007). 25
Figure 6 Site context over a Google Earth basemap. Flow enters the lake through the Oktwanch and Upper Muchalat Rivers and exits through the study site on Lower Muchalat River..... 35
Figure 7 RPAS imagery of the study area (red hatched zone). Water flows left to right. 36
Figure 8 Spatial distribution of substrate in the channel 38
Figure 9 Study timeline, where green represents field trips, blue is modelling and analysis, and purple are items related to reporting. 39
Figure 10 Benchmark locations in the study reach shown in red squares. Flow direction is from left to right, and the two water level gauges are identified with green arrows. 43
Figure 11 (a) Measured WSE and regression lines along the centreline of each section and (b) the approximate spatial extents of each section. 45
Figure 12 Calculated bed elevation from regression WSE and ADCP depth measurements..... 46
Figure 13 Location of ground control points..... 47
Figure 14 Comparison of measured and SfM bed elevations across the Solinst gauge transect..... 49
Figure 15 Example of the substrate photos taken by Ecofish. 51
Figure 16 Grain size distribution at three transects near BMs..... 52
Figure 17 Tracer stone cross-section with a 23 mm RFID PIT tag. 53
Figure 18 Recommended GSD curve for Chinook salmon spawning gravel from Ecofish. 53
Figure 19 Small (a), medium (b) and large (c) tracer stones after preparation..... 54
Figure 20 Tracer stones shape classifications based on Zingg (1935) categories. 55
Figure 21 Top view of the LF HDX Backpack reader. 57
Figure 22 (a) The pre-built loop pole antenna from Oregon RFID and (b) the custom-built flexible antenna..... 58

Figure 23 Roughness zones and corresponding IDs in initial model. 64
Figure 24 Roughness zones and corresponding IDs in updated model. 65
Figure 25 Hypothetical diagram on lake outlet hydraulics. 70
Figure 26 Critical average velocities for gravel mobility. From S. E. Coleman & Smart (2011). 71
Figure 27 HSI curve showing the spawning suitability of Chinook and sockeye salmon to current velocity. From Ptolemy (2001) and West et al. (2023). 74
Figure 28 HSI curve showing the spawning suitability of Chinook and sockeye salmon to water depth. From Ptolemy (2001) and West et al. (2023). 74
Figure 29 Hjulström (1935) curve. Adapted from Nichols (2010). 75
Figure 30 Aerial views of the delta formations located at the boundary between Muchalat Lake and Muchalat River from (a) Google Earth showing likely sediment pathways and (b) from the RPAS orthoimagery showing the small ephemeral streams creating the deltas. 76
Figure 31 (a) Ground view of the east delta (canoe paddle for scale) showing the footprint of the active channel and remnant water pooled on the left side of the image. (b) The material is small-medium gravels. 77
Figure 32 Deposited sand bar in the footprint of the west ephemeral stream. Remnant water is pooled in the deeper sections, but the water is stagnant. 77
Figure 33 View of the (a) fine substrate and (b) vegetation between the two deltas 78
Figure 34 Aerial view of the vegetative bed rise 79
Figure 35 Bed view on river left showing randomly deposited branches and fines. 79
Figure 36 Bed view of the center-left of the river showing larger areas of deposited fines. 79
Figure 37 Bed view of the center-right of the river, showing a mix of logs and branches, with deposits of gravel visible under a layer of algae and/or fines 80
Figure 38 View of the right side of the channel showing logs and larger branches. More algae are visible here, with substantial weedy material growing on the boulder at the channel edge. Some gravel and cobbles are visible under layers of algae and/or fines. 80
Figure 39 Location of the six ADCP transects collected during EFT3 superposed over simulated velocities from the simulation using the calculated discharge on this field day (123 m^3/s). 81
Figure 40 Sample plots comparing measured and modeled velocities vectors and magnitudes at (a, b) transect 001 and (c, d) transect 005 for the HiFT calibration scenario 82

Figure 41 Gravel mobility predictions for the 20-year return flow by the initial model using the (a) classical friction method and (b) Saint-Venant momentum equation method. 84
Figure 42 Gravel mobility predictions using the updated model for the (a) 2-year, (b) 20-year and (c) 100-year return flows. 85
Figure 43 Recovered tracer stone locations shown as coloured points. Red crosses denote BM locations, while the transect lines are shown as white lines. 87
Figure 44 Percentage of recovered stones by cross-section and size. Medium (M) and large (L) stones were generally more readily found than small (S) stones. 88
Figure 45 Recovery rate by lateral seeded location in the channel. 88
Figure 46 Mobility pattern based on seeding location, with the numbers in each cell representing the last three digits of the tracer's unique tag number. 89
Figure 47 Comparison of the modeled gravel mobility predictions under the peak 2023 flow (146 m^3/s) with recovered tracer stone locations, categorized by size and travel distance, $\boldsymbol{L}$ (m). 90
Figure 48 Tracer displacement lengths relative to predicted mobility ratios based on an assumed reference Shields parameter of 0.045. Tracer motion or stability correctly predicted by the model are shown in blue, while those that were incorrectly predicted are shown in red. Expected error of the Shields parameter threshold is shown by the shaded area. 93
Figure 49 Chinook HSI for (a) depth and (b) velocity under peak Chinook spawning flow (Oct average), and (c) depth and (d) velocity under peak Coho spawning flow (Nov average). 95
Figure 50 Sockeye HSI for (a) depth and (b) velocity under peak spawning flow (Oct average). 96
Figure 51 Areas at risk of fines deposition under 7Q10 flow and areas where fines are likely to flush under 400% MAD. 96
Figure 52 Areas fulfilling all design criteria based on gravel mobility under the (a) 2-year, (b) 20-year and (c) 100-year return flows. 97
Figure 53 Areas fulfilling the design criteria based on gravel mobility under the 100-year return flow when (a) considering fines deposition and flushing potential, (b) disregarding fines deposition and (c) excluding all consideration of fines. 99
Figure 54 Predicted mobility patterns for the (a, b) 2-year and the (c, d) 100-year return flows using the median and maximum grain sizes in each size class. 106
Figure 55 Distribution of mobile and immobile tracers with mobility ratios. 109

Figure 56 Fraction of tracers that were immobile above the predicted mobility threshold based on assumed reference Shields parameters of (a) 0.045 and (b) 0.030. 110
Figure 57 Achieving balance for gravel augmentation at a lake outlet. 115

List of Tables

Table 1 Summary of completed field trips and collected data 36
Table 2 Field trip discharges used for numerical model calibration 40
Table 3 Design discharges for model simulation 42
Table 4 Summary of completed RPAS flights 47
Table 5 Projection error summary statistics 48
Table 6 Tracer stone size class characteristics, obtained from the spawning substrate GSD 54
Table 7 Tracer placement pattern across the transects 56
Table 8 Boundary conditions for the initial and updated models 61
Table 9 Nikuradse roughness values in each channel friction zone 63
Table 10 Baptist (2007) vegetation model parameters for each class 64
Table 11 Gravel gradation for four target species. From West et al. (2023). 66
Table 12 Assumed pit run gradation 67
Table 13 Gravel placement gradation 67
Table 14 Shear velocity thresholds for sockeye and Chinook gravel mixes 69
Table 15 Critical velocities for entrainment of key size classes, from Figure 26 72
Table 16 Performance statistics for velocity during the HiFT calibration scenario (123 m^3/s) 81
Table 17 Performance statistics summary for MeFT flow scenario (10.2 m^3/s) 83
Table 18 Comparison of percentage of predicted and actual mobility 94
Table 19 Example of the difference in scales for calculated shear stress for different size classes 105

List of Abbreviations

Abbreviation	Description
1D	One-dimensional
2D	Two-dimensional
3D	Three-dimensional
AC	Alternating current
ADCP	Acoustic Doppler current profiler
ADV	Acoustic Doppler velocimeter
AWG	American wire gauge
BC	British Columbia
BCSRIF	British Columbia Salmon Restoration and Innovation Fund
BM	Benchmark
CGG2013	Canadian Gravimetric Geoid of 2013
CGS	Canadian Geodetic Survey
CGVD2013	Canadian Geodetic Vertical Datum of 2013
CGVD28	Canadian Geodetic Vertical Datum of 1928
CHC	Canadian Hydraulics Centre
COSEWIC	Committee on Species of Endangered Wildlife in Canada
CP	Control point
CSF	Cloth simulation filter
CSRS	Canadian Spatial Reference System
DEM	Digital elevation model
DFO	Department of Fisheries and Oceans Canada
EFT	Ecofish field trip
FT	Field trip
GCP	Ground control point
GIS	Geographic information system
GPS	Global positioning system
GSD	Grain size distribution
HDX	Half duplex
HEC-RAS	Hydrologic Engineering Center River Analysis System
HRV	Historical range of variability

HSI	Habitat suitability index
ID	Identification
LAI	Leaf area index
LB	Left bank
LiDAR	Light detection and ranging
MAD	Mean annual discharge
MAV	Mean absolute value
MMFN	Mowachaht/Muchalaht First Nation
NAD83	North American Datum of 1983
NCD	Natural channel design
NRC	National Research Council
NSE	Nash Sutcliffe efficiency
NSWS	Nootka Sound Watershed Society
PHABSIM	Physical habitat simulation
PIT	Passive integrated transponder
PPP	Precise point positioning
PVC	Polyvinyl chloride
RB	Right bank
RFID	Radio frequency identification
RHRG	River Hydraulics Research Group
RMS	Root mean square
RMSE	Root mean square error
RPAS	Remotely piloted aircraft system
RS	Reynolds stress
RTK	Real-time kinetic
SDS	Slotted drive system
SVE	Saint Venant equation
TCP	Temporary control points
TSS	Total suspended solids
UAV	Unmanned aerial vehicle
UBC	University of British Columbia
UHF	Ultra-high frequency
US	United States

USGS	United States Geological Survey
UTM	Universal Transverse Mercator
UW	University of Waterloo
WCVI	West Coast Vancouver Island
WFP	Western Forest Products
WSC	Water Survey of Canada
WSE	Water surface elevation
WUP	Water use planning
XS	Cross-section

List of Symbols

Symbol	Description
Br	Integration constant in the Prandtl-von Karman log-law distribution (-)
b	Channel width (m)
b_{RS}	Slope of the Reynolds stress momentum profile (-)
C	Chézy roughness coefficient ($m^{1/2}/s$)
C_d	Drag coefficient (-)
C_f	Dimensionless skin friction coefficient (-)
C_n	Courant number (-)
c	Wave celerity (m/s)
D_{50}	Median grain size diameter (m)
D_{84}	84^{th} percentile grain size diameter (m)
D_g	Geometric mean grain size diameter
D_i	B-axis diameter of the i^{th} percentile particle size
D_v	Average vegetation cylinder diameter (m)
d_A, d_B, d_C	Grain diameters of the A-, B- and C-axis, respectively (m)
Fr	Froude number (-)
f_i	Relative fraction in size class i (-)
g	Gravitational acceleration (m/s^2)
H	Time-averaged flow depth (m)
h	Time-variant flow depth (m)
h'	Deviation from the time-averaged flow depth (m)
h_1	Water depth above the channel crest (m)
h_2	Water depth below the channel crest (m)
h_p	Average vegetation height (m)
k	Viscous drag coefficient
k_N	Nikuradse equivalent sand-grain roughness (m)
k_s	Roughness height (m)
L	Particle displacement length (m)
m	Vegetation density ($1/m^2$)
p^*	Piezometric pressure head (m)
Q	Discharge (m^3/s)

R_h	Hydraulic radius (m)
r_A, r_B, r_C	Grain radii of the A-, B- and C-axis, respectively (m)
S_g	Sediment specific gravity (-)
S_o	Bed slope (-)
S_w	Water surface slope (-)
s	Position in the streamwise direction (m)
T	Mobility ratio (-)
U_c	Maximum velocity in the flow column (m/s)
u	Flow velocity in the x- or streamwise direction (m/s)
u_*	Shear velocity (m/s)
$\bar{u}$	Time-averaged velocity in the streamwise direction (m/s)
$\bar{u}_h$	Time-averaged velocity in the streamwise direction at the free surface (m/s)
u'	Mean turbulent fluctuations in the streamwise direction (m/s)
V	Scalar depth-averaged velocity (m/s)
$\forall$	Particle volume (m^3/s)
v	Flow velocity in the y- or lateral direction (m/s)
w	Flow velocity in the vertical direction (m/s)
$\bar{w}$	Time-averaged velocity in the vertical direction (m/s)
w_h	Time-averaged velocity in the vertical direction at the free surface (m/s)
w'	Mean turbulent fluctuations in the vertical direction (m/s)
X_j, Y_j	Floating coordinates of the j^{th} measured point (m)
X_j', Y_j'	Real-world coordinates of the j^{th} measured point (m)
X_0', Y_0'	Real-world coordinates of the control point (m)
z_o	Reference height (m)
α	Dip parameter (-)
β	Streamwise pressure gradient parameter (-)
Δ	Specific gravity of sediment (-)
δ	Depth of U_c relative to h_0 (m)
γ	Specific weight of water (N/m^3)
θ	Angle of repose (º)
κ	Von Kármán coefficient (-)
ν	Fluid kinematic viscosity (m^2/s)
ξ	Aspect ratio threshold governing wake effects (-)

Π	Coles wake parameter (-)
ρ	Fluid density (kg/m^3)
ρ_s	Particle density (kg/m^3)
τ_o	Wall shear stress (N/m^2)
τ_{rm}	Reference shear stress of the median particle size (N/m^2)
τ_{rm}^*	Reference shear stress of the median particle size (-)
τ_{ri}	Reference shear stress of the i^{th} particle size class (N/m^2)
τ_{ri}^*	Reference shear stress of the i^{th} particle size (-)

Preface

The title of this thesis “Achieving contrapuntal balance at a lake outlet: Restoring salmon spawning habitat with gravel augmentation design” has two distinct meanings. The first is an acknowledgement to my roots as a classically trained pianist and an homage to my nemesis and kryptonite: Johann Sebastian Bach and his prized fugues, which are considered the most complex and artfully designed examples of counterpoint. Counterpoint refers to a type of music originating in the Renaissance period that consists of multiple voices carrying complementary yet contrasting melodic lines.

Parallels abound between writing fugues and engineering, one of which is the need to balance multiple priorities to achieve a successful design. Both composition and engineering have design objectives at a range of scales that must be fulfilled by varying a set of parameters. For counterpoint, these objectives are the melodies interweaving through the voices that must be heard even amongst the complex layers of sound occurring simultaneously. To achieve this effect, the composer must be constantly aware of which voice carries the main melody at each measure and how to fit the other harmonically complementary yet melodically contrasting voices around it. Design decisions must regularly made, and exceptions to minor rules occasionally accepted to avoid infracting on the more significant laws of counterpoint or to create moments of musical interest. A balance must be struck between the voices and melodies, between the occasional bending of guidelines and adherence to rules, and between the appropriate amount of risk to take to achieve a more successful outcome.

The second meaning behind the title is perhaps a less obscure one to grasp. As my supervisor aptly noted, counterpoint also bears a coincidental resemblance to the French word *“contre-pente”*, which in hydraulics, is defined as the slope opposing the natural flow of water. In more technical words, *contere-pente* is an adverse bed slope, and is therefore a term that is fitting for this study on a lake outlet where the hydraulics are unique precisely because of the adverse bed slope. The rationale behind designing gravel augmentation at lake outlets is the understanding that accelerating flow over an adverse slope should produce an optimal location along the channel where multiple criteria can be balanced. The sediment should be stable enough to resist scour but close enough to the threshold of motion that the material can be excavated by salmonid spawners; velocity should be high enough to induce hyporheic flow and resist fines deposition but not so high as to make the site unsuitable for spawning; and depth too should meet the range for spawning habitat suitability. Contrapuntal balance can therefore also describe this need to balance these design elements over an adverse bed slope.

Chapter 1
Introduction

Climate change and anthropogenic activity have altered hydrologic regimes in many watersheds globally, causing an increased frequency in extreme flood events. These flashier floods have resulted in greater scour in riverbeds, leading to extensive habitat loss for riverine fish species and a consequent decline in aquatic populations. In British Columbia, forestry activities in mountainous watersheds and unpredictable weather patterns caused by climate change have been a driver for the degradation of streams. Concurrently, overfishing has strained the native salmon population. Concerns about the implications of industrial logging and fisheries on the conservation of native species have led to the recognition of the importance of indigenous consultation and an accompanying upsurge in indigenous-led restoration initiatives. Presently, many indigenous-led restoration projects call for process-based restoration techniques that allow for the stream to resume its ecological function through guided engineering interventions rather than imposed structural designs that would otherwise disrupt the river's functions. One such process-based restoration technique is gravel augmentation, or the strategic placement of gravel in a sediment-starved river to create an artificial sediment supply for the river. This technique allows the flow to rework the sediment to a natural equilibrium and restore of spawning grounds for fish.

1.1 Background

Climate and land-use influences on hydrology have been well-documented to have adverse impact on the quality of aquatic habitat in mountainous gravel bed streams (Scheurer et al., 2009). The effects of forest from logging is significant on Vancouver Island, with nearly 75% of the original forest habitat lost between 1995-2003 (Costello, 2008). Combined with the increased frequency of extreme weather from climate change, the resultant high stream flows have eroded streambeds and caused historically gravel-filled beds to scour down to cobble- and boulder-beds. Increased scour, along with other logging impacts such as increased stream temperatures, sedimentation, and wood inputs, have altered the ecosystems on many watersheds on the island. These changes have deteriorated the quality and abundance of habitat for many freshwater fish, including the Nootka and Kyuquot stocks of the West Coast Vancouver Island (WCVI) Chinook salmon (COSEWIC, 2021; Pike et al., 2010; Winkler et al., 2010). Recent conservation efforts on the island have consequently focused on the preservation of

Chinook salmon, and other native salmonid species. The urgent need for intervening action is underlined by historic observations of population decline by local First Nations and the recent "Threatened" designation assessed by the Committee on Species of Endangered Wildlife in Canada (COSEWIC) in November 2020 (COSEWIC, 2021).

The Nootka Sound Watershed Society (NSWS) and Mowachaht/Muchalaht First Nation (MMFN) have been developing a program of initiatives since the 1990s to improve Chinook habitat in the Gold River subwatershed, including a Nootka Sound Salmon Parks network designation and a salmonid conservation study through the BC Salmon Restoration and Innovation Fund (BCSRIF). The latter initiative was completed by the industry partner for the current research (Ecofish Research Ltd.), wherein the Muchalat Lake outlet was identified as a high priority site for spawning habitat restoration using gravel augmentation. The site selection and project justification arose from six key elements: (1) the existing presence of the species within Muchalat River, (2) the potential to support a plan by Fisheries and Oceans Canada (DFO) to release Chinook smolts in Muchalat Lake, (3) the importance of salmonid and ecosystem health to MMFN cultural heritage, (4) feedback from MMFN who favoured the use of spawning gravel placement over a Natural Channel Design (NCD) approach, (5) the potential benefits for secondary salmonid species who are also under threat, and (6) alignment with other initiatives for salmonid recovery in the region. The gravel augmentation project will be completed in conjunction with other initiatives such as sediment control and riparian forest restoration, pending funding approval (West et al., 2023).

Gravel augmentation has been shown to increase spawning utilization by Chinook salmon in other sites in North America (Zeug et al., 2014). Lake outlets are considered attractive sites for gravel augmentation projects due to the preference of the target salmon species and their perceived stability for the placed substrate (Gottesfeld et al., 2004, 2008; Hauer et al., 2015; Sweeney-Bergen et al., 2021). Restoration designs in these environments are often designed based on the intuition and experience of local stream restoration practitioners, with little research conducted on the validity of these assumptions. Lake outlets undergo accelerating flow over adverse bed slopes (i.e., the bed slope angled in the opposite direction of flow), which is a distinctly different morphology and flow condition than those on which most design guidelines and equations are based. Hydraulic analysis of river systems is typically conducted using empirical equations that were derived for uniform flow conditions (e.g., Shields equation, Manning's equation, etc.), although they are widely applied to non-uniform flow channels. Consequently, the identification of an optimal placement location using

computational models that employ these equations is subject to considerable uncertainty. Likewise, the sensitivity of the identified optimal location along the streamwise gradient of depth, shear stress and habitat suitability under accelerating flow can vary depending on differences in model assumptions. A systematic and methodological framework for evaluating gravel placement designs is therefore desirable. The need for evidence-driven design and research-based methodologies is an important research gap for improving the success rate of future sediment augmentation projects.

1.2 Objectives

The goal of this study was to advance the engineering methodology for evaluating the design criteria of a gravel augmentation project for salmon spawning habitat restoration at a lake outlet. These design criteria include the evaluation of gravel stability under flows of various design return periods, sand transport potential under a flushing discharge, the risk of sand deposition under a low flow and habitat suitability under seasonal spawning flow rates. The project primarily targeted Chinook salmon, but other native anadromous salmonids are expected to benefit from the project, as the placed gravel will eventually migrate downstream to their spawning areas. Sockeye salmon were considered a secondary target species, and high-level analysis was completed on the habitat suitability for this fish. The remaining salmon species (steelhead, Coho, pink, and chum) are lower priority species for this project; thus, no analysis was completed to evaluate the suitability of the created habitat for these fish. The research goal was accomplished through three objectives: (1) assess the viability of using two-dimensional models to model lake outlet hydraulics, (2) validate the strategy using sediment tracers in the pre-construction condition, and (3) specify a gravel spawning pad placement strategy for Chinook and sockeye salmon in the Muchalat Lake outlet.

1.3 Research project context

This study was partnered through a Mitacs Accelerate fellowship with Ecofish Research Ltd (“Ecofish”), who provided invaluable technical expertise on local conditions and stream restoration practices in BC. Support on the historical knowledge of the local environment was also indirectly provided by NSWS and MMFN, who were the clients retaining Ecofish on this project.

The tracer stone methods employed in this study are founded on a collective of work and expertise by past and current members of University of Waterloo River Hydraulics Research Group (UW RHRG). This project continues the work of a larger research program in the UW RHRG that aim to

understand the sediment dynamics of pool-like structures in natural rivers and apply this knowledge to further gravel augmentation as a process-based sediment-conscious stream restoration approach. Incorporating sediment transport in river management decisions allows engineers to account for sediment responses to restoration strategies and develop more ecologically successful designs.

1.4 Thesis organization

This thesis is organized in six chapters. Relevant literature is reviewed in Chapter 2, including approaches in river restoration, salmon spawning behaviour and habitat, hydraulics and sediment transport in accelerating flow, factors impacting critical shear stress and the application of numerical models to salmon habitat restoration. The study site and methodology are described in Chapter 3 and the results are reported in Chapter 4. Discussion of the results, limitations and recommendations for future work are presented in Chapter 5. The conclusions of this thesis are summarized in Chapter 6.

Chapter 2
Literature Review

2.1 River restoration

2.1.1 Approaches to river restoration

Human activity in and around rivers have altered landscape dynamics, leading to profound implications on the ecological functions and processes of many rivers globally (Bernhardt & Palmer, 2011; Poff et al., 1997; Wohl, 2005). These human perturbations lead to consequences such as alterations to flow regimes, to sediment fluxes and to the chemical composition in the water. When combined, these effects can promote the invasion of non-native aquatic species. Non-native species tend to have better biological or environmental resistance than their native counterparts who may be too acclimated to the specific natural flow patterns in the channel (Olden et al., 2006; Wohl, 2005). Native fish populations suffer from these impacts, resulting in a threat to the local biodiversity.

Accordingly, there has been an effort over the last half century to improve the ecological and geomorphic resilience of rivers through some form of "naturalization" or "restoration" of various aspects of degraded streams, with the assumption that the mimicry of nature is the ideal solution for all fluvial problems. (Wohl et al., 2015). River restoration refers to some type of mitigation, rehabilitation, or manipulation of channels affected by human activity with the objective of transforming some form or function of the river closer to its natural state (B. MacVicar et al., 2015; Wohl et al., 2015). This state is often defined by the practitioner based on biodiversity, ecological function, geomorphological function, stability, or aesthetics, and depends on the interests and goals of the practitioner (Bernhardt & Palmer, 2011; García et al., 2021a; Palmer et al., 2005; Wohl et al., 2015). The term restoration is therefore a misnomer, as restoration implies a reversal of the status quo to a past (and presumably better) state that is often arbitrarily defined (Miller & Kochel, 2010; Wilcock, 2012; Wohl et al., 2015). True restoration, short of an immediate and drastic removal of all human presence, structure, or intervention from the river, is often both impractical and impossible.

While some restoration projects have addressed river function, many reach-scale projects have historically focused on the appearance and aesthetics of the stream. The restoration of form is often preferred over function due to public perception and social priority, with most projects focusing on reaches considered to be unsightly or hazardous (Wohl, 2005). Form-based restoration was

popularized by the hydrologist and geomorphologist Dave Rosgen, the infamous creator of the Rosgen Classification System for stream forms (Rosgen, 1994; Wilcock, 2012; Wohl et al., 2015). Rosgen developed the NCD methodology which professes to be a nature-based solution for solving river issues without imposing a solution on nature. This methodology consists of designing reaches to match the pattern, profile and dimensions of a reference reach that is selected by the practitioner based on historical records of the site where available or a representative stream with similar pre-development conditions (Rosgen, 1994; Wohl et al., 2015). The attempt at stream stability is then made through the installation of in-stream structures where the goal is often to minimize lateral migration until riparian vegetation is well-established, mitigate damage to infrastructure and property, and provide some semblance of aquatic habitat (Miller & Kochel, 2010; Rosgen, 1994). NCD has since become the template for many restoration projects in the United States (US) (Wilcock, 2012), however Rosgen (1994, 2021) noted that NCD can cause more damage than benefit when it is misused by practitioners who do not have a firm understanding of geomorphology or channel adjustment processes.

Despite Rosgen's advocacy for NCD as a nature-based solution, it is fundamentally an imposed human-sourced template on nature. NCD is often criticized for its oversimplification of river processes, as practitioners tend to ignore the extensive diversity of stream types and the appropriateness of the channel form in the wider geomorphic context of the site. Many NCD projects have consequently taken the form of constructed single-thread meandering pool-riffle channels, at times despite a natural inclination towards other channel morphologies due to site-specific sediment loads, valley slopes or hydrological regimes (Beechie et al., 2010; Wohl et al., 2015). Furthermore, the foundational assumptions of this method fail to acknowledge that equilibrium for rivers is inherently dynamic, and habitually result in unnaturally static beds that do not serve the river's ecological needs (Beechie et al., 2010; Bernhardt & Palmer, 2011; García et al., 2021; Miller & Kochel, 2010; Wilcock, 2012). Many reconfigured channels 'fail' as they undergo extensive adjustments post-construction, thus negating the initial intention of increasing stability (Miller & Kochel, 2010).The rarity of adequate monitoring and the limited understanding of river processes has led to the failure of many of these reach-scale restoration efforts in addressing the physical, hydrological, biological, or chemical functions of the river, and eventually result in a loss of riverine taxa and a decline in water quality (Wohl et al., 2015).

More recently, efforts in developing process-based restoration techniques that restore river functions have emerged in research as a response to the failures of form-based restoration (Arnaud et al., 2017; Papangelakis & MacVicar, 2020; Wilcock, 2012). Process-based restoration aims to restore the physical, chemical, and biological processes that are critical in creating and sustaining river ecosystems. Attaining these outcomes is completed by addressing root causes or systemic drivers of stream degradation rather than through superficial solutions (Beechie et al., 2010). Compared to form-based approaches that tend to be constrained to reach-scale projects, process-based restorations have the capacity to be applied to larger spatial contexts (Wohl et al., 2015).

Poff et al. (1997) recommended adopting a holistic view in restoring the natural variability of the system; they suggested that process-based restoration could be accomplished by enacting policy changes that address watershed and streamflow management in conjunction with applying scientific models to fuel the design. Other examples of process-based restorations include enacting regulations stipulating the minimum allowable flows (Poff et al., 1997); the removal of dams to restore sediment fluxes (Bernhardt & Palmer, 2011); promoting channel-floodplain (i.e., lateral) connectivity, longitudinal connectivity and ecological integrity by removing riprap, levees and other structures (García et al., 2021a; Wohl et al., 2015); designating a free erosion corridor to allow the river to reclaim part of its floodplain (García et al., 2021a, 2021b); reducing riparian grazing; reintroducing beavers to historically occupied habitats; manipulating flow releases from dams to mimic natural flows or rebuild sedimentary cover (Wohl et al., 2015); and sediment augmentation (Staentzel et al., 2020). The selection of the most effective approach is highly context- and site-specific; often the optimal approach to maximizing the outcomes of a successful restoration requires a multi-pronged package of solutions at a variety of scales that may include both form- and process-based strategies (Beechie et al., 2010).

2.1.2 Success metrics in process-based restoration

Compared to the simplistic success metrics used for form-based restoration, quantifying success in the context of process-based or multi-pronged approaches is difficult, as the question on what constitute restoration for a process is more contentious than the standards for restoring an appearance. Defining realistic goals and objectives is critical for achieving a successful restoration, but this process can be complex (Saldi-Caromile et al., 2004), since identifying the desired outcomes should be done so in recognition of how anthropogenic constraints—such as immoveable structures like

dams or industrial activities in the watershed like logging or fisheries—and technical gaps—such as limited accuracy of models, the unpredictability of ecological responses, the presence of non-native species, and the complexity of process interactions—can limit restoration potential (Beechie et al., 2010; Saldi-Caromile et al., 2004). Once a presumably strong understanding of risk and the required contingencies is obtained and reasonable goals are defined, the practitioner should then ask, "How should we measure the success of the project in achieving these goals?"

For process-based approaches, the use of a single reference condition as a success metric is inappropriate, as the rate of a process can vary between streams that otherwise appear similar and 'equivalent'. In cases where an adequate historical record can be obtained, Wohl et al. (2015) proposed an evaluation of channel characteristics based on a historical range of variability (HRV) rather than a template reference condition. Papangelakis & MacVicar (2020) advocated for a sediment transport approach using individual coarse grains tracers within a gravel bed river and suggested that restoration could be considered successful if the bed sediment distribution is being transported downstream at a rate equal to its pre-disturbance value. This method is most appropriate for restoration approaches that employ analytical relationships between discharge and sediment transport to remediate river functions, such as sediment augmentation (Miller & Kochel, 2010; Papangelakis & MacVicar, 2020; Wohl et al., 2015). Other common metrics are based on biological variables, such as a species' prevalence in the study area or its growth rate. However, Poff et al. (1997) noted that designing a restoration effort based on the ideal conditions for individual species may not be beneficial for the remainder of the ecosystem, nor is designing for the ecosystem necessarily optimal for the individual species residing within it.

It is evident that single criterion approaches are limited in their ability to define ecological success, due to the vague and contentious definition of 'ecology'. Palmer et al. (2005) defined 'ecological' as a term encompassing all natural aspects of a river (biological, hydrological, and geomorphic) and affirmed that the achievement of ecological goals must occur in conjunction with social and research successes for a restoration project to be considered unanimously successful. The authors noted that the success of a restoration effort in attaining its defined endpoint is often contingent on public and stakeholder support, which is largely informed by factors such as the protection of infrastructure, recreation, and aesthetics, which often contradict ecological goals. Consequently, restoration projects considered successful by stakeholders—even those not considered ecologically successful—are more likely to receive public recognition and yield funding for similar projects in the future (Wohl et al.,

2015). However, Palmer et al. (2005) also commented that the lessons learned from each project are valuable regardless of whether ecological or social goals are met, as they have the capacity to fuel successes in the future. García et al. (2021) agreed with this principle and suggested that any engineered effort to restore a stream should be accompanied by passive measures such as educating the public on the values and risk of floods, improving technical training to practitioners, and applying watershed-scale land use management policies. Regardless of approach, a balance must be struck between the environmental benefits of allowing the river dynamics to reach its own equilibrium and the economic benefits of mitigating erosion to protect infrastructure; a second balance must then be struck between the social priorities and ecological urgency of undertaking such projects (García et al., 2021). Restoration efforts should thus be coupled with community education initiatives and professional training to effectively address the need to redirect restoration approaches to more sustainable techniques (García et al., 2021; Miller & Kochel, 2010; Papangelakis & MacVicar, 2020).

2.1.3 Gravel augmentation as a process-based restoration technique

Sediment augmentation is a hydromorphological restoration technique that involves the creation of an artificial sediment supply in starved rivers through the strategic placement of sediment (typically gravel) in the channel. The objective of the technique is to improve resilience to floods, recover biodiversity through habitat rehabilitation, and restore sediment dynamics (Staentzel et al., 2020).

First applied to restore fish habitat in the sediment-starved reaches below dams, sediment augmentation is now commonly used in the US, Japan, and Europe for a variety of applications including urban stream degradation, river regulation, and bank armoring (Arnaud et al., 2017; Mörtl & De Cesare, 2021; Saldi-Caromile et al., 2004). In North America, the technique is primarily used to restore freshwater salmonid habitat in gravel bed rivers that may have been scoured due to anthropogenic activities in the watershed or climate change (Mörtl & De Cesare, 2021). Many indigenous-led projects in British Columbia (BC) employ sediment augmentation with spawning gravel–sized substrate to restore declining salmon populations, as the approach is thought to be less intrusive than channel reconstruction. While some design guidelines for gravel augmentation strategies do exist (Saldi-Caromile et al., 2004), the practice is still relatively empirical and relies heavily on the judgement and experience of local practitioners. The lack of a systemic framework for restoration design, monitoring, and assessment contributes to the high levels of uncertainty and risk associated with attempting these projects. The development of reliable protocols and metrics to

implementing gravel augmentation is still in its exploratory phase, with significant research opportunity available to contribute to the currently sparse body of literature (Arnaud et al., 2017).

The classification of gravel augmentation as a form- or process-based method within literature is contentious—although the method is often viewed as a process-based method due to its outcome of restoring downstream sediment fluxes and allowing morphological processes to form habitat (Arnaud et al., 2017), Beechie et al. (2010) and Saldi-Caromile et al. (2004) argued that gravel augmentation constitutes a form-based habitat restoration strategy as it fails to address root causes of degradation. Most gravel placement only provides temporary ecosystem recovery, as the gravel will eventually transport out of the reach unless periodically replenished by a natural or engineered sediment supply. The lifespan and lifecycle cost-effectiveness of these designs are limiting factors in their success, thus they should only be implemented following a watershed-level analysis of the project's value and in conjunction with other higher-level restoration efforts (Saldi-Caromile et al., 2004).

Other researchers (e.g., MacVicar et al., 2015; Papangelakis & MacVicar, 2020; Wilcock, 2012) have argued that the classification of the strategy as process-based restoration stems from the need for a comprehensive understanding of the sediment transport regime in order to achieve success. The perception of gravel augmentation as a structural technique comes from the practice of sizing and placing gravel mixtures that are designed to remain immobile. Such operations ignore the geomorphological functions of sediment supply and ultimately fail to restore fluvial processes. Gravel augmentation designs that are intended to result in the reconstruction of natural morphologies require knowledge of processes and can therefore be classified as a process-based restoration. Augmentation in this context is fraught with uncertainty and gives rise to knowledge gaps on how hydraulic and sediment transport concepts apply in a range of environments, such as lake outlets. The accumulation of knowledge on the sediment regime in various geographical contexts through numerical modelling and sediment tracking is therefore crucial to improving the project success rates. Sediment motion and dispersion should ideally be studied in relation to unsteady flow since hysterical patterns can affect the type and extent of movement, and therefore the degree of freedom when designing gravel augmentation projects (Humphries et al., 2012).

2.1.4 Design considerations for gravel augmentation

The structural approach of designing gravel placements stems from caution on what constitutes a "safe" design. Overdesigning for stability can originate from funding limitations but also from the

historical failures of gravel augmentation projects that were implemented by well-meaning practitioners designing without adequate technical support.

Enhancing sediment without consideration of the site's context within a watershed, stream condition or the relationships between stream variables can have unintended adverse outcomes that actively deteriorate the resource originally intended for restoration (Beechie et al., 2010; Saldi-Caromile et al., 2004). Such outcomes may arise from attracting fish to spawn in a freshly placed gravel pad, only for the substrate and the buried eggs to be washed out in the first flood event due to an incomplete understanding of the discharge-sediment transport relationship. These mistakes are costly not only to the project funders and stakeholders but also to the fish populations who effectively lose a cohort of future spawners. Channel instability—channel avulsion, meander migration, or bed and bank erosion or deposition—may also result from the essentially instantaneous aggradation of sediment in the channel (Saldi-Caromile et al., 2004). Depending on the scale of the gravel pads relative to the stream network, these effects can initiate a morphological or biological response through a considerable length of the stream outside of the target reach.

For gravel placements that are intended to restore fish habitat, successful designs require some sediment transport at high flows to clear out interstitial fines and aquatic vegetation that may be clogging the gravel, but they must remain stable enough to withstand scour. The evaluation of these designs must therefore evaluate both the sediment transport dynamics and habitat suitability for the target species (Brown & Pasternack, 2009), which requires some knowledge on spawning behaviour and habitat preferences of the target and other local native species.

2.2 Salmon spawning habitat

The quality of a spawning site is dependent on three primary physical variables—the availability of suitable spawning-sized substrate, channel hydraulics and hyporheic flow conditions. The preference of fish species for each of these variables were previously treated in isolation with each other (and with other non-physical controls) but have since been demonstrated to be interconnected and highly dependent on local channel conditions (Kondolf & Wolman, 1993; Moir & Pasternack, 2010). These variables are tied together by flow, which functions as a key driver and determinant for riverine habitat due to its effect on both physical habitat and evolutionary life histories of aquatic species (Bunn & Arthington, 2002).

2.2.1 Salmon spawning mechanism

The range of suitable conditions can be better defined through the understanding of salmon spawning behaviour and the effects of such behaviour on the surrounding environment. Salmon spawn by laying their eggs in redds or excavated piles of gravel. The female fish digs redds in a gravel streambed using a rapid tail flapping motion. The flexing of the tail creates water jets that mobilize sediment and direct the grains to an accumulated pile, termed the 'tailspill'. Once a suitably deep depressions has been excavated in the bed, the female lay their eggs in the pit while the male simultaneously swims adjacent and fertilizes the released eggs. The female then buries the fertilized eggs with gravel by repeating the tail flapping process to cover the eggs and create a dune-shaped bedform, or a redd. The shape of the redd is characterized by a tailspill and an upstream depression, or a 'pot', as shown in Figure 1 (Buxton, Buffington, Yager, et al., 2015; DeVries, 1997; Gottesfeld et al., 2008).

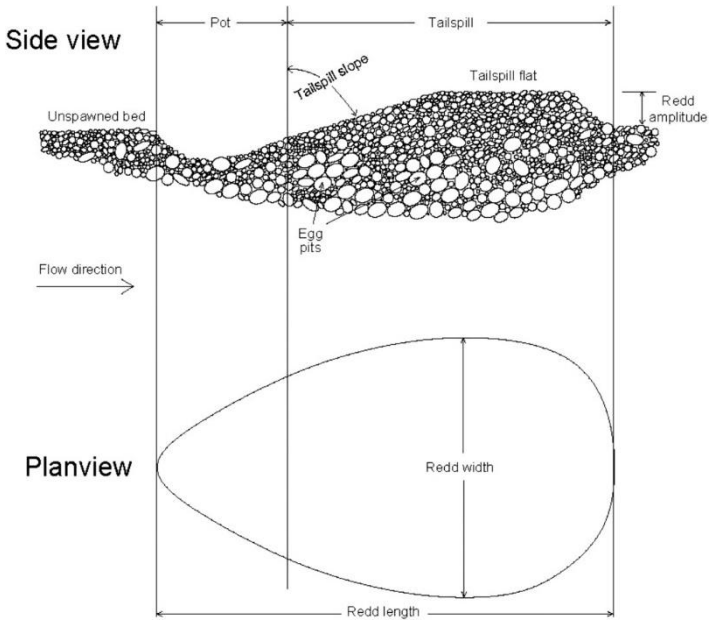


Figure 1 Schematic representation of a salmon redd. From Buxton et al. (2015).

2.2.2 Salmon spawning habitat quality

The preferred sizes of spawning substrate and the size of the constructed redd depend on the size and species of the spawning fish. These parameters affect egg survival rate; larger fish are able to bury their eggs deeper and under coarser sediment, thereby providing better protection from predators and

mobilization (Cienciala & Hassan, 2013; Kondolf & Wolman, 1993). Despite size selective spawning tendencies however, the range of sizes used by a species is often broad, thus allowing for multiple species to be targeted with a single restoration initiative.

The mobilization of sediment through the digging action disturbs the bed material and allows sand, silt, and clay to be flushed downstream. The coarser gravel grains remain and provide a relatively clean cover for the eggs that allows hyporheic flow to pass through the buried eggs in the redd, which delivers oxygenated water and exports metabolic waste (Buxton, Buffington, Tonina, et al., 2015; Buxton, Buffington, Yager, et al., 2015; Tonina & Buffington, 2009). The importance of hyporheic flow for egg survival reflects in the ecological preferences of Chinook salmon, as they tend to select patches of gravel with maximum upwelling or downwelling flows for redd construction (Geist et al., 2002; Geist & Dauble, 1998; Gottesfeld et al., 2008).

The infiltration of fine sediment in the interstices of the gravel limits hyporheic flows, therefore presenting a risk for embryo survival by reducing dissolved oxygen concentrations (Lisle, 1989; Sear et al., 2008; Slaney & Zaldokas, 1997). Hydraulically sheltered spawning sites can be more susceptible to fine sediment accumulation due to low velocities even if the reach is sediment-starved (Cienciala & Hassan, 2013). The regular flushing of fine grains is therefore essential to the maintenance of high-quality spawning substrate. However, the capacity for flushing in a gravel patch depends on its proximity to the thalweg and the significance of recirculatory zones in the channel (Rathburn & Wohl, 2003), so evaluation of flushing often requires detailed numerical models.

In addition to physical clogging, reductions in surficial permeability may also result from bioclogging through the growth of biofilm, or a matrix of microorganisms on the bed surface (Shrivastava et al., 2020). Biofilm can limit the capacity for flushing, as the it has a stabilizing effect on fine sediment by providing cover and increasing cohesion (Fang et al., 2017).

Designing a gravel pad that can be flushed of fines while resisting gravel erosion is a delicate balance, as the maximum size of placed spawning material is limited by the physical capabilities of the female spawners (Kondolf & Wolman, 1993). Salmon were also found to prefer recently deposited gravels post-flood events, as these gravels have less of a matrix, are cleaner and are easier to excavate (Poirier, 2003). These gravels are often near the threshold of mobility and more susceptible to mobility than their imbricated equivalents, which competes with the economic need for stable gravel augmentation installations.

2.2.3 Geomorphic effects of salmon spawning behaviour

Spawning salmon can have profound geomorphic effects on a stream by transforming them from pool-riffle sequences to a hummocky bed surface (Poirier, 2003). Their effects on sediment transport are also significant and the subject of much recent research. Hassan et al. (2015) hypothesized that effects of the mechanical particle sorting that occurs from salmonid spawning leads to competing geomorphic effects: (1) increased sediment stability and higher sediment entrainment thresholds and (2) increased sediment mobility. The former results from particle imbrication, surface bed coarsening, sediment sorting and higher drag from bedform roughness (Montgomery et al., 1996), while the latter is caused by the loosening of the grain packing, mixing of surface and subsurface layers, disruption of the armour layer, and prevention of armour layer re-development through annual mass spawning activities (Buxton, Buffington, Yager, et al., 2015; Gottesfeld et al., 2004, 2008; Hassan et al., 2008, 2011). The consensus of recent research points to the latter effect dominating most spawning sites, particularly at lake outlets where the net effect of high density Chinook spawning can be a primary agent dictating sediment mobility and bedform formation in the reach (Gottesfeld et al., 2008; Hassan et al., 2015).

Gottesfeld et al. (2004) found that the quality of substrate increases with successive repetitions of spawning activity through the selective export of fine sediment. This effect creates a positive feedback loop between gravel quality and spawning productivity—as gravel quality improves, more salmon survive the egg and fry stages, allowing them to reach adulthood where they then return to the spawning ground to propagate new generations. In gravel bed streams that are not yet scoured out, the greater spawner population then bioturbates more of the armour layers on the bed and creates more available spawning area. The authors also hypothesized that the removal of imbricated clasts reduces the necessary excavation effort for subsequent spawners, therefore progressively improving productivity. However, the study also found that the filling of the deep pockets in the reach and overall loosening of the bed through spawning activity also increases particle travel distances during nival floods, therefore suggesting an altered critical shear stress threshold in bioturbated streams.

2.2.4 Significance of lake outlets for salmon spawning habitat

The importance of Chinook salmon spawning at lake outlets was observed by Gottesfeld et al. (2008), who noted that 22 of 25 known Chinook spawning dune sites in BC were found in areas of abundant gravel supply, low bed slopes and within a few kilometres downstream of large lake. Sockeye salmon

also rely heavily on exorheic lakes—lakes that eventually connect to oceans—for rearing their fry and parr (Lennox et al., 2021). These lake features present an important milestone in the migratory lifecycle of this species, thus the proximity of available spawning habitat near the lake can thereby facilitate the early-life migration by sockeye to the lake. The prevalence of spawning and rearing sites at lake outlets suggests an appeal to fish fueled by a set of physical, chemical and fish behavioural controls (Gottesfeld et al., 2004, 2008; Sweeney-Bergen et al., 2021). The natural attraction of Chinook spawners to lake outlets supports a higher likelihood of usage for spawning habitat restoration actions in these reaches, thus making them desirable locations for such projects.

The lake exerts a strong influence on the downstream river dynamics in ways that likely encourage their use for spawning. The low water velocities in the lake allow it to trap sediment by causing suspended particles carried by upstream tributaries to settle out prior to reaching its outlet. Sediment transport rates downstream of lakes were found to only recover to 50% of upstream levels 2-4 km downstream of the lake, and may not even reach full recovery until 20 km downstream (Arp et al., 2007). The minimal sediment load exported from the lake is thought to help reduce fine particle accumulation in the outlet and improve maintenance of the substrate quality (Gottesfeld et al., 2008).

The lake also provides hydrologic stabilization by buffering the peak magnitude of flood events, which helps create stable rearing conditions for salmonid eggs and fry by reducing the potential scour caused by high flows (Hauer et al., 2015). The dampened flood flows allow Chinook to create multi-year spawning structures and encourage return in subsequent years (Gottesfeld et al., 2004). The natural stability of gravels in lake outlets is impaired only by the lack of upstream gravel supply, especially since most outlets do not have natural tributaries. In hydrologically altered watersheds where human- or climate-induced impacts are increasing peak flood magnitudes, gravel in lake outlets can be scoured out without being replaced by upstream sources. Without a new supply, the spawning productivity of the reach can thus decrease over longer timescales, and lead to overall decreases in salmonid populations in the river system. The degraded state of many lake outlets and the relatively higher probability of success render these reaches suitable target sites for restoration. Restoration at lake outlets is likely to have fewer maintenance requirements due to their hydraulic characteristics, while also having a higher likelihood for utilization by Chinook salmon spawners.

2.3 Hydraulics and sediment transport in accelerating flows

Modelling bedload transport at lake outlets is complex, because the non-uniformity of flow (Emadzadeh et al., 2010; Graf & Song, 1995), adverse bed slope (Chiew & Parker, 1994; Dey & Debnath, 2000; Parker et al., 2011) and spatially varying relative roughness (Afzalimehr, 2010; Dodangeh & Afzalimehr, 2022) affect the hydraulics and sediment mobility potential in the reach. Understanding the differences between the hydraulics of uniform and accelerating flow is therefore critical to obtaining realistic shear stress estimates in these environments.

2.3.1 Law of the wall and logarithmic velocity profiles under uniform flow

The idealized velocity profile of uniform flow is represented by the Prandtl-von Karman log-law distribution, or the law of the wall, written as:

$$\frac{u(z)}{u_*} = \frac{1}{\kappa}\ln\left(\frac{z}{k_s}\right) + Br = \frac{1}{\kappa}\ln\left(\frac{z}{z_0}\right) \quad [1]$$

where $u(z)$ is the mean point velocity (m/s) at a depth z (m) from the reference height z_0 (m), u_* is the shear velocity (m/s), κ is the von Kármán constant (typically given as 0.4), k_s is the roughness height (m) and Br is an integration constant (≈ 8.5). Shear velocity is related to shear stress as:

$$\tau_o = \gamma R_h S = \rho u_*^2 \quad [2]$$

where τ_0 is the wall shear stress (N/m^2), ρ is the fluid density (kg/m^3), R_h is the hydraulic radius and S is a slope parameter. S is defined as the bed slope, S_o, in uniform flow conditions but can be generalized as the friction or energy slopes in non-uniform or unsteady conditions. The shear stress derived from this equation is also sometimes referred to as the reach-averaged shear stress, as it is calculated from reach-averaged variables such as R_h and S. However, for wide channels or 2D models in areas far from the channel banks, R_h can be approximated by the average or local flow depths, h (m), respectively.

Plotting Equation [1] on semi-logarithmic axis with u/u_* on the x-axis and y/k_s on the y-axis yields a profile that is linear through most of the water column, except for the near-bed region where the normalized velocity drops back to zero. Extrapolation of the linear portion of the profile to $y = 0$ then allows for an estimation of shear velocity – this method was first proposed by Clauser (1956) and is at times referred to as the Clauser method.

2.3.2 Velocity profiles in accelerating flow

Lake outlets are best understood as non-uniform, gradually accelerating, adverse-slope flow. Although some field-based studies of accelerating flow exist (e.g., MacVicar & Roy, 2007; Whiting, 1997; Whiting & Dietrich, 1991), few were conducted in channels in spatially large-scale acceleration environments such as lake outlets. Most fundamental studies on this topic were completed in the laboratory (e.g., Afzalimehr & Anctil, 2000; Cardoso et al., 1991; Graf & Song, 1995; Song & Chiew, 2001; etc.), with only some studies using numerical methods (e.g., X.-F. Zhang et al., 2016).

Accelerating flows can be characterized by the streamwise pressure gradient parameter β, given as:

$$\beta = \frac{h}{\tau_o}\frac{\partial p^*}{\partial s} = \gamma \frac{h}{\rho u_*^2}\left(-S_0 + \frac{\partial h}{\partial s}\right) \quad [3]$$

where $\partial p^*/\partial s$ is change in the piezometric pressure head in the streamwise s-direction, and $\partial h/\partial s$ is the change in water depth in the streamwise direction (Cardoso et al., 1991; Clauser, 1956).

The β-parameter can be interpreted as a measure of the extent of acceleration or as a negative ratio of shear stresses calculated using the depth-slope and the shear velocity definitions given in Equation [2]. The parameter has a value of -1 representing uniform flow and increasingly negative values representing greater acceleration. One of the characteristics used to define equilibrium flow is the spatial and temporal invariance of β (H. W. Coleman et al., 1977; Rotta, 1962).

Equilibrium flow, also termed self-similar flow, refers to scenarios where the normalized mean velocity profiles collapse into a single relationship (Cardoso et al., 1991). This type of flow arises after the flow stabilizes in a channel where the geometric characteristics remain constant between different cross-sections, such that the acceleration gradient becomes constant in the channel.

Cardoso et al. (1991) showed the impact of slope changes on velocity profiles in their laboratory experiment that modelled the transition between uniform flow on a horizontal bed to an adversely inclined smooth plate. The self-similarity in velocity profiles is not immediately attained as flow begins to accelerate but is instead developed through the inclined section, as shown in Figure 2. The authors noted the existence of three types of velocity profiles: uniform flow, where the velocity profile closely follows the log law; flow re-establishment, consisting of the section between the immediate upstream to a short distance downstream of the slope change, where the profiles maintain the 1/κ slope but begin shifting downwards; and the accelerating flow region, where the log law is

valid near the wall but shows strong deviations in the outer layer. The deviations in both the flow re-establishment and accelerating zones tend to be below the theoretical relationship.

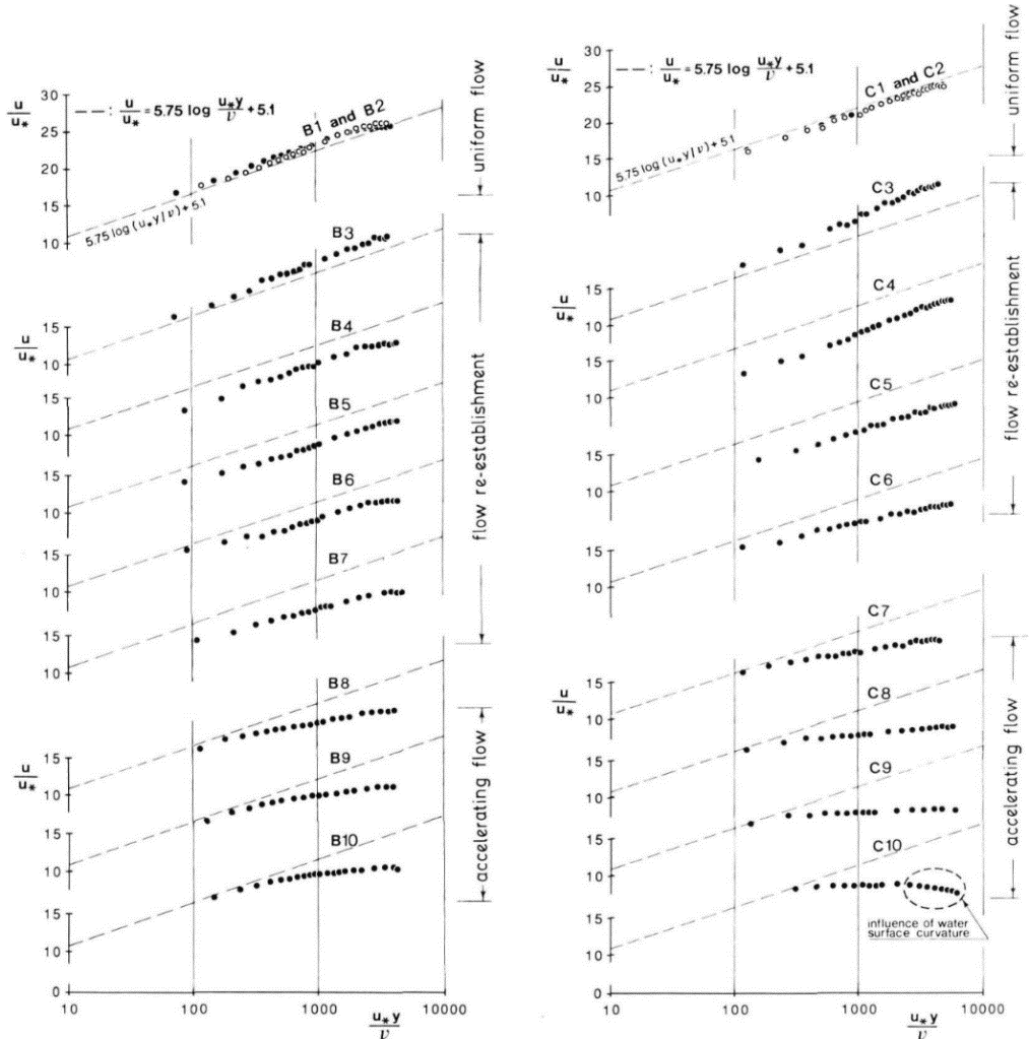


Figure 2 Progression of velocity profiles transitioning from uniform flow over a smooth horizontal bed to accelerating flow over an inclined plate angled 3º (B, left) and 7º (C, right). From Cardoso et al. (1991).

These results point strongly to the existence of at least two distinct layers in accelerating flow: the near-wall layer where the logarithmic law of the wall is valid and an outer layer that defects from the theoretical profile. The near-wall layer was termed the overlap layer by Sturm (2010) to reduce confusion with the inner viscous sublayer (Figure 3).

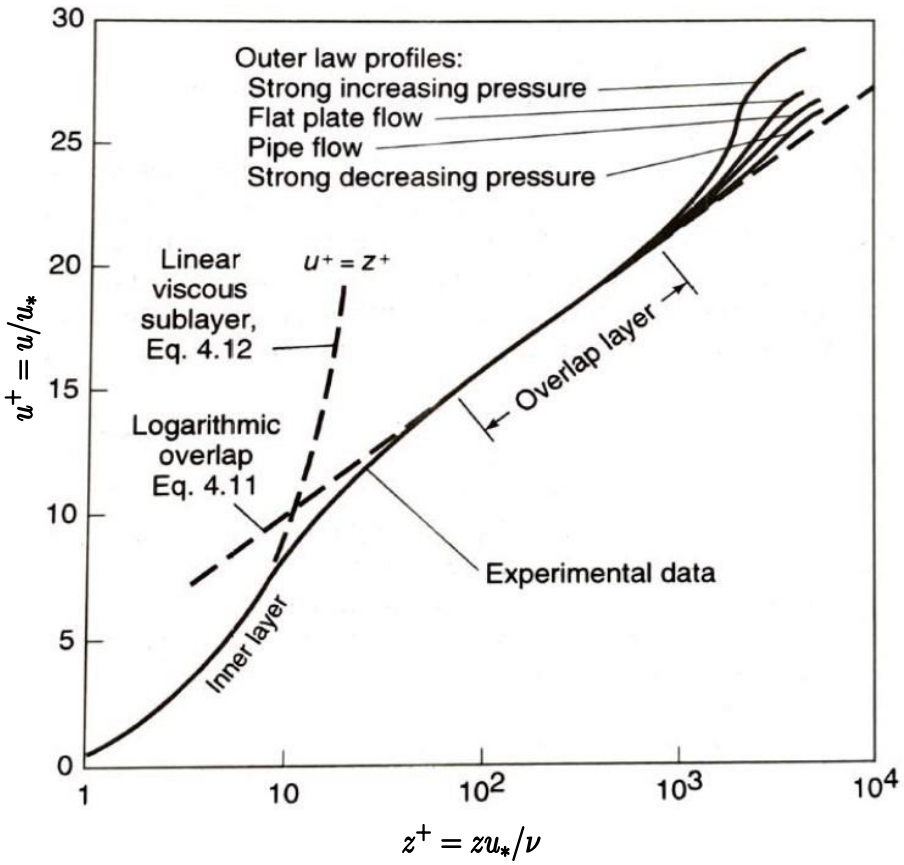


Figure 3 Generalization of velocity profiles in fully turbulent flow. From Sturm (2010).

Equilibrium flow is rarely achieved in nature due to the inherently random geometries of natural channels but is the most commonly type of flow studied in laboratory-based accelerating flow experiments. The extrapolation of these laboratory studies on practical applications can therefore be contentious due to the non-equilibrium status of natural channels. The presumed lack of equilibrium in natural channels suggests that the development of the overlap layer may not fully form in lake outlet environments and that the flow may semi-permanently remain in the flow re-establishment phase. Uncertainty over the extent of the deviation from the log law in natural accelerating channels makes the use of the Clauser method difficult to justify without proper verification. Deviations from the log law can be difficult to quantify due to the dependence on multiple parameters but they are generally described by two phenomena: the wake and dip effects.

2.3.2.1 Wake phenomenon

The wake phenomenon is caused from pressure gradients near sidewalls and in narrow channels, creating deviations in the velocity profile distribution from uniform flow. The Coles wake model describes these deviations between z_0 and δ:

$$\frac{U_c - u}{u_*} = -\frac{1}{\kappa}\ln\left(\frac{h}{\delta}\right) + \frac{2\Pi}{\kappa}\cos^2\left(\frac{\pi h}{2\delta}\right) \quad [4]$$

where U_c is the maximum velocity in the flow column (m/s), δ is the depth of U_c relative to z_0 (m), and Π is the wake parameter (White, 1991). The first term in the equation accounts for the theoretical logarithmic velocity profile while the second term is the wake function and is used to characterize deviations from the law of the wall.

The wake parameter Π is generally treated as a curve-fitting parameter that is estimated based on detailed velocity measurements in a water column. The reported values of Π vary considerably depending on experimental conditions, but most researchers obtained values that were $-1.5 < \Pi < 0$ for accelerating flows over smooth, sand and gravel beds (Cardoso et al., 1991; Kironoto & Graf, 1995; T. Song & Chiew, 2001; Xiao et al., 2023). The predominantly negative values agree with the findings in Cardoso et al. (1991) that showed that the velocity defects under accelerating flow generally deviate downward from the log law. However, experimental Π-values were not universally observed to be negative. In the Afzalimehr (2010) study, the author used a cobble bed to model the effects of moderate submergence. Regrettably, the author did not report the Π-values in his study, but he observed an upward deviation from the log law, which implies a positive wake effect. The author hypothesized that the positive divergence was caused by flow contraction over the leading edge of the cobbles in the bed. While this may be true, low- to medium-submergence studies are rare, thus there has yet been an attempt to corroborate this theory. This hypothesis also does not explain the positive Π-values that were observed in some experiments by Song and Chiew (2001) for their gravel bed and by Xiao et al. (2023) who used a smooth bed. The reason for the discrepancy between positive and negative wake parameter values therefore remains unclear, as there are no evident commonalities between these studies that distinguish them from others. The dependency of Π on various parameters, however, has been theorized.

Early researchers purported a positive power law relationship between Π and β (Cardoso et al., 1991) but the current consensus is in favour of a linear relationship (Kironoto & Graf, 1995; T. Song

& Chiew, 2001; Xiao et al., 2023). Π has also been shown to be dependent on the width-depth ratio, b/h, and roughness (T. Song & Chiew, 2001). More recently, Xiao et al. (2023) proposed a conceptual model, shown in Figure 4, where Π varies according to Π, b/h and the Reynolds number, Re. Based on this model, Π is a function of Re and inflects between a set of values based on a threshold Re value. The function undergoes vertical shifts based on a linear relationship with β, and is subject to another vertical shift of 0.25 depending on the two-dimensionality of the channel which is governed by the aspect ratio threshold ξ. The authors suggested a threshold of $\xi \approx 5$ on smooth beds and $\xi \approx 3.5{\sim}4$ for rough beds due to the weaker secondary currents on coarse beds.

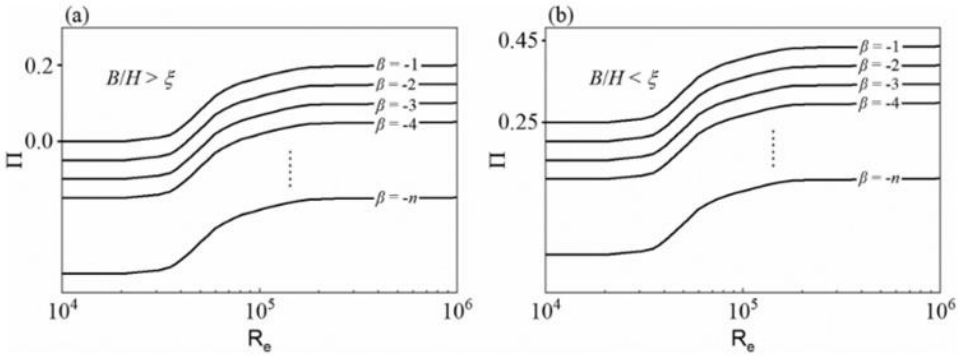


Figure 4 Conceptual model of the dependence of Π on β, Re and b/h. From Xiao et al. (2023).

Given the difficulty in parameterizing Π and capturing velocity defects with existing models, other wake models have also been proposed by various accelerating researchers to better fit their data—some are modifications of the original log law that do not use the wake function (Alfadhli et al., 2013; Yang et al., 2006), while others modify the Coles wake model itself (Cardoso et al., 1991). While other equations that did not employ the wake function were later proposed by various researchers (Alfadhli et al., 2013; Cardoso et al., 1991; Yang et al., 2006), inconclusive evidence of their utility in characterizing various types of accelerating flows have precluded their widespread acceptance.

2.3.2.2 Dip phenomenon

The dip phenomenon refers to the observation that the maximum velocity in a flow column is at times located below the free surface. The dip phenomenon is more prominent in accelerating flows than uniform or decelerating flows under similar channel geometries. Kironoto and Graf (1995) observed that accelerating flow profiles typically appear “fuller” with a steeper velocity gradient near the bed, resulting in the attainment of the maximum velocity closer to the bed and a deeper velocity dip than

uniform or decelerating flow under comparable channel conditions. This phenomenon was theorized to occur due to downward secondary currents in the upper layer of flow. The location of the dip corresponds to the location of zero Reynolds shear stress, which arises due to the intersection of the upward flow coming off the bed and the downward vertical velocity from the upper flow cell (Nezu, 2005; Yang et al., 2006; Yang & Chow, 2008). The negative depth gradient encourages downward secondary currents to form, resulting in an increased prevalence of negative free surface vertical velocities—and therefore more prominent dips—than in uniform flow. The dip phenomenon only occur in channels with low width-depth ratios where flow acts three-dimensionally due to the effects from the sidewalls (Yang et al., 2006). There is yet a lack of consensus on a single preferred model that is universally applicable, but a recent study that compared various equations found that the best fit was found with the log-wake-dip law which includes the dip term and the dip parameter α:

$$\frac{u}{u_*} = \frac{1}{\kappa}\ln\left(\frac{y}{y_0}\right) + \frac{2\Pi}{\kappa}\sin^2\left(\frac{\pi}{2}\frac{y}{\delta}\right) + \frac{\alpha}{\kappa}\ln\left(1 - \frac{z}{h}\right) \quad [5]$$

Xiao et al. (2023) proposed the same ξ-thresholds for the dip parameter α as those proposed for the wake parameter Π ($\xi \approx 5$ on smooth beds and $\xi \approx 3.5{\sim}4$ for rough beds), where $\alpha = 0$ when $b/h > \xi$ and $\alpha = 0.67$ otherwise. However, this recommendation was developed based on smooth, sand and gravel beds. Conversely, velocity profiles approach a vertical line above $z/h > 0.4$ in channels with intermediate relative submergence (i.e., high relative roughness) and $b/h \approx 2$, therefore indicating the existence of two layers of flow in such channels (Afzalimehr, 2010). The strong influence of relative roughness on the bed appears to play a non-negligible role on the strength of the secondary currents and the occurrence of a dip.

2.3.3 Reynolds stress

Applying a Reynolds decomposition to velocity timeseries allows for the splitting of the velocity flow field into its mean and fluctuating components. Reynolds stress is the product of the streamwise and vertical velocity fluctuations and is used to describe turbulent fluctuations in fluid flow. Similar to the Clauser method, shear velocity under uniform flow can also be estimated using the linear extrapolation of the normalized Reynolds stress (RS) profiles to the bed. The Reynolds stress method of estimating shear velocity is given the following relationship:

$$-\frac{\overline{u'z'}}{u_*^2} = 1 - \frac{z}{h} \quad [6]$$

where $-\overline{u'w}$ is the RS (m^2/s^2), or the stress caused by the mean turbulent velocity fluctuations, $\overline{u'}$ and $\overline{w'}$ (m/s), in the streamwise and vertical directions.

However, research has shown that RS profiles are not linear in non-uniform flow, with most studies showing that the RS profile is concave in accelerating flow due to the negative pressure gradient, which in turn causes a negative RS gradient (Afzalimehr & Anctil, 2000; Cardoso et al., 1991; Kironoto & Graf, 1995; T. Song & Chiew, 2001; Yang et al., 2006; Yang & Lee, 2007). However, Afzalimehr's (2010) experiments conducted in intermediate relative submergence over a cobble bed showed convex RS profiles, with the maximum value occurring at $z/h \approx 0.15$.

Afzalimehr (2010) also found that near-bed RS values were highly sensitive to discharge, but RS values in the upper half of the flow were largely invariant to flow rate. The findings from this study directly contradict many findings from previous research, therefore suggesting that patterns in velocity fluctuations are highly dependent on relative roughness. Many of these effects may result due to the importance of form drag over skin friction in flows with high relative roughness, however, more research is required to draw conclusive results, especially since there has yet to be an attempt to replicate the experiments from Afzalimehr (2010) which use a high relative roughness. These experiments, however, are directly applicable to many coarse-bed rivers that may have been historically subject to scour or armouring.

Regardless of the direction of concavity, the non-linear RS profiles precludes the use of the RS method to estimate shear velocity. Dey & Lambert (2005) proposed a momentum correction factor derived from the Saint-Venant equation (SVE) for motion for non-uniform unsteady flow in open channels. The authors then incorporated the correction into equations for time- and space-variable non-dimensional Reynolds shear stress and mixing length. Conversely, Yang et al. (2006) hypothesized that the nonlinearity resulted from the non-zero wall-normal velocity $\bar{v}$, and Yang and Lee (2007) found that a linear relationship could be obtained by modifying Equation [6] to include a momentum flux term $-\bar{u}\bar{v}$, shown in Figure 5.

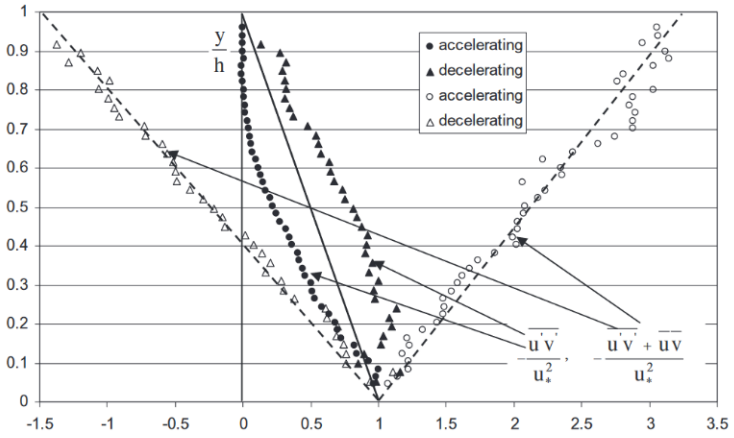


Figure 5 Measured Reynolds stress distribution with momentum flux modifications. From Yang and Lee (2007).

This relationship indicates that the total shear stress in non-uniform flow is a sum of two linear distributions, of which one is the turbulent shear stress produced by the boundary and the other is the momentum flux induced at the upper boundary due to the non-zero vertical velocity. Yang & Lee (2007) describes this relationship as:

$$-\frac{\overline{u'w'}+\bar{u}\bar{w}}{u_*^2}=1-\frac{z}{h}+b_{RS}\frac{z}{h} \quad [7]$$

where the slope of the RS-momentum profile, B, is given as:

$$b_{RS}=-\frac{\bar{u}_h w_h}{u_*^2}=-\left(\frac{\bar{u}_h}{u_*}\right)^2\frac{\partial z}{\partial x} \quad [8]$$

The parameter b_{RS} was found to vary between experimental conditions and was always positive in accelerating flow. As $b_{RS}>0$ in accelerating flow, $\bar{v}$ must therefore be negative, which agrees with the theory that accelerating flows are subject to strong downflows (Yang et al., 2006; Yang & Lee, 2007). Yang et al. (2006) noted that the RS was negligible at $z/h>0.75$ compared to the momentum flux term, thereby indicating the dominance of momentum in the upper portion. At the bed however, $\bar{v}$ is zero, thus the momentum flux term is also zero. The findings by Yang et al. (2006) and Yang and Lee (2007) demonstrate the importance of momentum flux in accelerating flow, and provide an alternative method of calculating shear stress from RS values in three-dimensional models.

2.3.4 Shear velocity

Shear velocity under uniform flow can be calculated in various ways, including the classic depth-slope definition shown in Equation [2], the Clauser method, the RS extrapolation method. Variations on these methods have been compared and applied to accelerating flow (Afzalimehr & Anctil, 2000; Cardoso et al., 1991; Graf & Song, 1995; Yang & Lee, 2007), while new methods have also been proposed (Afzalimehr & Anctil, 2000; Kironoto & Graf, 1995). Afzalimehr and Anctil (2000) suggested that the Clauser method is highly sensitive to the definition of the reference level, and instead supported the use of a boundary characteristics approach.

Regardless of approach, most of these methods are useful only for three-dimensional models, except for the classic depth-slope method, which is applicable to 1D, 2D and 3D models. This method can be redefined for non-uniform flow by defining the slope as the friction slope using a variation of the Saint-Venant momentum equation, as given in Equation [9] (T. Song & Chiew, 2001).

$$u_* = \sqrt{gR_h\left[S_o - \frac{\partial h}{\partial s}(1 - Fr^2)\right]} \quad [9]$$

where g is the gravitational acceleration constant (m/s^2) and Fr is the Froude number. In 2D models, the hydraulic radius R_h is replaced by the depth, h. For 1D models however, Song & Chiew (2001) found that the use of the hydraulic radius was generally preferred as it accounts for sidewall effects.

2.4 Critical shear stress dependencies

The critical bed shear stress refers to threshold of shear stress acting on a streambed over which a grain of a given size would be expected to mobilize in a channel. The dependency of critical shear stress on grain size and grain size distribution has been well-documented (Buffington & Montgomery, 1997; Wilcock & Crowe, 2003), however the competing interactions between other influential factors such as slope (Chiew & Parker, 1994; Dey & Debnath, 2000; Parker et al., 2011), bioturbation potential (Gottesfeld et al., 2008; Hassan et al., 2008, 2011, 2015) and presence of algal biofilm (Fang et al., 2017; Stone et al., 2011) are poorly understood.

2.4.1 Bed slope

For accelerating flows which often occur under adverse slope conditions, the influence on the bed slope on the critical shear stress may be important. The impact of slope on sediment mobility are

particularly important in mountainous or meandering natural channels that have complex three-dimensional bathymetry, as the channel often slopes in both the streamwise and lateral directions. The dependence of entrainment thresholds on bed slope has been well documented (Chiew & Parker, 1994; Dey, 2003; Dey & Debnath, 2000; Parker et al., 2011). Chiew and Parker (1994) noted that most incipient motion studies were conducted under nearly horizontal bed slopes and ignore the gravitational effects on particles under steeper slopes. They proposed an equation to correct for the effects of streamwise bed slopes and suggested that the critical threshold for motion is negatively correlated with bed slope, such that negative slopes have a higher u_{*c} value than horizontal or positive slopes. However, the authors found that the equation slightly underestimated the measured u_{*c} values for adverse slopes. Dey & Debnath (2000) repeated these experiments and found that the equation was able to adequately represent the variation in shear stress on bed slopes as adversely inclined as $-15°$. Dey (2003) advanced this topic by investigating the effects of combined transverse and streamwise sloping beds on critical shear thresholds and showed that the relative critical threshold is negatively correlated with both the transverse and longitudinal slopes. These findings agree with the conceptual understanding that a particle resting on a steep slope in the streamwise and/or transverse directions would be more prone to movement.

Parker et al. (2011) later noted however, that grains in steep mountainous rivers are not necessarily more likely to move than their counterparts in milder sloped streams, and that such channels instead often experience elevated critical bed shear stress values. They list numerous factors that may result in this positive relationship, such as the presence of stabilizing bed structures resulting from the interlocking of the coarse grains, the consequence of the hiding effect in streams with large particles, the reduced shear stress available for sediment transport resulting from the increased importance of form-based drag, the reduced weight of water in turbulent and highly aerated slopes, and the influence of slope on relative roughness and flow resistance.

2.4.2 Bioturbation

As discussed in Section 2.2.3, the disruption of the bed armour layer through spawning activity can dictate the morphology of the reach. Hassan et al. (2015) suggested that there exists an interplay between spawning- and flood-driven transport that results in seasonal mobility patterns. They observed that spawning by small-bodied salmon disrupts armouring, which decreases the dimensionless critical shear stress and enhances mobility by floods in the postspawning season. Nival

floods then re-armour and coarsen the streambed, thereby increasing the boundary shear stress and reducing the area of bed mobility. However, excess armouring is detrimental to egg survival rates, as Dusterhoff et al. (2017) observed that their sites with lower shear stress and greater coarse particle exposure under bankfull flow were subject to greater scour depths under these flows. They found that the redds with high D_{84}/D_{50} ratios experienced greater localized coarse grain mobility and bed scour. Thus, heavily armoured reaches or relatively high D_{84}/D_{50} ratios may increase the vulnerability of shallowly buried eggs to washing out.

Buxton, Buffington, Yager, et al. (2015) constructed physical redd structures in a flume study—they observed that shear stresses were up to 41% higher, and the critical shear stress threshold was 22% lower on the redd tailspill than the adjacent unspawned bed. Both results indicate that redd structures are less stable and more likely to mobilize compared to the adjacent unspawned bed. The results from literature suggest that a successful gravel enhancement attracts fish to spawn in greater densities may reduce the critical shear stress thresholds in the reach required for incipient motion.

2.4.3 Epilithic biofilm

The effect of biofilm on cohesive sediments have been studied in marine and lacustrine environments. The presence of biofilm has been shown to increase the ability of the sediment to resist shear—this effect has been termed “biostabilization”. The stabilization effect is significant even for cohesive fluvial sediment in freshwater environments, and has been shown to be a primary controller of bed stability and erosion potential in such scenarios (Droppo, 2009).

The significance of biofilm in lacustrine regions extends to their outlet streams, where the relatively slow velocities and well-lit conditions can encourage the growth of algae (Myers et al., 2007). Fang et al. (2017) developed an integrated 3D numerical model to simulate the effects of biofilm on cohesive sediment erosion thresholds. They found that biofilm increased mean velocity and decreased near-bed turbulence intensity through a reduction in bed resistance. These effects are coupled with an increase in incipient motion thresholds, increased settling velocities and a noticeable difficulty in resuspending deposited sediments. Biofilm-populated reaches may therefore increase the propensity for fine sediment accumulation in such environments.

Most studies on this topic focus on cohesive sediments, with very few studies on the effects of biofilm on gravel bed rivers where algae may be present in sufficient quantities to affect the hydraulics of the stream. Algae growing on river stone fall within the category of microorganisms

that are collectively referred to as “epilithic biofilm”. Epilithic biofilm has been shown to hold a complex relationship with stream hydrodynamics, as its age and abundance can increase or decrease drag at the bed, while the turbulent characteristics in turn can either promote its growth or encourage its detachment and subsequent transport (Graba et al., 2010).

The poorly understood effects of epilithic biofilm on gravel bed rivers limits the assessment of gravel augmentation suitability, as the relative stability of gravel in these environments compared to reaches without biofilm cannot be determined with certainty without site-specific studies. Furthermore, biostabilization on fine sediment increases the likelihood of physical clogging and bioclogging of the gravel interstices, which may impact hyporheic flow and the viability of buried eggs (Shrivastava et al., 2020). Algae may have an impact on salmon spawning, but salmon spawning itself may impact algae persistence. The digging of redds disrupts the surficial layer on the bed, therefore it must follow that this digging action also disrupts algae growth in some way. The cyclical nature of these impacts are unknown and is a current gap in literature on salmon spawning in algae-dominated reaches.

2.5 Application of numerical models for salmon habitat restoration design

2.5.1 Overview of numerical models for hydraulic simulation

The use of numerical models to predict fluvial responses to perturbations or restoration initiatives is becoming increasingly common due to continuous developments in model and computational efficiency, and the comparative cost-effectiveness of desktop studies relative to physical field or laboratory testing. The selection of three-dimensional (3D), two-dimensional (2D) and one-dimensional (1D) models depends on the level of accuracy and resolution required for these applications, as well as the unique conditions of each site. 2D hydrodynamic models employ depth-averaged velocities in their formulation, and thus do not account for any vertical flow or mixing. Conversely, 1D models apply Manning’s equation with empirical adjustment factors to account for effects from the sidewall or from the cross-sectional shape (Najafabadi & Afzalimehr, 2020).

In industry, 1D models are most common due to the low entry level for expertise and the widespread application of river modelling for flood and risk assessment. For high-level purposes that do not require precise spatial resolution, 1D models may be adequate in obtaining the desired results. For example, a U.S. Geological Survey (USGS) study evaluating restoration alternatives at a lake

outlet employed a 1D Hydrologic Engineering Center River Analysis System (HEC-RAS) model, as the authors were only interested in simulating river-lake flow exchanges without extrapolating to sediment transport or aquatic habitat predictions (Rounds et al., 2020). Other studies commonly use the 1D Physical Habitat Simulation (PHABSIM) developed by the USGS which links streamflow to habitat suitability (Milhous & Waddle, 2012). However, increased dimensionality in models offer improved accuracy in simulated results as they better account for mechanistic processes than their 1D counterparts. This characteristic allows multi-dimensional models to account for local variations in bed topography and roughness, and transverse flows and eddies (Najafabadi & Afzalimehr, 2020).

The use of 3D models allows for the greatest level of process representation, and when applied correctly, provides more accurate hydraulic and sediment transport predictions. However, such models require higher quality datasets to build the model and assess the accuracy of its predictions. These models are heavily limited by the resolution of the collected topographic and the depth and velocity profile data used to define the boundary conditions (Lane et al., 1999). The estimation of this information through interpolation or extrapolation can present levels of uncertainty that may be greater than the usefulness and reliability of the model.

Conversely, 2D models are less sensitive to topographic variations and may be preferred in scenarios with limited bathymetry data, though they still require more detailed calibration and validation data than 1D models (Lane et al., 1999). The depth-averaging simplification also reduces their computational load compared to 3D simulations, which can provide significant time-savings while often providing reasonably accurate depth and velocity predictions (Füstös et al., 2021). 2D models however, are significantly more sensitive to the prescribed bottom roughness parameter than their 3D counterparts (Lane et al., 1999). Lane et al. (1999) found that much higher roughness values are required to accurately predict velocities in 2D models than would be expected from field-based estimates or an equivalent 3D model. Bottom roughness in 2D models must account for a greater proportion of the total shear due to the depth-averaging, which eliminates the consideration for shear between fluid layers, vertical mixing, and form-based drag. The increased (and potentially unrealistic) roughness directly results in overpredicted shear stress values which arises as an artefact of the roughness-based shear stress calculations ubiquitously applied to 2D models (Füstös et al., 2021).

2.5.2 Applications to salmon habitat restoration

Despite the popularity of 1D models in engineering practice, these models are incapable of accounting for transverse velocities and eddies (Najafabadi & Afzalimehr, 2020), which are important components in determining the flow fields that govern aquatic habitat (Brown & Pasternack, 2009). Even in reaches with limited suitable spawning area, low-density spawners may be able to find small pockets of suitable bed texture and hydraulic features where these characteristics differ from reach-averaged conditions (Cienciala & Hassan, 2013). Cienciala & Hassan (2013) noted that in such scenarios, a finer resolution approach such as a 2D or 3D model is required to accurately predict spawning suitability, although coarse resolution 1D approaches may be adequate for reaches with high density spawning action. Conversely, Brown & Pasternack (2009) found that 1D models are heavily limited in shallow gravel-bed rivers with low-to-moderate relative submergence, which represent the most common morphology for gravel augmentation sites. The authors also observed that 1D models tended to overpredict the quality and spatial extents of suitable spawning habitat, thereby painting a deceptive picture of the health of the aquatic ecosystem for water resource managers. Therefore, while 1D models may provide useful predictions on the watershed scale, there are considerable risks when employing them to evaluate reach-level habitat restoration initiatives.

Few studies at salmonid spawning sites employ 3D models, with most instead electing to utilise 2D models (Hauer et al., 2020). This is largely attributed to the lack of sufficiently high resolution topographic information to calibrate and validate 3D models at the necessary scales, especially given the sensitivity of 3D models to minor bathymetric changes (Pasternack et al., 2004). Comparatively, 2D models were found to adequately represent the characteristic flow and depth patterns required for the assessment of aquatic habitat suitability (Füstös et al., 2021; Harrison et al., 2022).

Although 2D models are considered standard for gravel augmentation projects, the methods used to translate hydrodynamic simulations to sediment transport predictions vary significantly. Traditionally, hydrodynamic models are used to calculate shear stresses from flow and channel parameters, which can then be combined with sediment transport equations to predict areas of erosion or deposition. The sediment transport equations can be applied post-simulation for steady flow models, but can also be directly incorporated into model calculations through the coupled Saint-Venant-Exner equations, which account for topographic changes in unsteady simulations. Juez et al. (2016) used the morphodynamic approach and found it to be effective for replicating overall trends, but not for

sediment clustering. More recently, Arnaud et al. (2023) proposed a method that derived particle trajectories based on a hydrodynamic model, allowing for the simulation of individual tracers.

However, there is a consensus in studies pointing to the consistent overprediction of shear stress magnitudes in 2D models compared to measured and 3D-modeled values despite following similar spatial trends (Füstös et al., 2021; Najafabadi & Afzalimehr, 2020). This systematic error is a major limitation for uses that require detailed characterization of sediment transport dynamics, as shear-based estimates of scour and interstitial fines flushing would likely be overpredicted. These 2D models are thus restricted in their ability to delineate scour areas but may be sufficient to make qualitative comparisons between when predicting areas of relatively greater scour within a reach.

2.5.3 Characterizing sediment transport using tracers

The validation of sediment transport models through field-based monitoring is challenging, in part due to the difficulty in quantifying sediment transport rates or mobility using available techniques. Various methods of evaluating of sediment transport have been proposed, including approaches using Difference of DEM (DoD) (e.g., Wheaton et al., 2010), sediment tracers (Arnaud et al., 2023; Mörtl et al., 2023; Papangelakis & MacVicar, 2020), bedload monitoring stations (Iannetta, 2020), geographic information systems (GIS) mapping coupled with in-field measurement (Hauer et al., 2020) and the combination of RPAS surveys with active ultra-high frequency (a-UHF) transponders (Cassel et al., 2020). However, most methods are only applicable for estimating average transport rates during post-placement monitoring and cannot validate models that seek to predict mobility for individual grain sizes.

Of these methods, tracers are expected to be most useful for evaluating or monitoring gravel augmentation designs, as each tracer can be sized to represent a grain size fraction of interest. This qualities makes tracers suitable for analysis through the surface-based fractional transport models such as those proposed by Wilcock & McArdell (1993) and later Wilcock & Crowe (2003), which is considered the most representative and commonly applied model for gravel-bed rivers. The use of the Wilcock & Crowe (2003) is now standard practice for engineering design and is incorporated in many common hydraulic models such as HEC-RAS and TELEMAC.

These fractional transport models purport a distinction between partial and full mobilization for grain fractions, where incipient motion thresholds can predict the mobilization of some grains in a size class but mobilization of the full size class only occurs at roughly two times its critical shear

stress (Church & Hassan, 2002). This difference means that the mobility of an individual grain is not deterministically determined by whether the local shear stress exceeds a critical threshold but also depends on an unknown probability distribution function. Tracer stones capture the effects of the inherently stochastic nature of sediment transport, as each tracer represents a particle of known characteristics and can be uniquely identified through its tag number. The tracking of individual particles through flow events can provide useful conclusions on critical incipient motion thresholds, size-selectivity in gravel transport, dispersion patterns, and transport pathways (Arnaud et al., 2023). Further conclusions can be drawn on trends related particle shape, density or other physical attributes, which influence particle mobility and velocity (Cassel et al., 2021). Other methods of evaluating sediment transport such as DoD or survey-based approaches rely on elevation changes over a spatially wide area and do not provide information on size-based transport or partial mobilization of specific size classes. These methods may be useful for watershed assessments but cannot capture local relationships between flow and resultant sediment transport (Papangelakis & MacVicar, 2020).

Validation of 3D models with tracers have shown good agreement between model predictions and field observations from tracer data (Biron et al., 2012; Liedermann et al., 2013). Arnaud et al. (2023) compared the tracking of a high number of tracers to probabilistic and 2D numerical approaches for predicting mobility. They found that the model could deterministically simulate realistic displacement distributions, but failed to completely reproduce the shape of the tracer cloud due to the influence of stochastic processes that were not captured in the model. The findings in this study supported the use of 2D models for designing gravel augmentation given their ability to incorporate high-resolution hydrodynamic forces on sediment transport but highlighted that these models still require the addition of a probabilistic approach to achieve accurate and representative results (Arnaud et al., 2023). These promising qualities make tracers a common tool used in gravel augmentation projects (Arnaud et al., 2017, 2023; Chardon et al., 2021).

Chapter 3
Methods

3.1 Study area

3.1.1 Watershed context

Muchalat River is a tributary of Gold River on the west coast of Vancouver Island (a map of the watershed is included in Appendix A). Gold River is a key passageway and habitat for multiple anadromous salmonid species, as it drains into Nootka Sound which eventually flows into the Pacific Ocean. The watershed has been subject to extensive anthropogenic alterations over the last 100 years, including heavy logging in the upper portion and loss of estuary habitat from filling and diking practices along surface water bodies due to industrial, road building and forest harvesting activities (COSEWIC, 2021; Pike et al., 2010; West et al., 2023; Winkler et al., 2010). These human activities have caused the decline of multiple native salmonid populations in the watershed, including Chinook salmon (*Oncorhynchus tshawytscha*), Coho salmon (*O. kisutch*), sockeye salmon (*O. nerka*), chum salmon (*O. keta*), and steelhead/ rainbow trout (*O. mykiss*).

Muchalat Lake, a 5 km^2 lake, is located along Muchalat River. The lake is supplied by Upper Muchalat River and Oktwanch River, with a drainage area of approximately 219 km^2 (West et al., 2023). Upper Muchalat River drains the neighbouring mountain peaks on the west side of the lake, where small glacial units were observed to persist even during the summer field visits. The presence of the glaciers in the summer suggest that the system is both snow- and rain-fed.

The lake drains into Lower Muchalat River, which then flows into Gold River at a confluence located approximately 6.5 km downstream of the lake and 7.5 km upstream of the town of Gold River. Chinook salmon were observed to spawn in the reach immediately downstream of Muchalat Lake, both by the MMFN community and through imagery captured by an RPAS flight in 2021 (West et al., 2023). Despite the existence of some spawning activity, the quality of the spawning habitat on Muchalat River between Muchalat Lake and the Gold River confluence is currently poor with relatively little spawning areas remaining. The degradation of the streambed is thought to be driven by the higher peak flows associated with watershed logging activities and climate change (West et al., 2023).

The prevalence of clearcut logging in the watershed increases sediment supply to the lake through hillslope failure or the erosion of gravel access roads, which can be connected to the project reach under sufficiently high flow events. Figure 6 shows a map of the study area in the context of nearby mountain peaks and anthropogenic activity.



Figure 6 Site context over a Google Earth basemap. Flow enters the lake through the Oktwanch and Upper Muchalat Rivers and exits through the study site on Lower Muchalat River.

3.1.2 Site investigations

A total of five field visits were completed for this project including three that were completed by the Ecofish project team and/or the MMFN only. The Ecofish field trips were generally completed with local field technicians from MMFN or NSWS and were intended to primarily collect hydraulic data using an Acoustic Doppler current profiler (ADCP) and establish local benchmarks (BM). Conversely, UW-led field trips were intended to implement tracer stones, complete a remotely piloted aircraft system (RPAS) survey and further the research objectives. The purposes and dates of each field trip are summarized in the following table.

Table 1 Summary of completed field trips and collected data

Field trip	Label	Date	Participants	Purpose
Ecofish field trip 1	EFT1	2022/07/07	Ecofish, MMFN/NSWS	Establish BMs; streamwise and cross-sectional ADCP transects; install gauges
UW field trip 1	WFT1	2022/07/26 - 2022/07/29	UW, Ecofish, MMFN	Prepare and seed tracer stones
Ecofish field trip 2	EFT2	2022/09/08	Ecofish	ADCP and USGS Pygmy mechanical velocimeter transects
Ecofish field trip 3	EFT3	2023/01/14	Ecofish	ADCP transects; download gauge data
UW field trip 2	WFT2	2023/08/04 - 2023/08/06	UW, UBC	Find and survey tracer stones; collect downstream bathymetry; RPAS images

3.1.3 Study area

The project site is located on the lower Muchalat River at the outlet of Muchalat Lake. The study reach extends from 100 m downstream of the lake boundary to a point located approximately 600 m downstream. The study area is shown on the RPAS imagery of the reach in Figure 7.

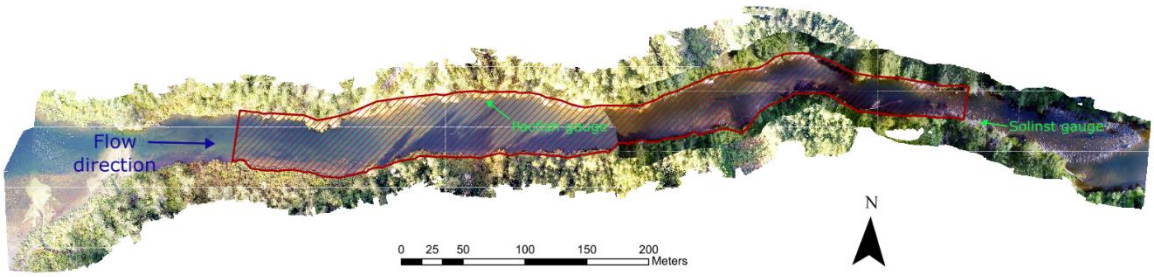


Figure 7 RPAS imagery of the study area (red hatched zone). Water flows left to right.

A power line runs across the river in an electrical utility corridor approximately 50 m upstream of the bend. Sediment deposits on the left bank of this section suggest that this is a sediment supply area. According to MMFN, these deposits either result from a former bridge that was temporarily mounted to install the power line or from the gravel roads running 40 m north and 190 m south of the river.

3.1.4 Hydraulic characteristics

Lake outlets are unique geomorphological features within a watershed because they can be subject to flow, sediment and wind loadings that are unlike the rest of the river system. The definition of lake outlet can be unclear, as hydraulic characteristics along the stream can vary significantly based on the spatial distance from the lake boundary.

The study reach is located immediately downstream of the lake, where the bed slope is mostly adverse, and the water surface is relatively non-varying along the flow direction. The hydraulics in the study reach reflects the transitional environment between a very deep and near-lacustrine fluvial section to a pool-riffle morphology further downstream. The transition to pool-riffle sequences is marked by a crest at the apex of a river bend located approximately 100 m upstream from the downstream boundary of the study site. The streambed rises by about 5 m within the 250 m section upstream of the crest, which creates a convectively accelerating flow. A deep pool is located downstream of the crest with a maximum depth of nearly 5 m below the top of the upstream crest. This pool is approximately 50 m long and is followed by a short higher elevation riffle-like stretch that forms the downstream study boundary.

The proximity to the lake and geographic location on Vancouver Island—which is on the eastern edge of the Pacific Ocean—makes the reach subject to considerable eastward wind loading. The wind speed changes throughout the day, which creates diurnal variations in surface water velocities in the channel. MMFN noted that wind typically increases throughout the day and peaks in the afternoon. The wind effects are less pronounced downstream of the crest where flow is primarily gravity driven.

3.1.5 Sediment characteristics

The dominant substrate in the reach varies considerably from upstream to downstream, with relatively higher amounts of fines in the deep upstream section and coarser cobbles dominating the downstream shallower section. The bed in the downstream pool is also cobble- and boulder-dominated, similar to substrate found in the shallower sections. A thick layer of algae is present throughout the stream transition, although it is less prevalent in the bars that were exposed during summer low flows. The algae create a smooth surface over the otherwise rough bed, which may potentially decrease the overall skin friction of the reach. A map of the distribution of substrate is shown in Figure 8.

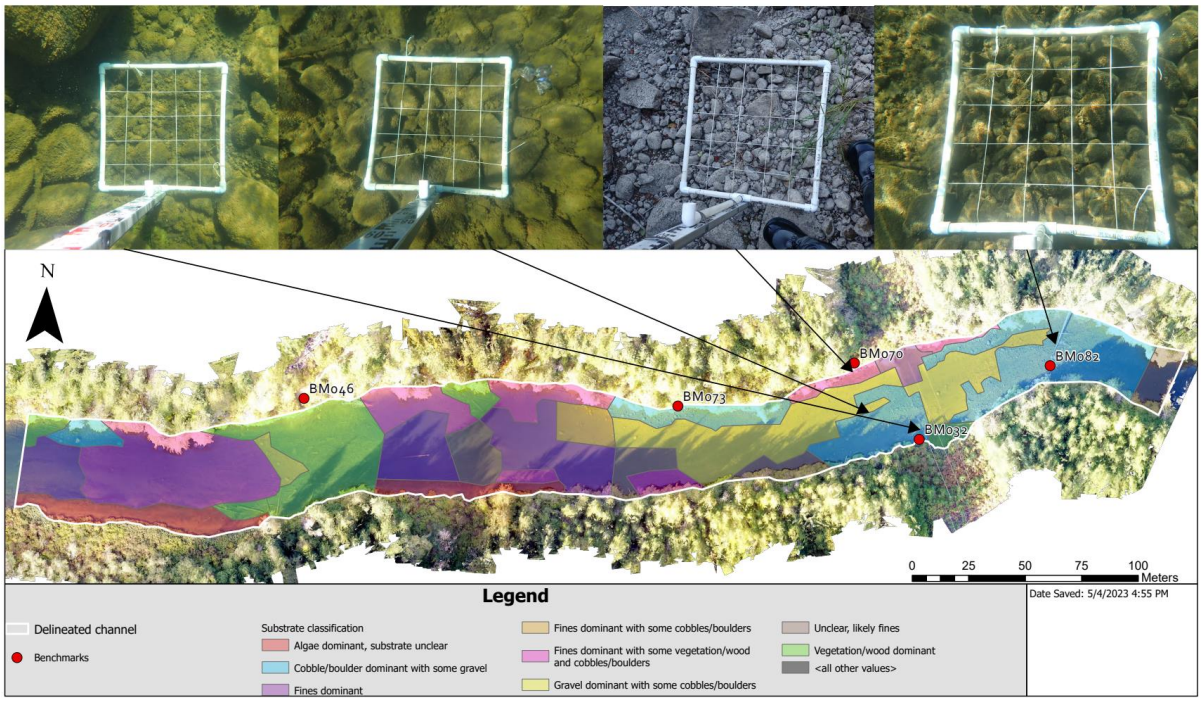


Figure 8 Spatial distribution of substrate in the channel

Large boulders and wood logs are interspersed throughout the entire reach. While some of these features are fully submerged near the thalweg, others are located near the banks or in areas of relatively shallower depths, which creates complex roughness features that can range from partial to full submergence throughout the year. A log jam was present at the river bend along the crest in the first year of the study (2022) that was also visible in previous RPAS imagery from 2021. However, it was washed out by January 2023, indicating that although large wood has an important influence on the hydraulics, such features may be transient at different time scales. These features also show that the river functions as a transport pathway for large wood, which is unsurprising given the historical prevalence of forest harvesting in the upper reaches of the watershed.

3.2 Project timeline

The timeline of the study is presented in the following figure.

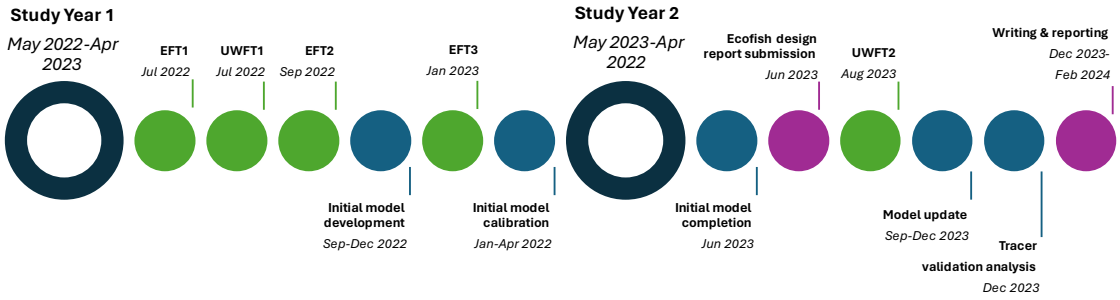


Figure 9 Study timeline, where green represents field trips, blue is modelling and analysis, and purple are items related to reporting.

In Year 1, four field visits were completed to collect data and to seed tracer stones in the study reach. The data was used to develop and calibrate an initial numerical model. A major limitation with this early model was the uncertainty of the reliability of 2D sediment transport predictions derived from hydrodynamic models calibrated with friction zones. A novel shear stress calculation method based on the Saint-Venant momentum equation was proposed to circumvent this limitation, however this method is highly sensitive to bathymetry and still requires additional development.

A field visit was completed at the start of Year 2 in the study to collect additional topographic data and recover the tracer stone positions, which allowed for the validation of the sediment transport model. The topography data was then used to update the model by extending its downstream boundary condition to a water level gauge and changing the calibration strategy. This extension was intended to significantly reduce the uncertainty surrounding the stage-discharge rating curve at the downstream boundary, as the previous curve was interpolated from the rating curves of the two onsite gauges. The location of the new boundary is also preferred since it creates a simpler open boundary than the previous location which was in the middle of a pool where eddies typically form near the banks. The updated model is presented as the final result of this thesis.

3.3 Data collection and preparation

The required data inputs for the numerical model are the channel extents, which are used to build the mesh; topographic and roughness data, which are assigned to mesh nodes; and hydraulic data, which is used to determine the design flow rates and develop stage-discharge rating curves.

3.3.1 Discharge

3.3.1.1 Water level gauges

Two water level gauges were installed at the site during EFT1. The upstream gauge ("Pacfish") is a submerged water level and temperature sensor that transmits 30-minute real-time data every 6-hours to the DFO Pacfish Hydromet Gauging Stations website (DFO, n.d.). The downstream gauge ("Solinst") is a Solinst Levellogger and a Barologger that records hourly water levels and barometric pressure. This gauge requires onsite manual downloads to retrieve data. (West et al., 2023).

3.3.1.2 Discharge data collection

Velocity data at multiple cross-sections were collected during the three Ecofish field trips using an Acoustic Doppler current profiler (ADCP). During EFT1, the ADCP was fitted with a real time kinematics (RTK) global positioning system (GPS) rover to collect independent location measurements. Twenty-six transects and four longitudinal passes were completed with this set-up to allow for interpolation of the bathymetry between adjacent cross-sections. For EFT2, the ADCP was used for two deeper transects and a USGS Pygmy mechanical velocimeter was used for a shallow transect. Fourteen transects were completed for EFT3, but only six transects were georeferenced sufficiently to be used for analysis. One of these transects only covered half of the channel as the ADCP failed midway through the transect. The ADCP data was processed by Ecofish staff using WinRiver II (USGS, 2021) to calculate the average discharge values for each EFT listed in Table 2. Further details are provided in West et al. (2023).

Table 2 Field trip discharges used for numerical model calibration

Field trip	Date collected	Discharge (m^3/s)	Source
EFT1	2022/07/07	10.2	ADCP
EFT2	2022/09/08	1.17	USGS Pygmy
EFT3	2023/01/14	123	ADCP

The derivation of discharge using ADCP can be subject to uncertainty due to site-specific conditions. ADCPs are sensitive to the sediment load, as clear streams with low load can result in insufficient acoustic signal being returned to the unit. Uncertainty may also arise from the blanking distance (defined as the near-surface water depth above the transducer and the near-bed water depth

where there is side-lobe interference) where the ADCP cannot measure velocity (Mueller & Wagner, 2013). The blanking distance limits the accuracy of discharges calculated from this method in shallow channels. For EFT2, most of the data were not usable as the flow was not deep enough to exceed the 1 m blanking distance requirement. Hence the USGS Pygmy was used instead to calculate discharge.

In channels such as the Muchalat Lake outlet where the water is often clear and there can be considerable depth differences throughout the reach due to the outlet's funnel-like shape and steep bed slope, the usefulness and uncertainty associated with ADCP-derived measurements can vary significantly. The low sediment input from the upstream lake results in clear waters that make the reach suitable for novel methods in sediment sizing and bathymetry estimation using RPAS. However, the low turbidity also decreases the accuracy of discharge estimation methods using large-scale particle image velocimetry (LSPIV) or ADCP approaches. The range of uncertainty also varies depending on the time of year, as the stage differences between low and high flows are considerable.

3.3.1.3 Design flow rates

The measured flows were used to calculate design flows for the gravel placement. Given the short record period of the site gauges, the design flows were computed from a synthetic time series at the Pacfish gauge. The synthetic data was obtained by scaling the historical records at the Water Survey of Canada (WSC) gauge at Gold River below Ucona River (08HC001) by the drainage areas of the two gauges. A climate change adjustment (CCA) factor was applied to account for potential future impacts of changing climate conditions. Further details are described in West et al. (2023).

According to MMFN, the spawning season for Chinook and sockeye in the Muchalat River typically occurs from September to October, with peak spawning occurring in late October. Coho and chum tend to spawn later, with their peak occurring in November. Annual variations in flow or temperature can cause these peaks to occur sooner or later than average (West et al., 2023). Thus, simulations of the average October and November flows are expected to represent the peak spawning period for four species, while also representing alternative spawning periods for Chinook and sockeye, which are the species of interest in this study. The design flows are presented in Table 3.

Table 3 Design discharges for model simulation

Flow	Description	CCA	Discharge (m^3/s)
7Q10	Lowest 7-day average with 10-year return period	-20%	0.55
LoFT	Measured flow from EFT2 (USGS Pygmy)	-	1.17
MeFT	Measured flow from EFT1 (ADCP)	-	10.2
CnSp	Chinook & sockeye spawning flow (Oct average)	-	25.9
CoSp	Coho & chum spawning flow (Nov average)	-	42.3
Flush	400% of mean annual discharge	-	87.5
HiFT	Measured flow from EFT3 (ADCP)	-	123
2yr	2-year return flow	+20%	474
10yr	10-year return flow	+20%	759
20yr	20-year return flow	+20%	866
50yr	50-year return flow	+20%	1005
100yr	100-year return flow	+20%	1112
200yr	200-year return flow	+20%	1220

3.3.1.4 Stage-discharge curves

Stage-discharge rating curves at the gauges were prepared by Ecofish by pairing the discharge measurements and gauge WSEs from the EFTs to fit power law relationships given by:

$$Q = 21.417 \times (Z_1 - 194.830)^{1.866} \quad [10]$$

$$Q = 23.436 \times (Z_2 - 194.589)^{2.413} \quad [11]$$

where Q is the discharge (m^3/s), and Z_1 and Z_2 are the corresponding WSEs at the Pacfish and Solinst gauges, respectively. The stages for each design flow at the gauges are in 1430.

3.3.2 Topography

Common methods of obtaining bathymetry data include: 1) interpolation of channel cross-section data collected by ADCP or total station (e.g., Dysarz, 2018), 2) interpolation using LiDAR-based DEMs (e.g., Y. Song et al., 2020), and 3) RPAS-sourced remote sensing to obtain high-density bathymetric estimates (Dietrich, 2017; Harrison et al., 2022; Helm et al., 2020). A combination of all three approaches was adopted for this study.

3.3.2.1 Benchmarks

The system of BMs established by Ecofish were used for this study (shown in Figure 10; full list in 144Appendix A). The BM coordinates were collected using an RTK GPS based on the North American Datum of 1983 (NAD83) Universal Transverse Mercator (UTM) zone 10 coordinate system, the Canadian Geodetic Vertical Datum of 1928 (CGVD28) and the HTv2.0 geoid model.

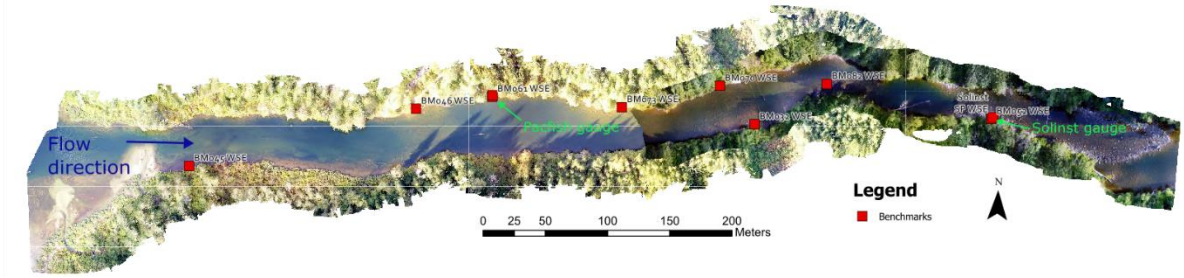


Figure 10 Benchmark locations in the study reach shown in red squares. Flow direction is from left to right, and the two water level gauges are identified with green arrows.

It is noted that the quality of the GPS measurements collected by Ecofish is uncertain due to the proximity of the BMs to canopy and the short GPS occupation durations during the BM survey.

3.3.2.2 Floodplain digital elevation model

A 1 m digital elevation model (DEM) from Western Forest Products (WFP) was provided by Ecofish. The data was collected using Light Detection and Ranging (LiDAR) based on the Canadian Geodetic Vertical Datum of 2013 (CGVD2013) and the Canadian Gravimetric Geoid of 2013 (CGG2013) model. The NRCan vertical datum transformation webtool (NRCan CGS, n.d.-a) was used to convert the data to CGVD28 to align with the GPS measurements.

As the DEM was provided by a third party to the project, knowledge on the date of the LiDAR flight and the water stage on this date was not available. This information is essential for LiDAR over open waters due to its inability of the laser to penetrate water surfaces. Subwater area must be erased from the DEM, which is completed by delineating the contours of the wetted edges. Although the location of the wetted edges can be deduced from an estimate of the WSE, this was not possible due to the lack of information on the date and time of year of the LiDAR collection.

Instead, the subwater points were erased using channel extents that were manually delineated on ArcGIS (Esri, 2022) by referring to RPAS orthoimagery. Overhanging riparian vegetation prevented

a visual identification of parts of the channel edge from the imagery, thus the extents were modified using estimates of the distance to wetted edge for each ADCP transect from EFT1.

3.3.2.3 Solinst gauge total station survey

The elevation across the channel at the Solinst gauge was measured with Leica TS16 total station during WFT2. The locations of two control points (CP) were surveyed with the total station, then tied to the global coordinate system by either resurveying the CPs with >5 hour-long RTK GPS occupations or comparing the points with the project coordinates. A floating coordinate system was adopted relative to the CPs to convert the surveyed points to the project coordinate system using:

$$\begin{bmatrix} \cos\theta & -\sin\theta \\ \sin\theta & \cos\theta \end{bmatrix} \times \begin{bmatrix} X_j \\ Y_j \end{bmatrix} + \begin{bmatrix} X_0' \\ Y_0' \end{bmatrix} = \begin{bmatrix} X_j' \\ Y_j' \end{bmatrix} \quad [12]$$

where θ is the real-world angle between CP1 and CP2, X_j and Y_j are the floating coordinates of the j^{th} point, X_i' and Y_i' are its real-world coordinates, and X_0' and Y_0' are the real-world coordinates of CP1. The errors associated with this transformation are included in Appendix B.

3.3.2.4 Bathymetry estimation from ADCP

Bathymetry measurements were obtained using the data from EFT1 by subtracting ADCP-measured depths from the water surface elevation (WSE) measurements. The streamwise WSE profile during EFT1 was first generalized using a statistical regression of the GPS data from the longitudinal ADCP passes, as shown in Figure 11. A centreline of the reach was drawn from the furthest upstream BM (BM045) to the Solinst gauge and then divided into three sections. The first division was determined based on observed changes in the WSE trends from upstream to downstream. Here, a sudden change in the WSE slope is observed between the upstream section where flow is dominated by lake characteristics, and the transition section where the WSE slopes downwards over a mild adverse bed slope. The second divide was set at a log jam present over the crest during EFT1 and WFT1, which provided a natural break in the collected data and in the WSE profile. The deep scour pool located past this break marked a transition into more typical fluvial characteristics. The increasingly steep WSE slope as flow progresses downstream fits with the shape of an accelerating flow profile in subcritical flow (i.e., an M2 profile according to Chow (2009)).

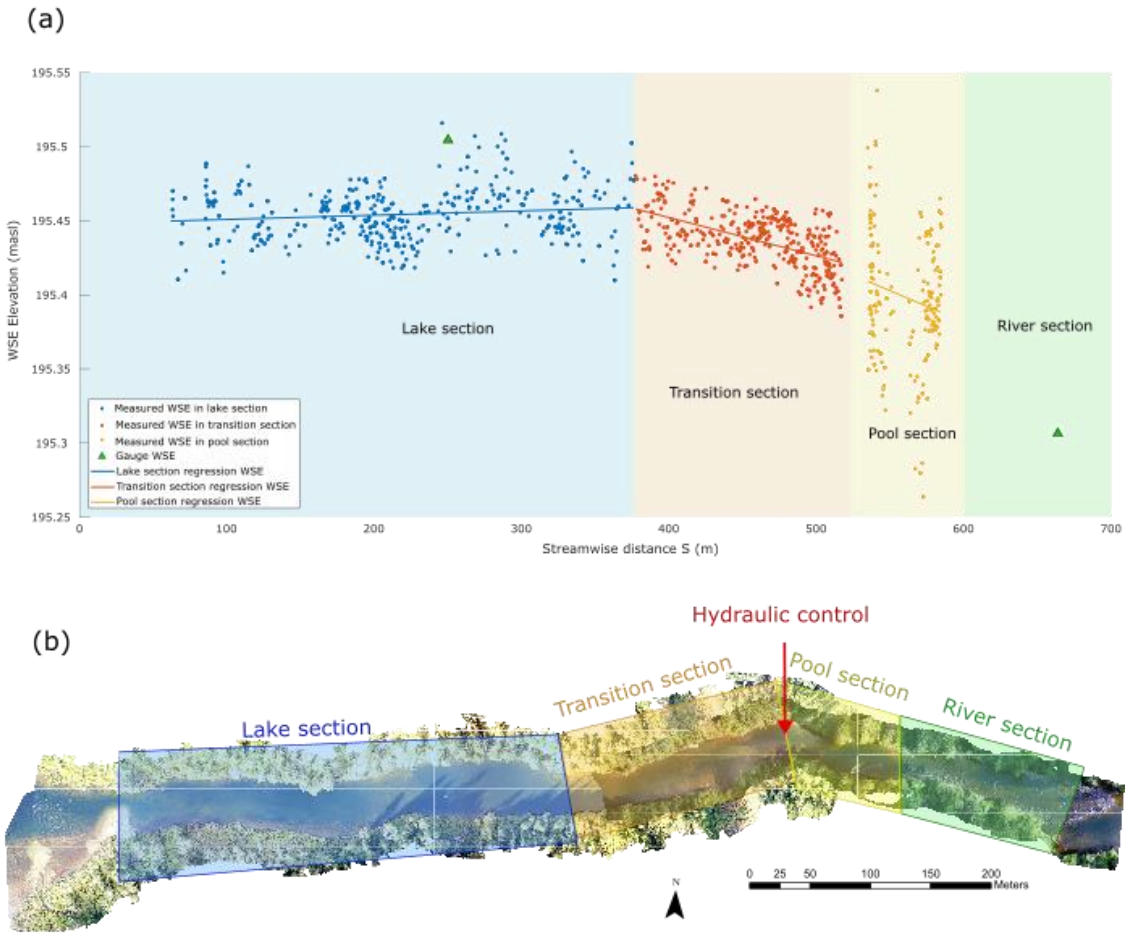


Figure 11 (a) Measured WSE and regression lines along the centreline of each section and (b) the approximate spatial extents of each section.

Considerable variability in the measured elevations of the pool section due to the dense canopy resulted in uncertainty in the accuracy of the regression relationship in this section. The WSE at the Solinst gauge (S ≈ 670 m) is also much lower (~6 cm) than the value predicted by the regression line in the pool section, suggesting that the bed rise at the exit of the pool is causing a drop in the WSE and that the WSE profile cannot be represented as a straight line.

Although not shown in Figure 11, there was also significant variation (≤30 cm) in the measured WSE along transects, likely due to error arising from the influence of canopy near the banks. The WSE was assumed to be laterally non-varying such that the water surface is flat across individual transects. Each of the ADCP points were projected against the stream centreline and the depths were

subtracted from the corresponding value on the WSE profile. The profile of the WSE regression points and the calculated bed elevations from the longitudinal passes is shown in Figure 12.

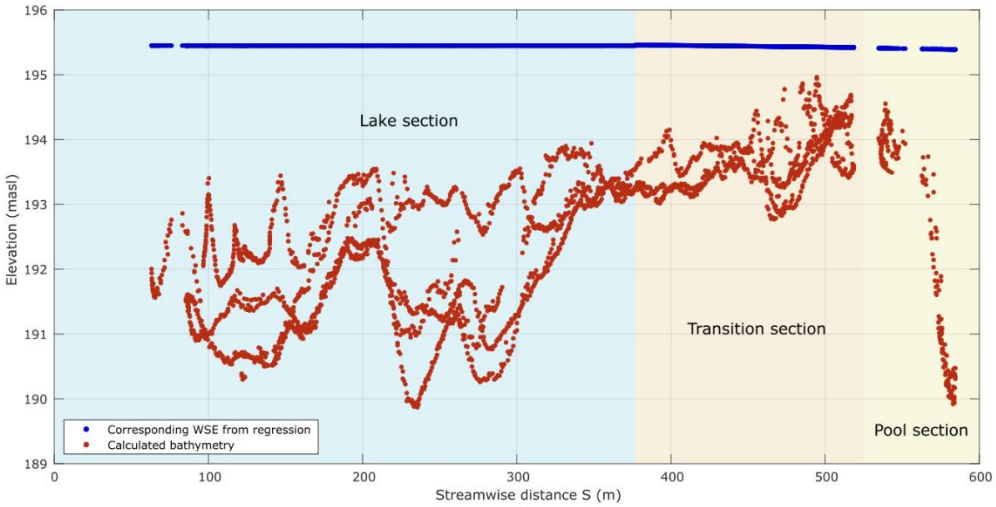


Figure 12 Calculated bed elevation from regression WSE and ADCP depth measurements

3.3.2.5 Remote piloted aircraft system survey

An RPAS survey was completed by Ecofish in 2021 for a watershed study and used to generate an orthoimage of the reach between the lake boundary and the downstream extent of the scour pool. A second RPAS survey was completed during WFT2 for the section between BM070 and BM052 using a DJI Phantom 4. This survey captured imagery of the section downstream of the pool in a second orthoimage and was used to characterize the bathymetry using Structure-from-Motion (SfM) techniques. Twenty-four ground control points (GCPs) were placed underwater throughout the reach prior to the flights, shown in Figure 13. These GCPs were made from cobbles sourced from the reach that were spray painted with orange X's. All GCPs were surveyed with a total station using the methods described in Section 3.3.2.3. The depth of water above each point was recorded for later validation.

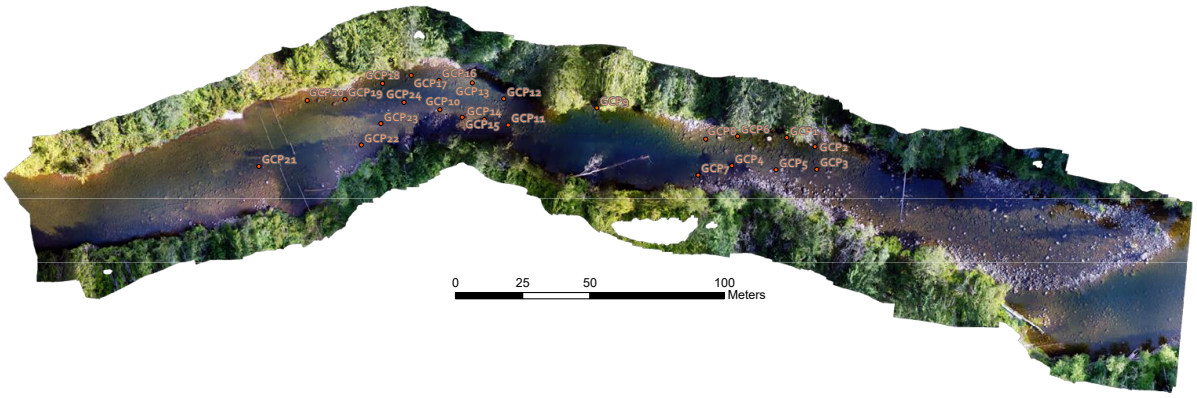


Figure 13 Location of ground control points

Three flights were completed during WFT2 on August 6th, 2023. The RPAS was flown ~40 m above the water surface. The flights were completed at different times of the day to capture different lighting and wind conditions, which is essential for maximizing the area of the reach captured through the images. The camera was set to take a photo every 2 seconds, yielding 798 photos over the three flights. Passes were either completed with the camera set nadir (i.e., facing down at 0º) or obliquely near the banks. The flights are summarized in Table 4 while Appendix B provides additional details.

Table 4 Summary of completed RPAS flights

Flight	Photos taken	Flight speed (m/s)	Flight time	Notes
1	371	0.5-2.5	8:00-8:20 am	Nadir camera angle.
2	308	1.0-2.2	10:10-10:30 am	One pass nadir and two oblique passes of each bank (20-30º). The final pass was flown at 2.2-3.5 m/s due to decreasing battery levels.
3	116	0.8-2.8	2:05-2:15 pm	Two oblique passes (15-20º). Flight cut short due to safety hazard.

3.3.2.6 RPAS photogrammetry

For most RPAS-based photogrammetry applications in fluvial geomorphology, the GCPs are typically placed above water on dry bars due to the distortionary effects of refraction on objects below the water surface. Objects on land are therefore correctly georeferenced, while the coordinates of underwater objects are subject to distortion. Refraction refers to the deviation of the path of light

through the interface of two different media such as air and water, causing these objects in the receiving media to appear at a shallower depth than their actual locations. While this effect has historically limited the application of Structure-from-Motion (SfM) to fluvial uses, recent developments in code such as have allowed for the large-scale correction of these apparent depths (Dietrich, 2017). For this study, the lack of unobstructed dry bars throughout the full reach precluded the application of this technique, as the GCPs could not be evenly spaced out. All the GCPs were therefore placed underwater and inputted directly into the SfM model, with varying levels of depth to reduce the skewing of the model towards specific depths. Six GCP points were also removed from the reference system to avoid overfitting the model and to provide validation points.

The workflow described in Helm (2019) was used to process the data, however, the steps using the refraction adjustment code by Dietrich (2017) was omitted due to the unique GCP placement in this study. This method makes use of a cloth simulation filter (CSF) (W. Zhang et al., 2016) that was shown by Helm (2019) to be effective for removing overhanging vegetation from the SfM model. An additional step of re-aligning the model to all GCPs was added at the end to reduce the systematic error arising from the water refraction. Error in the model is defined here as the difference between modeled elevations from field measurements at the GCPs. The root-mean-square and the mean absolute value of the errors from the reference, validation and combined GCPs is reported in Table 5. Further detail on the processes used to prepare this data are included in Appendix B.

Table 5 Projection error summary statistics

GCP	Original Agisoft error (m)	Post-CSF error (m)	Post-alignment error (m)
Referenced			
RMS	0.064	0.055	0.052
MAV	0.085	0.066	0.063
Validation			
RMS	0.084	0.081	0.021
MAV	0.095	0.093	0.023
Combined			
RMS	0.058	0.046	0.015
MAV	0.082	0.055	0.018

A final validation was completed using the elevations of the Solinst gauge transect. Figure 14 shows that the model can capture average elevation changes, but systematically produces slightly higher elevations in deeper submerged areas. However, given the lack of better data and the relative insensitivity of 2D hydraulic models to bathymetry, the SfM data is expected to be adequate. The final dense cloud was re-imported into Agisoft to generate the final DEM and orthomosaic image.

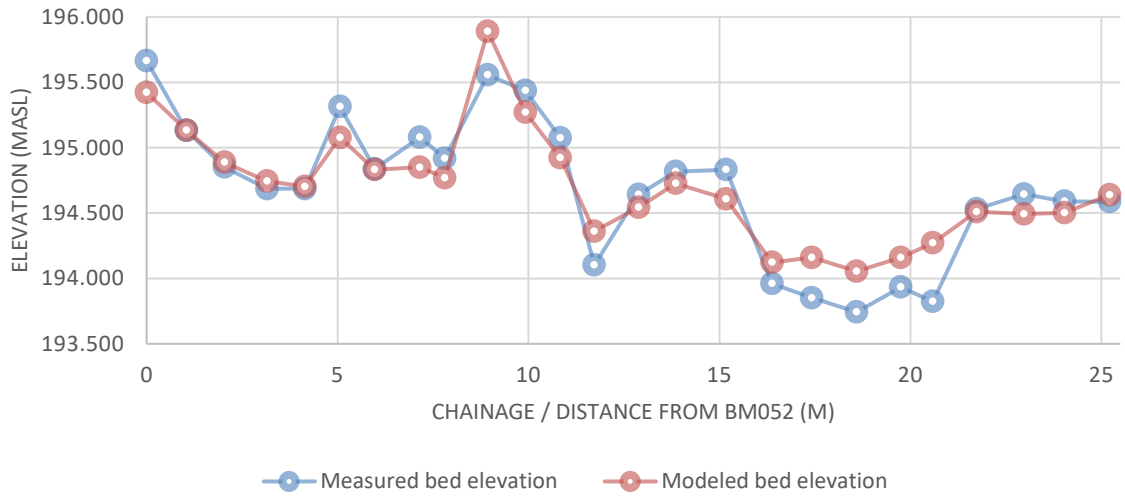


Figure 14 Comparison of measured and SfM bed elevations across the Solinst gauge transect

3.3.2.7 Blue Kenue

The topography was interpolated and mapped onto the mesh using Blue Kenue. Blue Kenue is a software tool developed by Canadian Hydraulics Centre (CHC) at the National Research Council Canada (NRC) for the preparation, analysis, and visualization of data for hydraulic models. The software supports the file formats required by the hydraulic model, and provides functionalities including mesh generation, data mapping and boundary condition delineation.

The topographic mesh used in this study consists of a dataset described in the previous sections. The initial model employed only the floodplain DEM and the ADCP cross-sections, as the RPAS data had not yet been collected, while the final numerical model used all three sources. Artificial water surface points at the edge of the channel were added based on the linear regression WSE profiles shown in Figure 11. This step prevented channel narrowing as an artefact of topographic interpolation, which can occur in areas without cross section data as part of the conversion from a sparse set of bathymetry measurements to a 2D grid.

3.3.3 Roughness

3.3.3.1 Nikuradse roughness length

The logarithmic velocity profile for hydraulically rough flow is described by Equation [1].Nikuradse (1930) showed that for a logarithmic velocity profile on a fully rough bed, the reference height, z_0, is related to the hydraulic roughness of the bed and to the equivalent sand-grain roughness, k_N (m), as:

$$z_0 = \frac{k_N}{33} \quad [13]$$

In TELEMAC-2D, the Nikuradse roughness is converted to the Chézy roughness C ($m^{1/2}/s$)via Equation [14] and then to the skin friction coefficient C_f using Equation [15] (Hervouet, 2007).

$$C = 7.83 \ln\left(12\frac{h}{k_N}\right) \quad [14]$$

$$C_f = \frac{2g}{C^2} \quad [15]$$

López & Barragán (2008) compiled empirical data from past studies and proposed that the Nikuradse roughness is related to 84th percentile grain size fraction, D_{84} (m):

$$k_N = 2.8D_{84} \quad [16]$$

The Nikuradse equivalent roughness length k_N was used as to define roughness in the channel. Modelling k_N as a function of the bed particle size is advantageous because it allows the modelled roughness of the channel to decrease with increasing stage, which matches what is expected from measured results in gravel bed rivers. Manning's n, by contrast, is a fixed value and so should theoretically be calibrated for each water level (Ferguson, 2010).

3.3.3.2 Substrate photos

Thirty-eight substrate photos were taken by Ecofish during FT1 across three transects located at BM070, BM032 and BM082. A square 50x50 cm grid with 10-cm squares, shown in Figure 15, was included as a scaling object in the photos. The images were mostly taken with the grid and the substrate fully submerged underwater while the camera was held above the water, which resulted in significant refraction and reflection on the water surface.

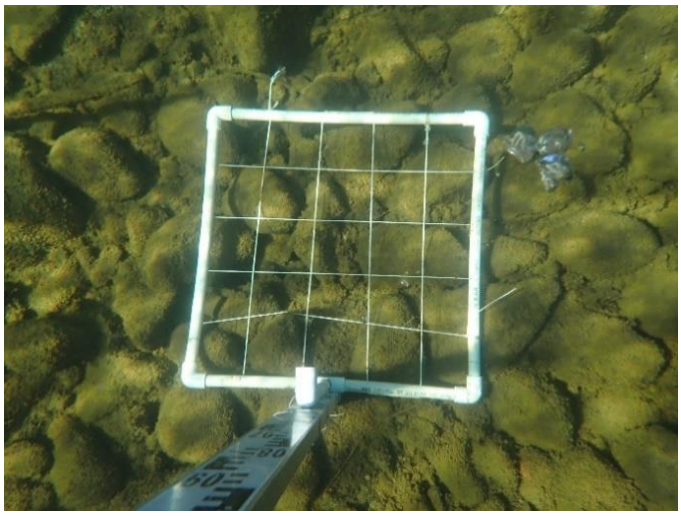


Figure 15 Example of the substrate photos taken by Ecofish.

3.3.3.3 Photographic pebble count

Various image analysis techniques have been proposed compute grain size distribution (GSD) from images of sediment. These techniques may use image segmentation techniques, statistical methods, or interpretations of the spectra of image intensity (Cuttler et al., 2017). Open-source code (e.g., Buscombe, 2013, 2020; Purinton & Bookhagen, 2019) have been developed to streamline the implementation of these techniques, but these methods are generally developed for photos where sediment grains are clearly resolved, and where neither the camera and substrate are not submerged.

It was determined that these methods would not be applicable to this project given that the substrate photos had: (1) water reflection and refraction that distorted the underwater objects; (2) inconsistent photo quality, with variable degrees of reflection, refraction, algae and suspended solids which would require photo-by-photo calibration; and, (3) an obtrusive scaling object that was difficult to remove through masking. Instead, a visual pebble count was manually completed by sampling the particles that intersected with the interior crosshairs of the grid. Up to sixteen particles were sampled for each photo where the sediment sizes were clearly resolved by eye, resulting in a potential of 608 grains for the 38 substrate photos. This number was reduced to 170 particles due to the poor quality of some images and the coarseness of the grains, which at times overlapped with multiple crosshairs. The GSD curves for each BM transect and the overall set of photos is shown in Figure 16. The overall D_{84} value was 14 cm, which translates to a Nikuradse roughness length of 0.40 m using Equation [16].

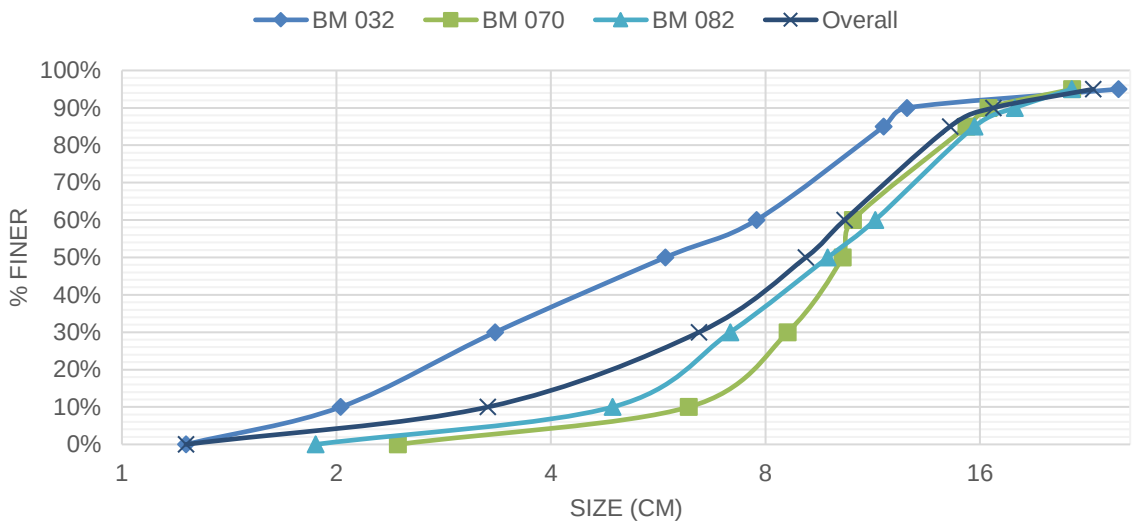


Figure 16 Grain size distribution at three transects near BMs.

3.3.4 Radio frequency identification tracer stones

3.3.4.1 Tracer stone preparation

The tracer stones were drilled stones that were fitted with radio frequency identification (RFID) passive integrated transponder (PIT) tags. The stones were locally sourced from Oktwanch River and Gold River ~14 km downstream of its confluence with Muchalat River. Holes approximately 23-50 mm deep were drilled into the stones using a slotted drive system (SDS) hammer drill with a 3/16-in drill bit. The fine dust in the holes was cleaned out with a straw cleaner and water in a spray bottle. Each stone was fitted with a 23 mm half duplex (HDX) PIT tag and sealed with masonry caulking. A typical cross-section of the RFID-fitted stones is shown in Figure 17.



Figure 17 Tracer stone cross-section with a 23 mm RFID PIT tag.

A recommended gradation curve for Chinook spawning substrate was provided by Ecofish and shown in Figure 18. The GSD was used to define the three size classes listed in Table 6. RFID tags were assigned so that stones in the same class would have tag numbers within a prescribed range.

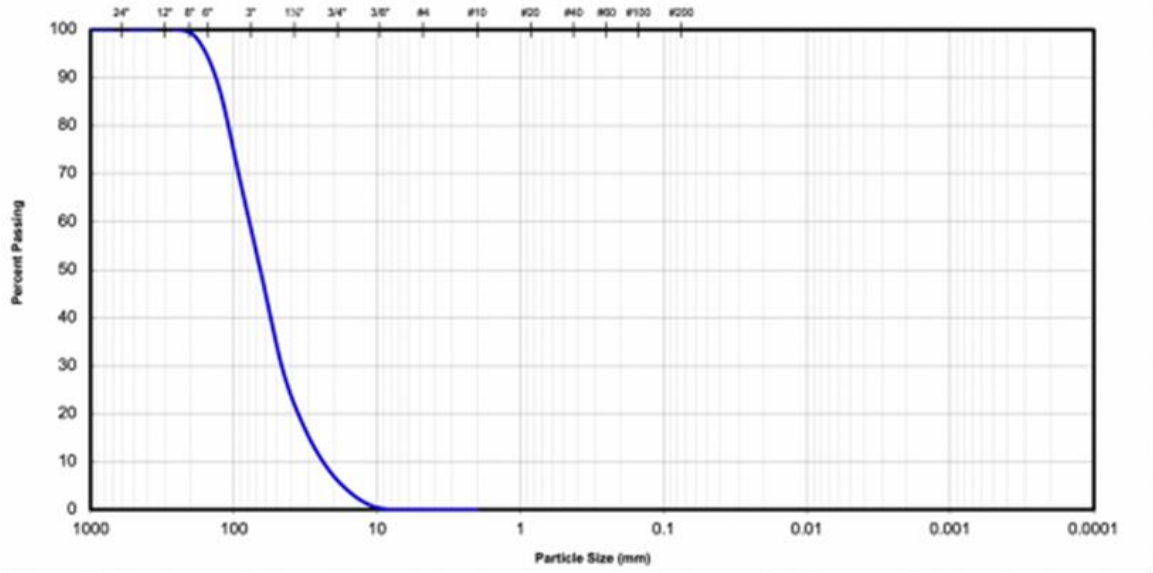


Figure 18 Recommended GSD curve for Chinook salmon spawning gravel from Ecofish.

Table 6 Tracer stone size class characteristics, obtained from the spawning substrate GSD

Category	GSD class	Range (mm)	Median (mm)	Range (ϕ)	Quantity prepared	Tag No. Range	Quantity placed
Small	D50	45-64	54.5	5.5-6	80	400-479	70
Medium	D60	64-90	77	6-6.5	64	480-543	56
Large	D90	90-128	109	6.5-7	48	550-597	42

The stones were striped with permanent marker to make them visually differentiable in the field. The small and large categories were marked with black while the mid-sized stones were marked with red. An image of the tracer stones after the completed process is shown in Figure 19.

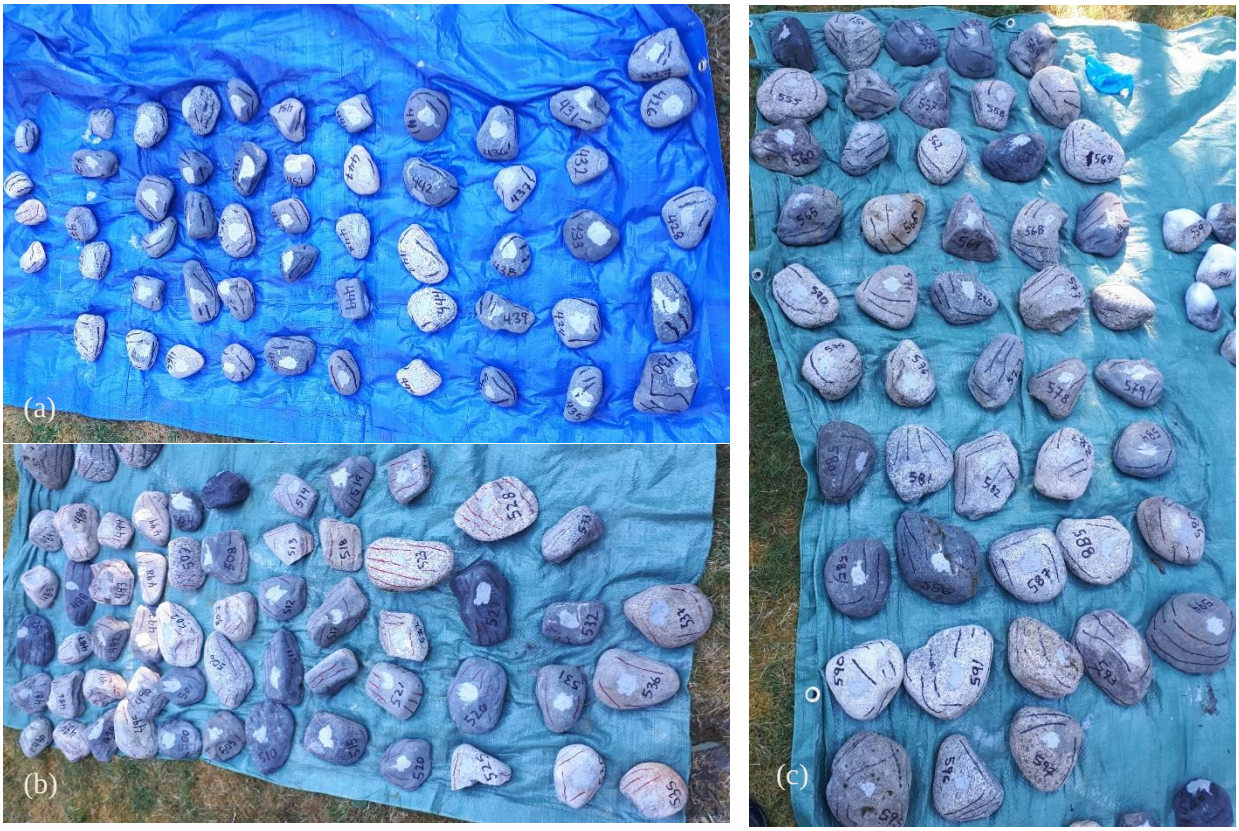


Figure 19 Small (a), medium (b) and large (c) tracer stones after preparation.

The A-, B- and C-axis diameters (d_A, d_B, d_C) and the masses of each particle were recorded and used to characterize the shapes of the particles following the classification scheme from Zingg (1935).

Rounded granitic type stones were found to be less prone to breakage during drilling than the angular volcanic stones, thus the particles in the small size class were primarily granitic spheroids (Figure 20). Some studies have reported selective shape entrainment in low to moderate flood events (Cassel et al., 2021; Demir & Walsh, 2005; Schmidt & Ergenzinger, 1992) which may open the possibility of skewed mobility data, given the preferential selection of the tracer stone shapes.

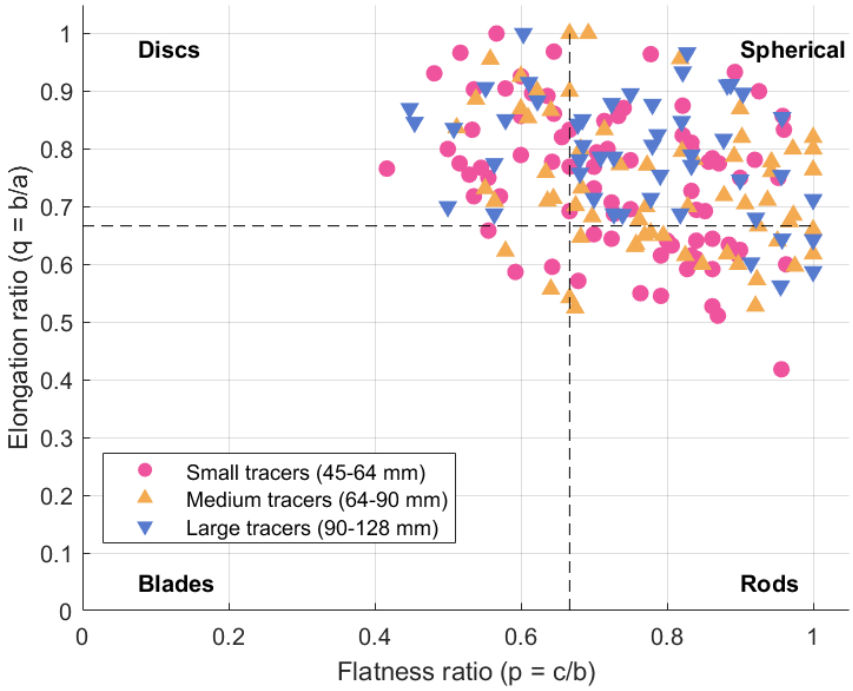


Figure 20 Tracer stones shape classifications based on Zingg (1935) categories.

Given the strong clustering of stones in the spherical category, it was assumed that the volume of the tracer stones could be represented by the volume of an ellipsoid shape using:

$$\forall = \frac{4}{3}\pi r_A r_B r_C = \frac{d_A d_B d_C}{6}\pi \qquad [17]$$

where $\forall$ is the particle volume (m^3), and r_A, r_B and r_C are the radii (m) of the A-, B- and C-axis, respectively. Using the calculated volumes and measured masses, the densities of each clast were obtained, which ranged from 2123-5966 m^3/s with an average value of 3429 m^3/s.

3.3.4.2 Placement strategy

The target area for the tracer stones was delineated based on the area identified by Ecofish at the time of seeding to be the most likely target for the gravel placement. A total of 168 stones were distributed across 7 transects, with each consisting of 24 stones (10 small, 8 medium and 6 large). A placement pattern allows for some lateral randomization while retaining consistency between each transect. The pattern is listed in Table 7, starting with 1 at the right bank (looking downstream).

Table 7 Tracer placement pattern across the transects

No.	**1**	**2**	**3**	**4**	**5**	**6**	**7**	**8**	**9**	**10**	**11**	**12**
Size[1]	S	M	L	S	S	M	L	S	M	S	L	M
No.	**13**	**14**	**15**	**16**	**17**	**18**	**19**	**20**	**21**	**22**	**23**	**24**
Size[1]	S	M	L	S	M	S	L	M	S	S	L	M

[1]S – small; M – medium; L - large

During the visit, the Geode GPS supplied by Ecofish did not work due to technical errors, which prevent the record of the exact locations of the stones. The approximate lateral position of each stone was instead measured using a transect tape. The error associated with the lateral position of each placed stone varied depending on the conditions at that cross-section. Stones at deeper cross-sections located further upstream were dropped from the boat or from swimming, thus greater errors are expected than the shallower transects where placement could largely be completed by wading. The error in the deeper cross-sections may be up to 1 m, while the margins of error at the shallower cross-sections are expected to be sub-metre. The locations of the transects were not recorded during WFT1 due to time constraints but were tied into the tracer locations during WFT2.

3.3.4.3 RFID antennae

The search for the tracers was completed using a portable RFID reader (LF HDX Backpack Reader). The search range of the reader was extended using antennas. The reader is powered by a 12 V battery and includes three ports that attach to a buzzer, a serial-to-Bluetooth adapter, and an antenna, as shown in Figure 21. Upon detection of a tag, the buzzer sounds, and the tag number is sent to an external device via the Bluetooth adapter (Grid Connect Firefly Bluetooth adapter).

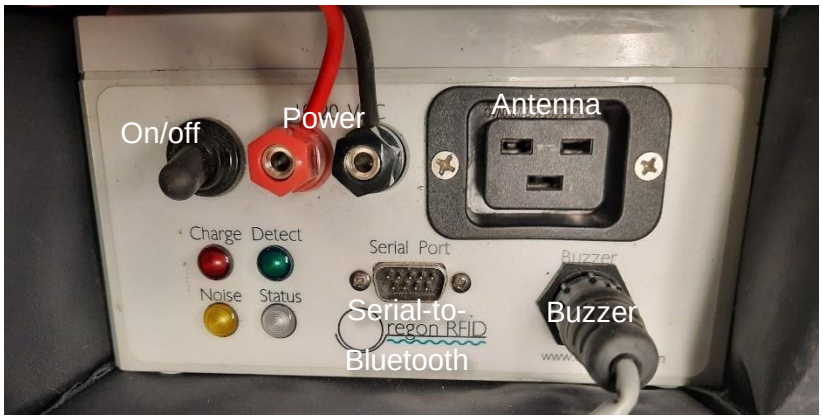


Figure 21 Top view of the LF HDX Backpack reader.

A pre-built pole antenna was used in the wadable sections of the reach, while a custom-built flexible loop RFID antenna was used in the deeper areas. The pole antenna is housed in a 0.25 m radius loop attached to a rigid 2 m polyvinyl chloride (PVC) pole and has a 0.5 m detection radius The tuner housed in the upper section of the pole is an open circuitry board and the antenna housing is not waterproof, thus limiting the use of the pole from use in deep water.

The second custom antenna was built to address the unique needs of the site, as flexible maneuvering was required for searches completed through swimming. The design consisted of five components: a coaxial cable forming the antenna wiring, a tuning capacitor box, twin axial cable running between the tuner and the reader, and an AC power supply connector that connects to the tuner. The tuning capacitor used in the prototype (Texas Instruments RI-ACC-008B-30 or the Orgon RFID pre-2015 standard tuner) has watertight cable grips and a gasket sealing the gap between the transparent cover and the main body.

A Belden 34412 coaxial wire rated at 12 American wire gauge (AWG) with 65 × 30 stranding was used for the antenna. It was predicted that the maximum depth at which the antenna needed to be used was 2.5 m based on continuous gauge records at the Pacfish gauge in early July 2023. Accordingly, a wire length of 4-5 m between the loop and the tuner was assumed to be necessary to provide sufficient depth and slack between a swimmer holding the loop and a boat containing the electronics.

The size and number of loops and the length of antenna wire governs the inductance generated by the antenna, which was tested by attaching the antenna wire in series with an inductance meter measuring at a frequency of 1 kHz. The size and number of loops were varied until an inductance

reading in the middle of the tuner's allowable range (8-80 µH) was achieved. A 60 cm diameter loop with 6 passes and a 4.2 m wire length to the capacitor was found to yield an inductance of 57 µH. The loops were passed through a ¾-in flexible PVC conduit fashioned in a circular shape and out through a T-shaped conduit body. The remaining 4.2 m wire was twisted to reduce noise and passed through a ½-in vinyl tube before being attached to the tuner. The tube was not directly sealed to the conduit body to allow water to fill the housing and reduce its buoyancy, thereby improving its maneuverability underwater. An unshielded Belden 22 AWG twin axial cable was attached to the tuner box and the other end was fitted with a male AC power plug (Schurter 4789.1200) that connects directly with the reader. Once assembled, the antenna was tuned approximately using the jumper chart associated with the tuning capacitor and then fine-tuned using a ceramic screw and a tuning indicator. The antennas are pictured in Figure 22



Figure 22 (a) The pre-built loop pole antenna from Oregon RFID and (b) the custom-built flexible antenna.

3.3.4.4 Recovery strategy

The recovery procedure consisted of passing over each of the seven cross-sections with an antenna to locate the tracers placed along the transect. When a tracer was found, its location was surveyed immediately using a total station. The three transects located furthest downstream were first scanned using the pole antenna as the water depth was mostly under waist height. The search at these cross-sections were then repeated using the flexible antenna, as the recovery rate over the three transects via

wading was only around 75%. The search procedure using the flexible antenna consisted of one diver holding the antenna, a coordinator on a canoe holding the reader, tuner, total station prism and clipboard, a canoe paddler, and a total station operator.

3.4 Hydrodynamic model

A 2D steady flow hydrodynamic model was developed to simulate the site hydraulics using TELEMAC-2D. An initial model was created in the first study year using solely the site data collected by Ecofish during their three field trips. The model was used to generate sediment transport predictions based on the Wilcock & Crowe (2003) equations, map habitat suitability using habitat suitability index (HSI) curves and capture sand flushing potential. These preliminary results were used to support a client report submitted by Ecofish in July 2023. Details on the development and calibration of the initial model are included in Appendix C. Validation of the model were completed following UWFT2 using tracer stone results. The model boundary and roughness conditions were updated using these findings to improve the confidence in the prediction accuracy.

3.4.1 TELEMAC-2D

TELEMAC-2D is a solver in the open-source TELEMAC-MASCARET software system (Hervouet, 1999, 2007). TELEMAC-2D solves the two-dimensional non-conservative Navier-Stokes equations (Hervouet, 1991, 1994), which are also commonly referred to as the shallow-water equations (SWE). The SWE are derived by depth-averaging the Navier Stokes equations to obtain the following mass continuity and momentum conservation formulas Hervouet (2007).

$$\frac{\partial h'}{\partial t} + \frac{\partial}{\partial x}\big((H + h')u\big) + \frac{\partial}{\partial y}\big((H + h')v\big) = 0 \quad [18]$$

$$\frac{\partial u}{\partial t} + u\frac{\partial u}{\partial x} + v\frac{\partial u}{\partial y} = -g\frac{\partial h'}{\partial x} - ku + \nu\left(\frac{\partial^2 u}{\partial x^2} + \frac{\partial^2 u}{\partial y^2}\right) \quad [19]$$

$$\frac{\partial v}{\partial t} + u\frac{\partial v}{\partial x} + v\frac{\partial v}{\partial y} = -g\frac{\partial h'}{\partial y} - kv + \nu\left(\frac{\partial^2 v}{\partial x^2} + \frac{\partial^2 v}{\partial y^2}\right) \quad [20]$$

where t is time (s), x and y are horizontal coordinates on a Cartesian plane (m), H is the mean water depth (m) at a node, and h' is the deviation from the mean depth (m) such that $h(x, y, t) = H(x, y) + h'(x, y, t)$, u and v are the x- and y-components of velocity (m/s), g is the acceleration due to gravity (m/s), k is the viscous drag coefficient (1/s), and ν is the kinematic viscosity of water (m^2/s).

3.4.2 Model set-up

A triangular mesh was generated using Blue Kenue. Iterations with various cell sizes and time steps were tested until the model could reliably achieve convergence with a Courant number consistently below 1. The Courant number, C_n, describes the numerical stability of the model as a ratio of actual wave velocity to numerical wave velocity and is given:

$$C_n = \frac{|u \pm c|}{\Delta x / \Delta t} \leq 1 \quad [21]$$

where c is the wave celerity (m/s), Δx is the length of the mesh element (m), and Δt is the time step duration (s) (Sturm, 2010).

The mesh of the final updated model consisted of 37672 nodes and 74749 elements, with an average 1 m side length for in-channel elements and a 3 m side length for the floodplain elements. An element edge growth factor of 1.2 was applied in Blue Kenue's mesh generator to connect the channel sub-mesh with the floodplain mesh.

The convergence criteria were set based on permissible variable thresholds for velocity and depth, where the computation stops if the absolute difference between two successive time steps at all nodes is less than the threshold. If the criteria are not met, the computation will continue until the user-defined duration. A duration of 30,000 seconds was generally sufficient to reach a volumetric steady state within at least 3 decimal places. The time step length was set at 0.2 seconds for all scenarios.

3.4.3 Model boundary conditions

Liquid (or open) boundaries were set roughly 10 m past the bankfull channel at the upstream and downstream channel extents, while no-flux (closed) boundaries were defined for the remainder of the model extents. The upstream boundary condition consisted of a prescribed flow rate and variable depth, while the downstream condition had a prescribed elevation and variable flow rate. The prescribed flow rates corresponded to the discharge values presented in Section 3.3.1.3.

The downstream boundary conditions for the initial model were interpolated from the rating curves from the two onsite gauges. Details on the methods and assumptions used to estimate these values are included in Appendix C. Comparatively, the downstream boundary of the updated model was set at the Solinst gauge, thus the gauge rating curve was directly applied to calculate the corresponding stages. The values prescribed for the boundaries at each flow are summarized in Table 8.

Table 8 Boundary conditions for the initial and updated models

Flow scenario	Upstream boundary flow rate (m^3/s)	Initial model downstream boundary stage (masl)	Updated model downstream boundary stage (masl)
7Q10	0.55	194.80	194.80
LoFT	1.17	194.89	194.88
MeFT	10.2	195.34	195.30
CnSp	25.9	195.74	195.63
CoSp	42.3	196.03	195.87
Flush	87.5	196.62	196.32
HiFT	123	196.98	196.58
2yr	474	199.11	196.72
10yr	759	200.17	198.07
20yr	866	200.50	198.81
50yr	1005	200.88	199.05
100yr	1112	201.15	199.34
200yr	1220	201.40	199.54

3.4.4 Turbulence model

The turbulence closure model selected for use was the Rastogi & Rodi (1978) adaptation of the k-ε equations for the Saint Venant equations (Hervouet, 2007). The k-ε turbulence model requires minimal user-defined parameters in 2D models and thus relatively little calibration compared to other turbulence models. This model is also computationally inexpensive and able to provide reasonably accurate predictions (Almeida & Ota, 2020), making it suitable for most engineering applications.

3.4.5 Calibration

The model was calibrated by comparing the depth-averaged velocity of the HiFT flow scenario at the six ADCP transects measured during EFT3. The measured and modeled vectors and magnitudes were plotted for each transect, from which the coefficient of determination R^2, Nash-Sutcliffe efficiency (NSE) coefficient, root-mean-square error (RMSE) and percent bias were calculated.

Each performance metric captures different aspects of error in the model. The R^2 value represents the correlation between modeled and measured values (i.e., how well the shape of the cross-sectional velocity profile is predicted by the model) where 0 implies no correlation and 1 implies a perfect correlation. The R^2 is limited in its inability to capture systematic error or situations where the cross-sectional velocity profile is relatively flat, as such cases would appear to have no discernible trend. The NSE is a similar parameter that compares the fit between observed and simulated data and is better equipped to capture systematic errors but tends to overestimate performance with model runs containing higher values and underestimate performance with low values. NSE ranges from $-\infty$ to 1, where NSE = 1 is a perfect fit and NSE < 0 indicates that the mean value would have been a better predictor than the model. In the context of these 2D hydrodynamic models, a zero NSE value can be interpreted such that equivalent results could have been obtained from a 1D model. RMSE shows an absolute value of error and is context dependent. It can therefore be used to compare apparent model performance at a range of flows and stages. Percent bias is useful for identifying systematic errors in the prediction, which are not captured by the other performance metrics.

Roughness was varied to calibrate the hydraulic model, as it is the only independent variable in the depth-averaged k-ε turbulence model formulation. The calibration methods for the initial and updated models differed and are thus detailed in the following subsections separately. The finalized calibration was validated with the MeFT flow scenario.

3.4.5.1 Initial model calibration

The initial model was calibrated by assigning spatial friction zones to the mesh through a Fortran subroutine. These friction zones were used to account for roughness resulting from: 1) the transitional deposition of increasingly coarser bed material from upstream to downstream, 2) bank effects at high flows resulting from overhanging tree branches, and 3) the relative presence of algae between upstream and downstream sections. A summary of the in-channel zones is presented in Table 9.

Table 9 Nikuradse roughness values in each channel friction zone

Friction ID	Roughness k_N (m)	Description
100	0.396	Default roughness value calculated from substrate photos.
200	1.00/5.00	Accounts for overhanging vegetation for high flows and rougher banks (1.00 for low flow, 5.00 for high flow).
300 to 600	0.300 to 0.100	Transition zones between downstream and upstream sections.
700	0.750	Cobble/boulder deposits near upstream left bank.
800	0.04	Smaller substrate sizes between middle and edge in upstream.
900	0.004	Smaller substrate sizes in upstream thalweg.

The Baptist et al. (2007) vegetation model was applied to the floodplain to replicate the slower velocities through forested areas under flood conditions without increasing the roughness values. The vegetation model was used to minimize artificially high shear stresses in the floodplain area, as De Jong (2005) had shown that increasing the Nikuradse roughness length to account for vegetation resulted in higher shear stresses than the Baptist model. The Baptist vegetation model implemented through TELEMAC-2D requires three parameters: 1) the friction factor for the floodplain soil, the drag coefficient C_d (~1.0 for rigid cylinders), 2) the product of vegetation density m (1/m^2) and the average diameter of the cylinders D_v (m), and 3) the average height of the vegetation h_p (m). Finnigan (2000) found that the second input, mD_v, can be approximated through the leaf area index (LAI) and vegetation height h_p through:

$$mD_v = 0.5 \times \frac{LAI}{h_p} \quad [22]$$

The forest in the study area was assumed to be of similar density and species as forests near Victoria, BC where Chen et al. (2002) characterized the LAI to be 7.1-10.3. The upper value of this range was adopted as the site is more rural than Victoria and was thus expected to have a higher LAI.

A roughness length of 0.004 m was used for the floodplain area to align with the smoothest zone of the channel, since it was expected that the soil consists largely of fines, and organics. This value was varied from 0.004 to 0.4 in a sensitivity test and was found to have negligible impact on the results.

The average vegetation heights were determined using a canopy height model provided by Ecofish from WFP, with the canopy heights subdivided into three classes for the manual delineation of three friction zones in the floodplain. A summary of the vegetation model parameters for each zone is presented in Table 10, while the combination of friction and vegetation zones are shown in Figure 23.

Table 10 Baptist (2007) vegetation model parameters for each class

Friction ID	Canopy heights (m)	Median height h_p (m)	Vegetation characteristic density mD (m^{-1})
1000	0.001-9.1	4.5	1.03
1100	9.1-22.4	15.7	0.328
1200	22.4-46.4	34.4	0.150

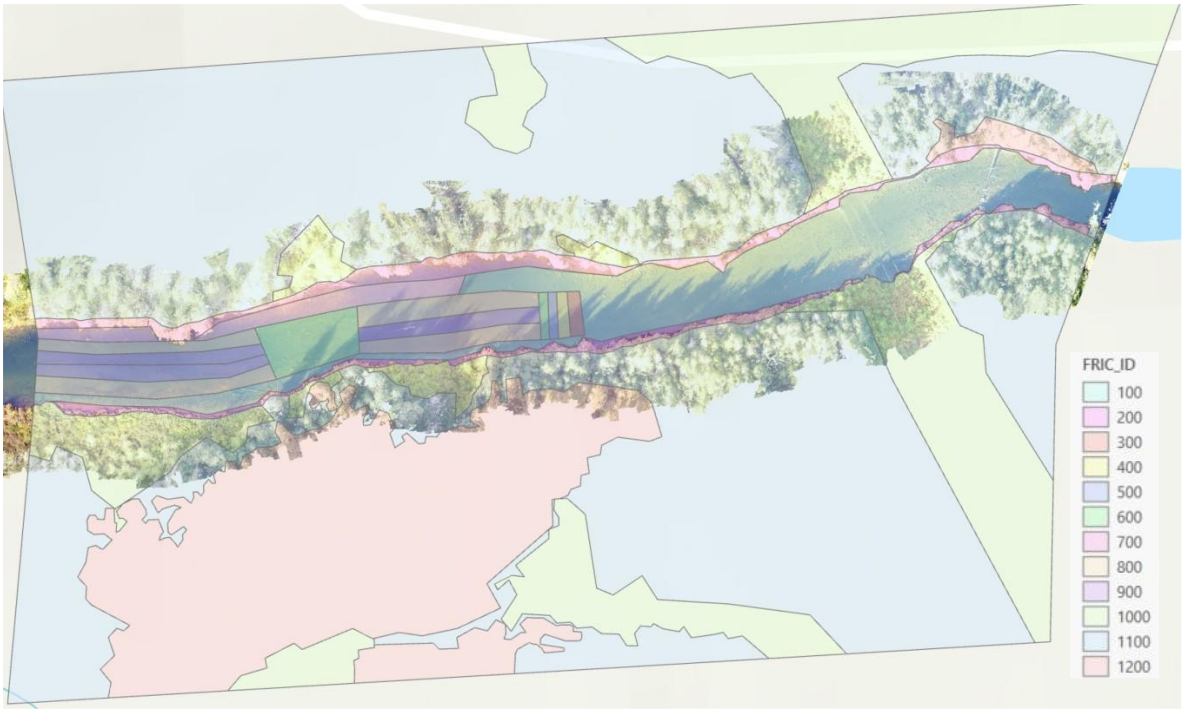


Figure 23 Roughness zones and corresponding IDs in initial model.

The calibration improved the average R^2 and RMSE of the transects in the model from 0.77 and 0.183 m/s to 0.80 and 0.157 m/s, respectively for the flow scenario HiFT (Table 3). Validation using the LoFT and MeFT scenario discharges yielded comparatively low average R^2 values, which were

0.04 and 0.35, respectively. The low agreement was attributed to the limitations of the ADCP at low discharges which likely result in inaccurate velocity measurements, the increased sensitivity of the model to bathymetry at low depth and the poor ability of most hydraulic equations to capture high relative roughness conditions. The low magnitude of velocities at the LoFT and MeFT also likely magnify the apparent error, as the average RMSE for these scenarios, 0.184 and 0.082 m/s, are similar to that of the HiFT flow. Further detail on the initial model is in Appendix C.

3.4.5.2 Updated model calibration

The updated model did not employ in-channel friction zones to avoid issues arising from the sensitivity of the shear stress calculations to prescribed friction. Instead, a constant reach-averaged roughness value was applied, with only the vegetation zones retained in the model (Figure 24).

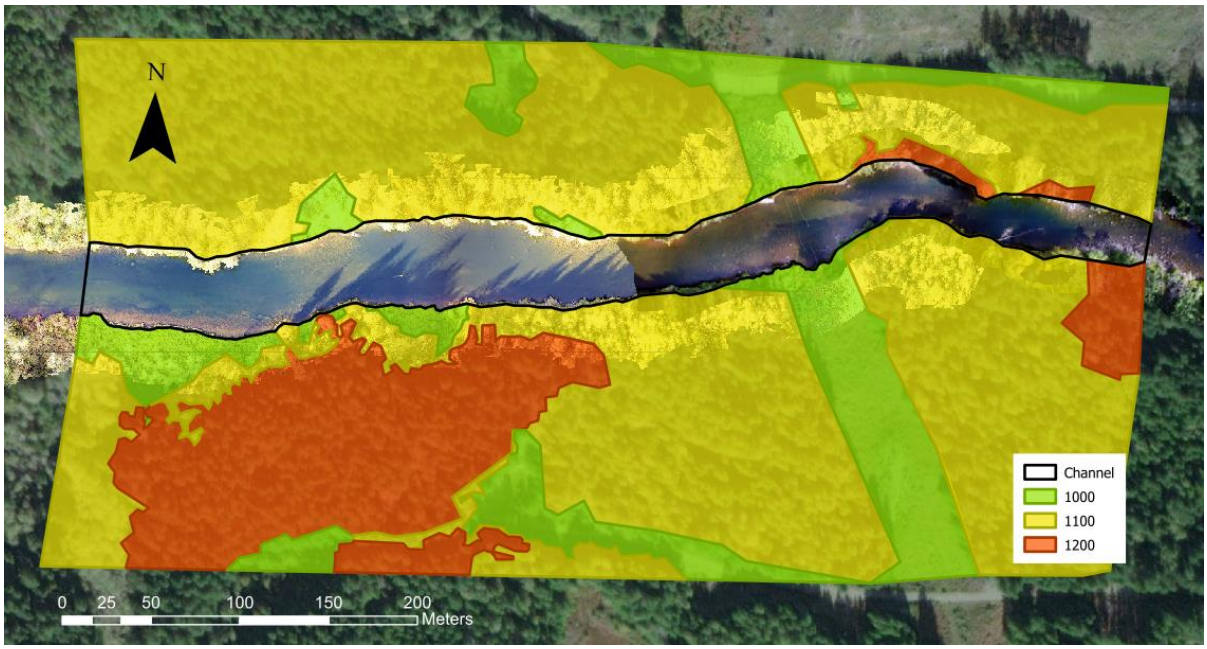


Figure 24 Roughness zones and corresponding IDs in updated model.

3.5 Sediment transport model

3.5.1 Gravel placement mix

The critical shear velocity thresholds were determined based on the design placement mix. The same thresholds were applied when evaluating both the existing bed condition and design placement conditions for due to the lack of information on the surfaces and fraction on the bed.

The approximate GSDs for spawning substrate used by each species was provided by Ecofish based on the Stream Habitat Restoration Guidelines from the Washington State Aquatic Habitat Guidelines Program (Saldi-Caromile et al., 2004). The pit run material was noted to approximately follow a well-graded mix of sand and gravel sized 0.5 to 75 mm, and that a moderate fraction of sand should be included. Following guidance from Ecofish, only the mobility of the Chinook mix was analysed because this species was most likely to benefit from the placement and this design mix was most likely to remain stable in the reach due to its relative coarseness.

Table 11 Gravel gradation for four target species. From West et al. (2023).

	Fraction for each species			
Size (mm)	**Sockeye**	**Coho**	**Steelhead**	**Chinook**
Pit run	0.12	0.08	0.08	0.10
3-12	0.23	0.23	0.23	0.19
13-50	0.51	0.43	0.43	0.38
51-101	0.12	0.23	0.23	0.21
101-150	0.02	0.03	0.03	0.12

Because 6 mm is expected to be the lower bound of usable spawning material for some small salmonids (Slaney & Zaldokas, 1997), the 3-12 mm size class was split into two size classes (3-5 mm and 6-12 mm) by assuming a normal distribution within the size class. To account for the contributions of the pit run material to each size class, the range of pit run sizes was assigned to classes based on a positive skewed distribution. As it was thought that the pit run material would provide the bulk of the fine content, it was assumed that 50% of the material would be sized 0.5-3 mm to align with the lowest bound of the defined size classes. The remaining 50% was distributed between the remaining size classes using a truncated normal distribution. It was assumed that 76 mm

corresponded with the D_{95} of the pit run material, thereby allowing for the calculation of the standard deviation of the material and the assignment of fractions in each size class. The calculated results are in Table 12, while resulting gradation after applying the described changes is shown in Table 13.

Table 12 Assumed pit run gradation

Size (mm)			Percent finer		
Min	**Max**	**Median**	**Min % Finer**	**Max % Finer**	**Total %**
0.5	2	1.75	0.05%	50.0%	49.9%
3	5	4.5	50.0%	53.3%	3.3%
6	12	9.5	53.3%	60.8%	7.5%
13	50	32	60.8%	90.4%	29.7%
51	100	76	90.4%	99.6%	9.2%
101	150	125.5	99.6%	100%	0.4%

Table 13 Gravel placement gradation

Size range (mm)	Median size (mm)	Percent fraction	Percent finer
0.5 – 2	1.75	5.1%	5.1%
3 – 5	4.5	2.9%	8.0%
6 – 12	9.5	17.3%	25.3%
13 – 50	32	41.0%	66.3%
51 – 100	76	21.9%	88.2%
101 - 150	125.5	12.0%	100%

3.5.2 Critical shear stress thresholds

It has been well-documented that in size-selective bedload transport is diminished in mixed-size beds, as finer fractions are subject to sheltering by larger grains while larger fractions tend to sit in shallow pockets and are more exposed to flow (Church & Ferguson, 2015). Consequently, hiding functions derived from bed GSDs are commonly used in engineering applications evaluating incipient motion. A reference Shields parameter of 0.045 is generally used to evaluate the incipient motion of gravel in fluvial environments (Buffington & Montgomery, 1997). However, it is noted that critical shear stress thresholds are sensitive to many factors applicable to this reach, as discussed in Section 2.4.

Correction of the selected threshold can at times be calculated through the tracking of tracer stones pre- and post-flood if the magnitude of the flood is known. As this could not be accomplished in this study due to the lack of sufficient data, a range of possible values was instead identified.

The hiding function method from Wilcock & Crowe (2003) was applied to a reference Shields parameter value of 0.045.

$$\bar{\phi} = \sum_{i=1}^{n} \phi_i f_i \quad [23]$$

$$D_g = 2^{\bar{\phi}} \quad [24]$$

where D_g is the geometric mean of the surficial GSD, ϕ is the median grain size of size class i measured in the negative phi scale, f_i is corresponding relative fraction in the size class, and D_g is the geometric mean of the sediment mix (taken to be equivalent to the mean surface grain size). The reference shear stress is calculated using:

$$\tau_{rm}^{*} = \frac{\tau_{rm}}{(S_g - 1)\gamma D_g} \quad [25]$$

where τ_{rm}^{*} is the reference Shields parameter (also referred to as the dimensionless shear stress) for the median grain size, τ_{rm} is the corresponding reference shear stress (N/m^2), S_g is the specific gravity of the sediment (typically assumed to be 2.65), and γ is the specific weight of water (N/m^3). The hiding function is given by Equations [26] and [27].

$$b = \frac{0.67}{1 + \exp\left(1.5 - \frac{D_i}{D_g}\right)} \quad [26]$$

$$\frac{\tau_{ri}}{\tau_{rm}} = \left(\frac{D_i}{D_{s50}}\right)^{b} \quad [27]$$

where b is 0.12 for $D_i/D_g < 1$ and 0.67 for $D_i/D_g > 1$, τ_{ri} is reference shear stress for the i^{th} size class. Assuming the median of each size class is representative of that class, the application of the equations to the design mix and a subsequent conversion to shear velocity yields the thresholds listed in Table 14. The design mix thresholds were used for the entire reach as there is insufficient data on the gradation of the existing bed material to calculate separate thresholds for different areas.

Table 14 Shear velocity thresholds for sockeye and Chinook gravel mixes

Size range (mm)	Median size (mm)	Shear velocity thresholds (m/s)
0.5 – 2	1.75	0.12
3 – 5	4.5	0.13
6 – 12	9.5	0.14
13 – 50	32	0.15
51 – 100	76	0.20
101 - 150	125.5	0.26

3.5.3 Shear velocity calculations

The calculation of shear velocity in 2D models is based on a product of the user-defined skin friction parameter. For parameterization using the Nikuradse roughness length in TELEMAC-2D, the method consists of converting the Nikuradse roughness to an equivalent Chézy value and transforming the Chézy value to a dimensionless skin friction coefficient before calculating the shear velocity.

$$C = 7.83 \ln\left(\frac{12h}{k_N}\right) \quad [28]$$

$$C_f = \frac{2g}{C^2} \quad [29]$$

$$u_* = \sqrt{\frac{C_f}{2}\,(u^2 + w^2)} = \sqrt{\frac{\tau_o}{\rho}} \quad [30]$$

where C is the Chezy roughness, C_f is the skin friction coefficient, and u and w are the depth-averaged velocities in the x- and y-directions.

This method is dependent on water depth, roughness, and velocity. In simulations where velocity gradients are very smooth, the outputs are highly sensitive to roughness. In models calibrated using user-inputted friction zones, areas of unrealistically higher or lower mobility can therefore result as artefacts of the prescribed roughness values.

An alternate method of calculating shear stress can be derived from a first principles approach that alters the 1D Saint-Venant momentum equation. Previously presented in Section 2.3.4 as Equation [9], the momentum equation was reformulated as:

$$u_* = \sqrt{g h_1 S_w - V(h_1 + h_2)\frac{\partial V}{\partial s}} \quad [31]$$

where h_1 is the depth of water above and upstream of the crest (m), h_2 is the depth of water below the control (m), S_w is the water surface slope in the direction of flow, V is the magnitude of the depth-averaged velocity (m/s) and $\partial V/\partial s$ is the velocity slope in the direction of flow (1/s).

This novel interpretation of the SVE accounts for the unique hydraulic characteristics at lake outlets, where the steep adverse bed gradient can cause the crest to act as a pseudo-weir. Gravity would therefore only act on the upper layer of the fluid above the crest elevation, while the lower portion is dragged upwards and across the bed by the upper layer through convective acceleration. The shear velocity consequently depends only on local hydraulic characteristics instead of user-imposed roughness values that were set during calibration. The verification of this hypothesis was outside the scope of this thesis but is presented here as a future research opportunity into lake outlet hydraulics. A diagram of the hypothetical fluid layers is shown in Figure 25.

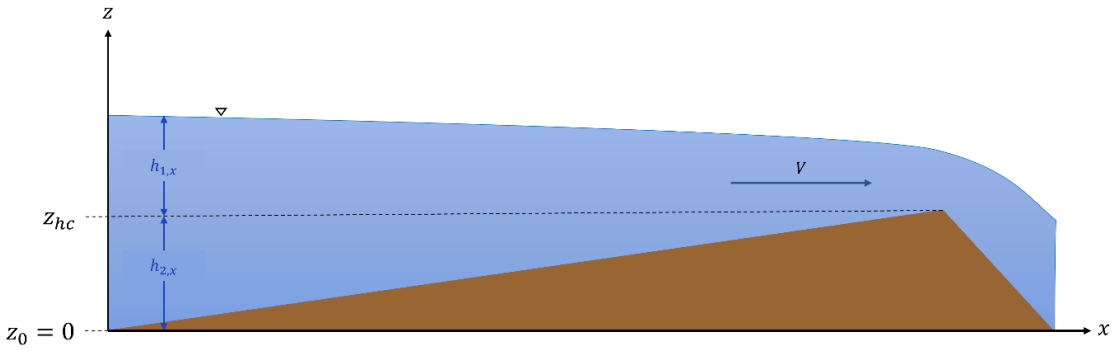


Figure 25 Hypothetical diagram on lake outlet hydraulics.

The steady state water surface and velocity slopes and aspects were computed using the T3 Element Average surface extraction tool on Blue Kenue. This tool calculates the slope and aspect at each node using cross-products to extract an average of all the elements connected to the node. The slope and aspect values were then projected in the direction of stream flow based on the modelled velocity vectors. An in-house MATLAB (The Mathworks Inc., 2022) code that used the package Telemac Tools (Benson, 2011) was written to extract the remaining parameters and calculate the shear velocity at each model node.

3.5.4 Critical velocity filters

Both shear velocity calculation methods overestimated shear velocity in some regions of the computational domain. In the initial model which employed friction zones, the classical friction-based method appeared to overpredict mobility near the banks and in the floodplain due to the higher friction zones in these areas despite being subject to near-zero or zero velocities. Comparatively, the SVE momentum method appeared to overestimate shear throughout large portions of the reach and did not reflect a gradual increase in shear expected in an accelerating flow channel.

Consequently, a critical velocity filter was applied based on thresholds obtained from Figure 26 (S. E. Coleman & Smart, 2011), such that a particular size will only be classified as mobile if both the critical shear velocity and the critical velocity thresholds for that size is met. The mobility for any given size class at each node was set to zero if the shear velocity threshold that class is exceeded but the corresponding velocity threshold is not met. The modelled velocity is then evaluated against increasingly lower size classes until this criterion is also met. The size class at which the velocity criterion is met then becomes the size predicted to be mobile at that node.

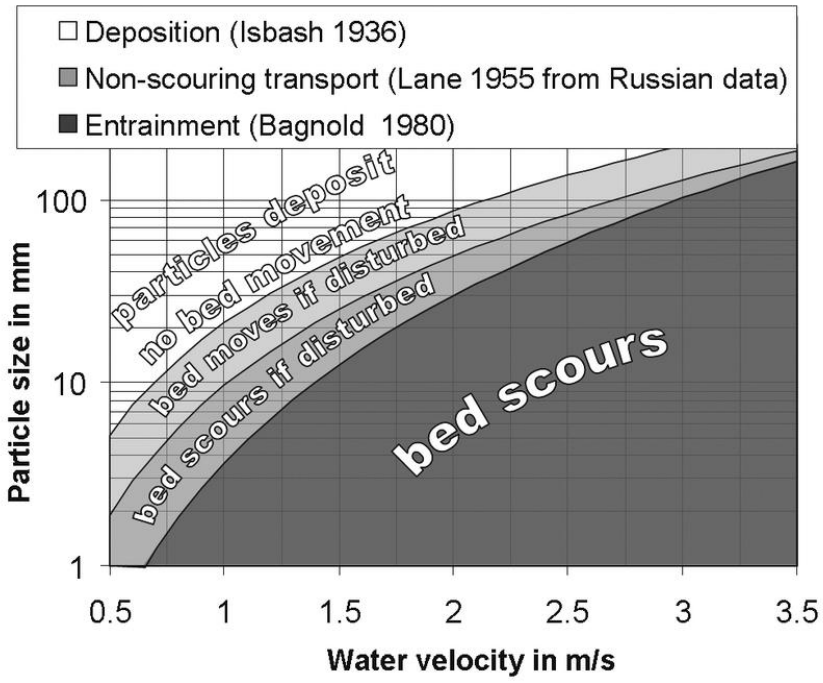


Figure 26 Critical average velocities for gravel mobility. From S. E. Coleman & Smart (2011).

The “bed moves if disturbed” line was used to obtain the thresholds for each size class, as summarized in Table 15. The 110 mm threshold was used for the 101-150 mm class as the graph only extended up to this size. The thresholds were decreased by 20% to remain conservative.

Table 15 Critical velocities for entrainment of key size classes, from Figure 26.

Upper limit of size class (mm)	Critical velocity (m/s)	Adjusted critical velocity (m/s)
2	0.50	0.40
5	0.75	0.60
12	1.05	0.81
50	2.00	1.60
100	2.70	2.16
110	3.50	2.80

3.5.5 Numerical model validation using tracer stones

The highest flow event in the first year of study peaked at 146 m^3/s, wherein the maximum Froude number across the crest was 0.47. The model was run with this discharge and a downstream boundary condition of 196.72 masl over the existing bed topography. The predicted mobility under this flow scenarios was compared with the travel distances, L (m), of the tracers from the transects at which they were placed and the size of each displaced tracer.

3.6 Engineering design criteria for spawning gravel enhancement projects

Simulations were run over the existing bed topography and a design placement scenario (Appendix D). Four design criteria were evaluated, including: i) gravel stability under select return period flows, ii) hydraulic habitat suitability, iii) fines deposition risk and iv) fines flushing potential. Gravel mobility for the six size classes was evaluated by comparing the modeled and filtered shear velocities with critical shear velocity thresholds, as described in Section 3.5. Although Chinook tend to spawn in gravel substrate between 13-102 mm (Slaney & Zaldokas, 1997), the species has been found to spawn in gravel as large as 150 mm (Washington State Department of Ecology, 2021). Thus, the stability criterion was considered fulfilled if gravel in the 100-150 mm class was stable under the select design flow rates. The stability of this size class is represented by the mobility threshold for 126 mm grains, which is the median of the size class. The remaining criteria are described in the

following subsections. The QGIS (QGIS Development Team, 2022) plugin PostTelemac (Artelia Eau et Environnement, 2021) was used to visualize the results of the analysis for each criterion.

A gravel placement scenario was modeled for Ecofish to evaluate post-construction changes to the hydraulics and gravel mobility patterns. The methods and results of this exercise are included in Appendix D.

3.6.1 Hydraulic habitat suitability index curves

Habitat suitability was described using habitat suitability index (HSI) curves, which consist of assigned weightings to discrete intervals of key physical habitat parameters including flow depth, current velocity, and substrate size. These indices are unique to each life stage of each species, and can be used to predict ecological responses to channel modifications on a microhabitat scale when coupled with 2D or 3D hydrodynamic models (Füstös et al., 2021; Webb et al., 2022).

The current velocity and water depth HSI curves shown in Figure 27 and Figure 28 were provided by Ecofish based on existing local models for the spawning habitat of the target species. The HSI curves for substrate were omitted, as the gravel mix was to be designed and sized according to the optimal substrate size for the target species (Ptolemy, 2001; West et al., 2023). Each mesh node was evaluated to be suitable if the HSI for both parameters met or exceeded 0.5.

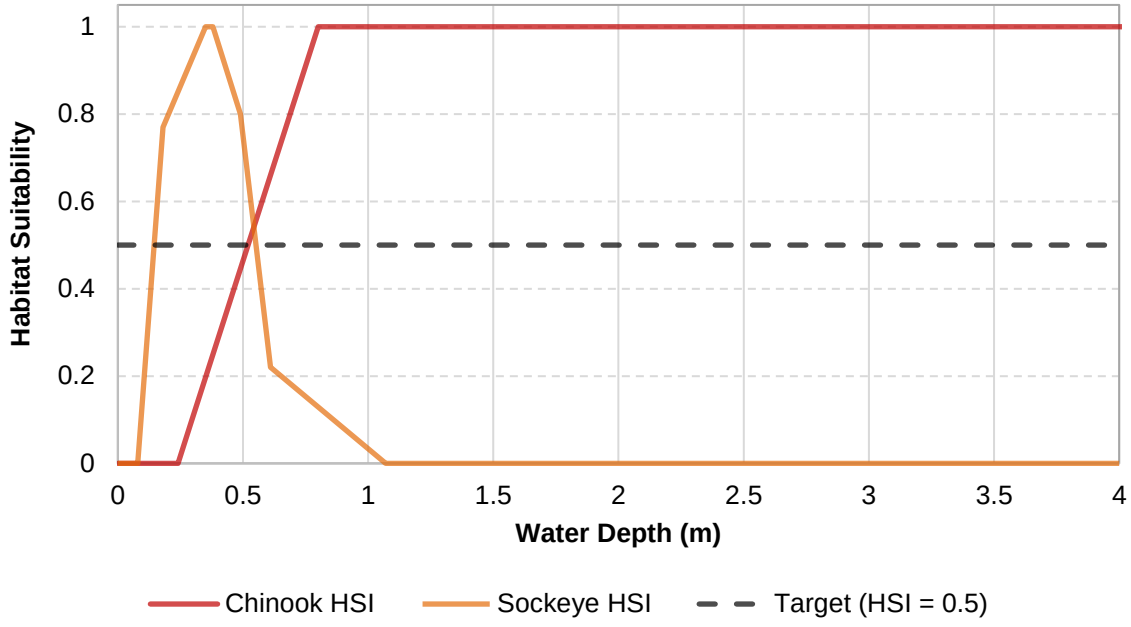


Figure 27 HSI curve showing the spawning suitability of Chinook and sockeye salmon to current velocity. From Ptolemy (2001) and West et al. (2023).

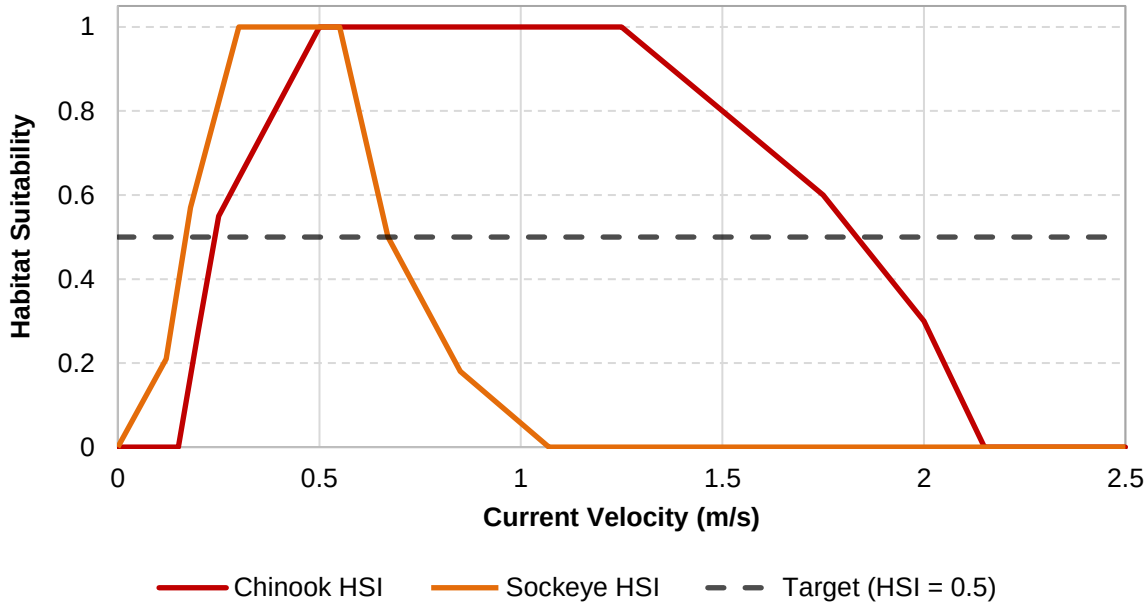


Figure 28 HSI curve showing the spawning suitability of Chinook and sockeye salmon to water depth. From Ptolemy (2001) and West et al. (2023).

3.6.2 Interstitial fines deposition and flushing

The risk of fine intrusion in the interstices of the placed gravel was evaluated using two methods. First, the risk of sand deposition was quantified by comparing the flow velocity at each node under the 7Q10 flow to the settling velocity for 0.5 mm grains obtained from the Hjulström (1935) curve. From Figure 29, the settling velocity for this particle size is 0.3 m/s. Each model node was defined to be at risk for deposition if the settling velocity exceeded the modeled flow velocity.

Second, the likelihood of the surficial sand deposits being mobilized was evaluated at the flushing flow (defined as 400% of the mean annual discharge by Ptolemy & Lewis, 2002). A Shields value of 0.021 was used which is recommended for surface flushing of gravel bed rivers (Milhous, 1998; Reiser et al., 1985). Like the gravel mobility assessment, a hiding function was applied to the sand under the assumption that the deposited fines are negligible in the gradation of the bed material such that it remains the same as the design mix. Although this assumption is unrealistic, it provides a conservative estimate of areas likely to flush, as the hiding effect inhibits fine grains from mobilizing.

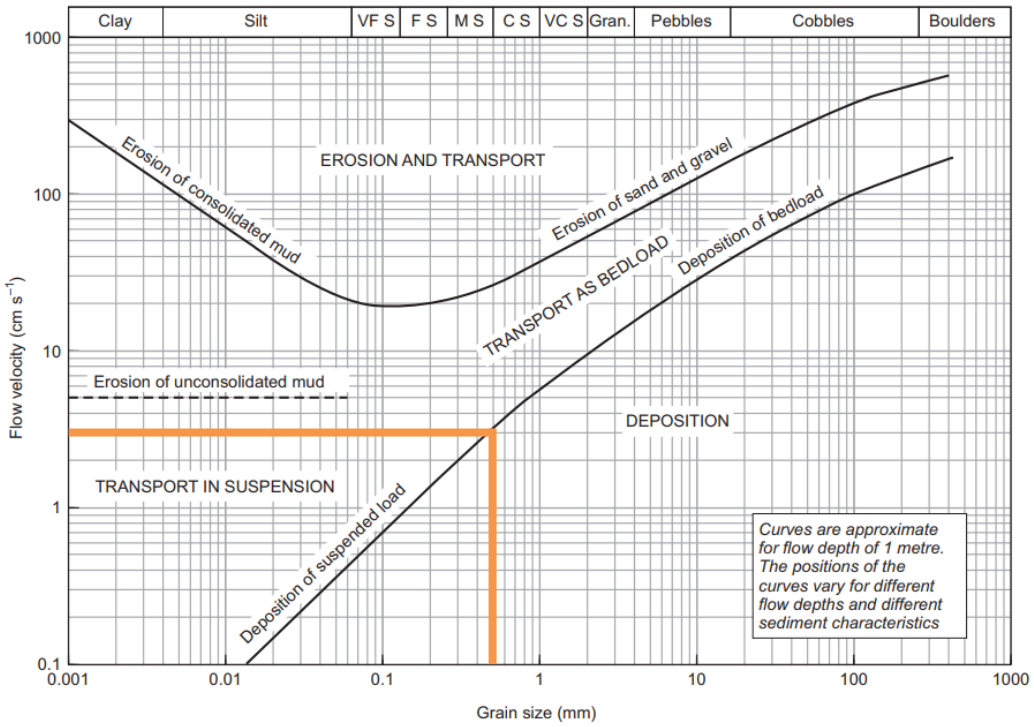


Figure 29 Hjulström (1935) curve. Adapted from Nichols (2010).

Chapter 4
Results

4.1 Field investigations of sediment transport

4.1.1 Existing sediment sources

Investigations into two delta formations at the lake-stream boundary were completed to investigate potential sediment sources to the reach. These sources likely result from nearby logging activity, as shown in Figure 30a, while the streams leading into the delta can be observed in Figure 30b. At the time of the field visit, no flow was present in the streams and the beds were fully exposed, which suggests that the streams are ephemeral and only activate under runoff from rain events.

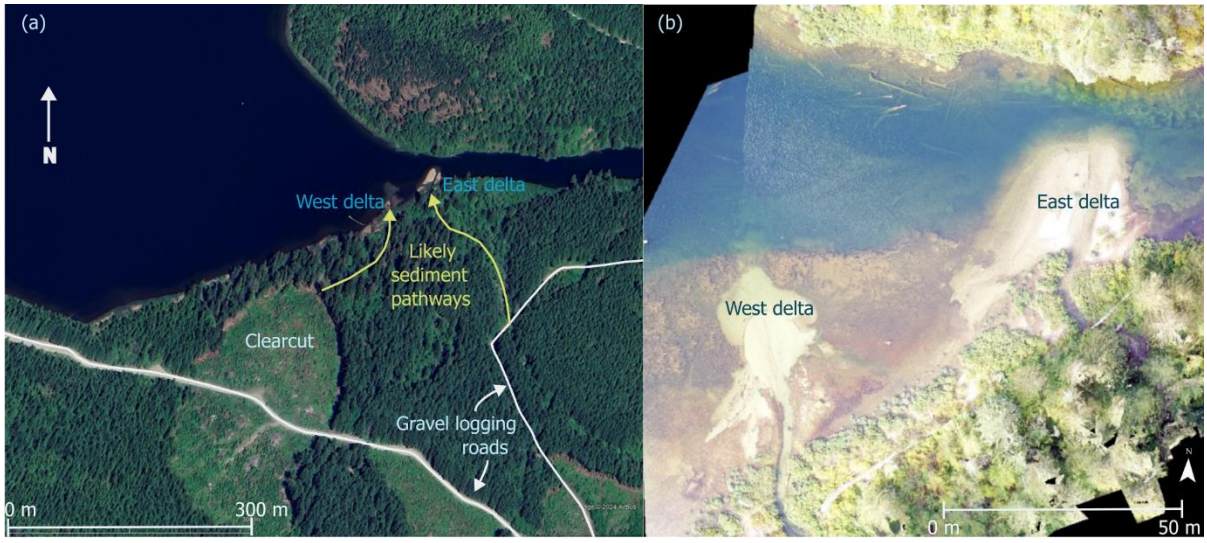


Figure 30 Aerial views of the delta formations located at the boundary between Muchalat Lake and Muchalat River from (a) Google Earth showing likely sediment pathways and (b) from the RPAS orthoimagery showing the small ephemeral streams creating the deltas.

The substrate in the east delta, shown in Figure 31, comprises of loose sandy gravel, with sizes generally ranging from sand to medium gravel. Sparse vegetation was present in the delta plain which indicates that the flow pathways generally follow a preferred route. The gravel likely originates from the gravel road southeast of the delta. The material in the west delta is comparatively finer and is composed primarily of sand. A photo of the deposited sand is shown in Figure 32. Between the two

deltas lies an area of accumulated fines (silt and smaller) and lacustrine vegetation, seen in Figure 33. This material likely results from the topsoil released by the logging in the nearby clearing, which may be why it is relatively finer and more organic than the east delta.



Figure 31 (a) Ground view of the east delta (canoe paddle for scale) showing the footprint of the active channel and remnant water pooled on the left side of the image. (b) The material is small-medium gravels.



Figure 32 Deposited sand bar in the footprint of the west ephemeral stream. Remnant water is pooled in the deeper sections, but the water is stagnant.

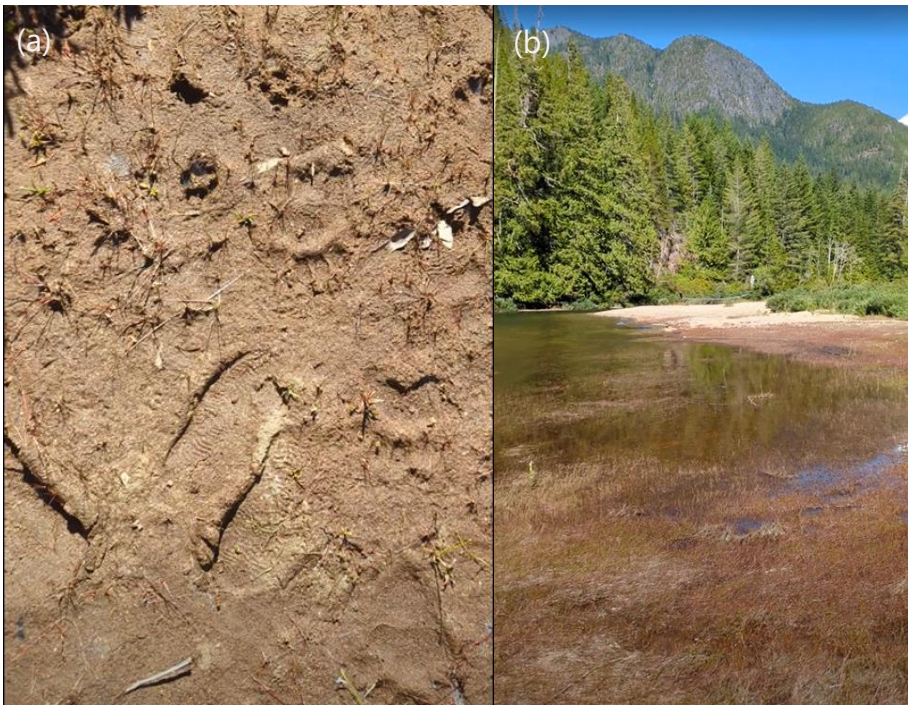


Figure 33 View of the (a) fine substrate and (b) vegetation between the two deltas

4.1.2 Sediment pathways through a vegetative bed rise

Examination of the orthoimagery revealed a bed rise near BM046 consisting largely of wood and fines, shown in Figure 34. As this bed rise is a potential gravel placement location, the substrate and transport pathways were assessed by swimming across the channel while recording video footage of the bed with a GoPro during WFT2.

A sequence of screenshots from the videos showing the bed from the left to right banks is presented in the following figures. The deposited logs are mostly concentrated on the right side of the channel and oriented in the direction of flow while smaller branches are in higher abundance on the left side. Similar patterns follow the sediment deposition, with finer material (sands and silts) more commonly observed on the left side and larger (gravel and larger) substrate observed on the right side. The wood deposition pattern suggests that the left side is a more active transport zone for both wood and sediment, while the right side is relatively more immobile.



Figure 34 Aerial view of the vegetative bed rise

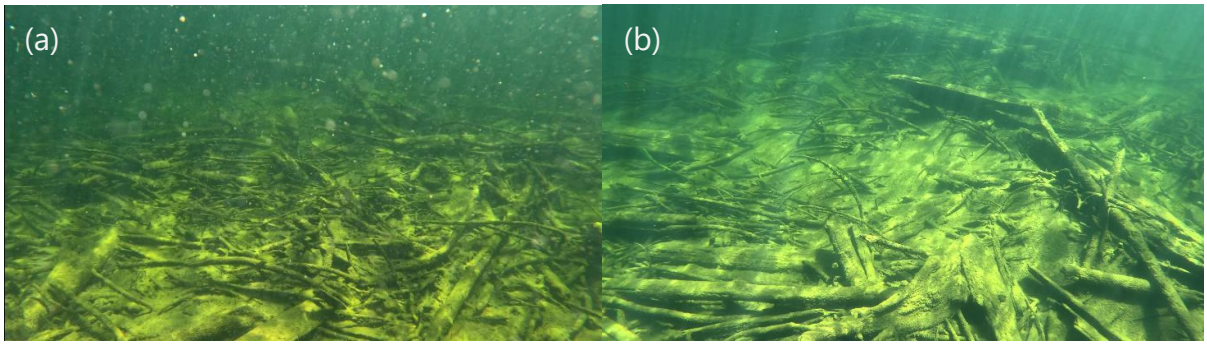


Figure 35 Bed view on river left showing randomly deposited branches and fines.



Figure 36 Bed view of the center-left of the river showing larger areas of deposited fines.

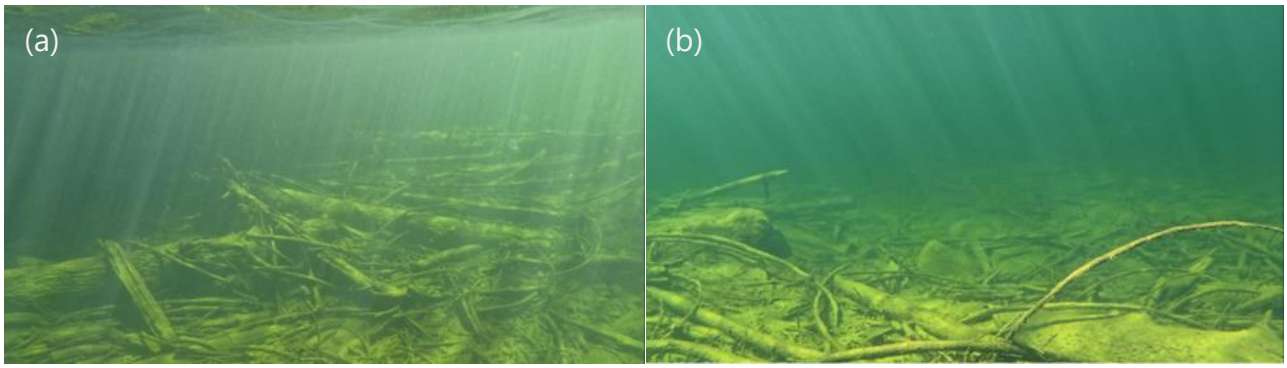


Figure 37 Bed view of the center-right of the river, showing a mix of logs and branches, with deposits of gravel visible under a layer of algae and/or fines.

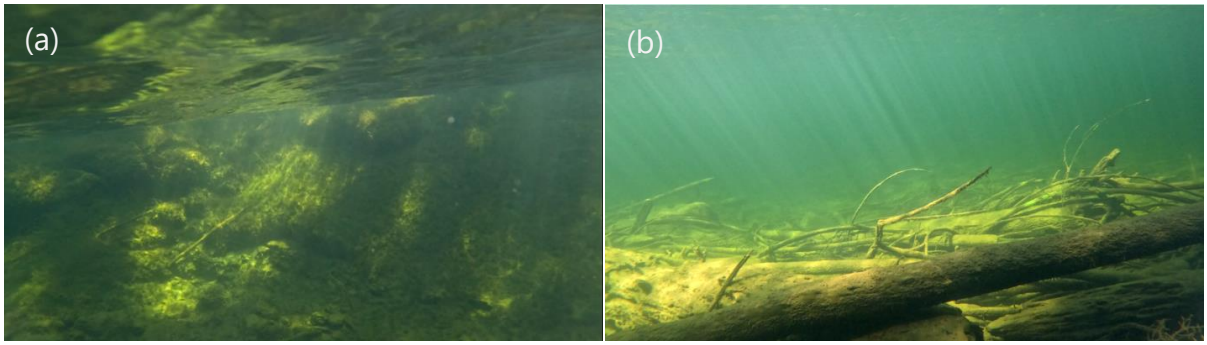


Figure 38 View of the right side of the channel showing logs and larger branches. More algae are visible here, with substantial weedy material growing on the boulder at the channel edge. Some gravel and cobbles are visible under layers of algae and/or fines.

4.2 Hydrodynamic model calibration and performance

4.2.1 Calibration results for HiFT flow scenario

The location of the transects relative to the modeled velocities under the HiFT scenario are shown in Figure 39. The channel friction value was varied between 0.37 to 0.41 m, with the performance statistics of the best result (0.39 m) reported in Table 16. The measured and modeled velocities were plotted together to identify deficiencies in the model. Sample figures are shown in Figure 40.

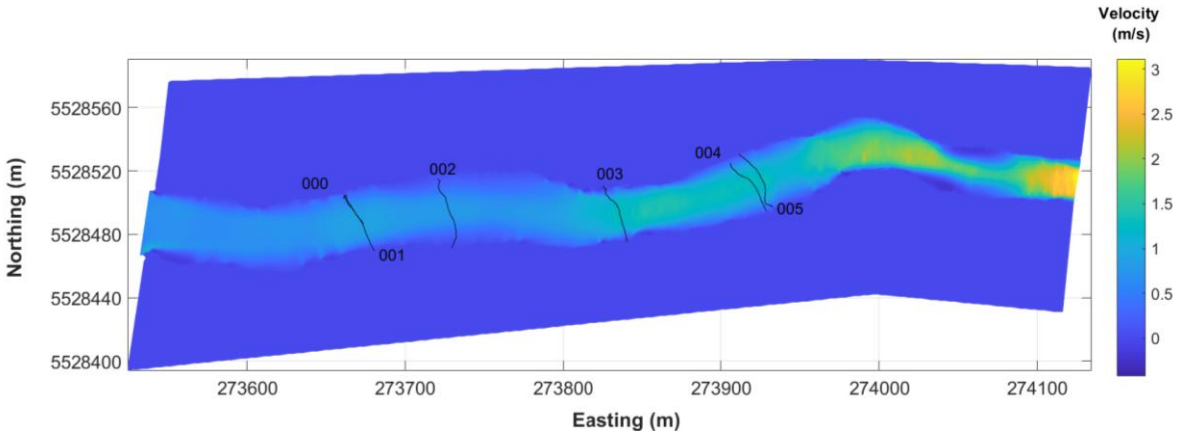


Figure 39 Location of the six ADCP transects collected during EFT3 superposed over simulated velocities from the simulation using the calculated discharge on this field day (123 m^3/s).

Table 16 Performance statistics for velocity during the HiFT calibration scenario (123 m^3/s)

Transect	R^2	NSE	RMSE	Percent bias
XS 000	0.96	0.93	0.082	-4.07%
XS 001	0.76	0.71	0.140	0.18%
XS 002	0.78	0.77	0.156	-0.81%
XS 003	0.84	0.48	0.250	-2.85%
XS 004	0.74	0.61	0.185	-2.75%
XS 005	0.84	0.79	0.186	-8.93%
Average	0.82	0.71	0.167	-3.20%

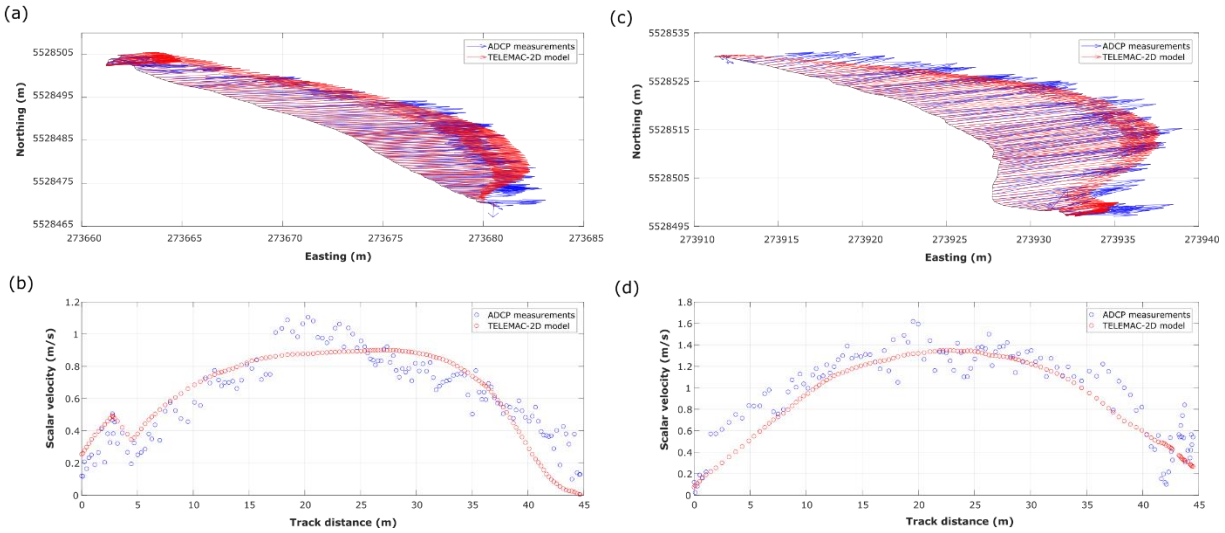


Figure 40 Sample plots comparing measured and modeled velocities vectors and magnitudes at (a, b) transect 001 and (c, d) transect 005 for the HiFT calibration scenario.

The comparison of the measured and modeled velocity vectors in Figure 40a and c reveal that the overall directions of the measured vectors are slightly offset from the modeled results. The vectors near the bank also appear somewhat aleatory, likely due to the unreliability of the ADCP at shallow depths. The magnitudes plotted in Figure 40b and d show that the model adequately captures average velocity trends but shows some discrepancies with the measured data near the banks. The peak velocity in transect 001 does not appear to have been captured in Figure 40b, likely because the transect is located further upstream where the bathymetry data is less detailed. The lateral changes in velocity are better captured in transect 005 (Figure 40d) which is located further downstream, but the model slightly underpredicts the measured velocities.

4.2.2 Validation results for the MeFT flow scenario

The performance statistics reported in Table 17 for the MeFT scenario (10.2 m^3/s) indicate that model does not perform as well at this discharge. While some individual transects appeared to perform adequately, others were unable to replicate the measured data, resulting in moderately poor average and median R^2 values. Similar conclusions can be drawn from the NSE values, where a near-zero average NSE suggests that a similar level of performance could have been obtained from a 1D model. Interestingly, the range of RMSE values from this flow scenario are similar to those calculated from the higher stage HiFT calibration scenario, which suggests that the apparent poor performance may be

at least partially attributed to the absolute margin of error expected in this model. The average bias present in this model is also comparable to that of the HiFT scenario, but greater bias is observed in individual transects than the previous model run. Thus, reach-level model interpretations may be adequate, but that conclusions relying on high spatial resolution should be used with caution.

Table 17 Performance statistics summary for MeFT flow scenario (10.2 m^3/s)

Parameter	R^2	NSE	RMSE	Percent bias
Range	0.00 – 0.85	-3.27 – 0.68	0.034 – 0.147	-36.3% – 20.8%
Median	0.39	0.23	0.061	-2.8%
Average	0.43	-0.15	0.055	-3.6%

The decreased performance for MeFT is likely caused by the low quality ADCP data associated withshallower flows, the lack of significant variation in the measured velocities across certain transects, and the inability of the model to account for high relative roughness. Most flow resistance equations were not formulated for scenarios with low relative submergence, much less for partial submergence, which is common at this site due to the prevalence of boulders. These equations form the basis for most hydraulic models despite recent proposals to alter these equations to account for the full range of relative submergence scenarios (e.g., Ferguson, 2007).

The poor replication of velocities at MeFT, which has relatively low submergence indicates the continued deterioration of model performance at increasingly lower flows. The model results at flow rates lower than the MeFT flow scenario (i.e., the 7Q10 scenario) should also be treated with caution.

4.3 Sediment transport model

4.3.1 Comparison of shear velocity distributions calculation methods

The filtered shear velocity distribution for the 20-year return period flow produced by the initial model using the two methods is shown in Figure 41. When compared with the friction zones used in the calibration, the shear velocities predicted by the classical friction method shows a clear alignment between the predicted mobility near the left bank in the upstream half of the channel and the vegetative bed rise with the edges of the defined calibration zones. In the downstream half where

calibration zones were not as heavily used, the mobility patterns follow the expected accelerating gradient from upstream to downstream, with areas of higher mobility predicted near the thalweg.

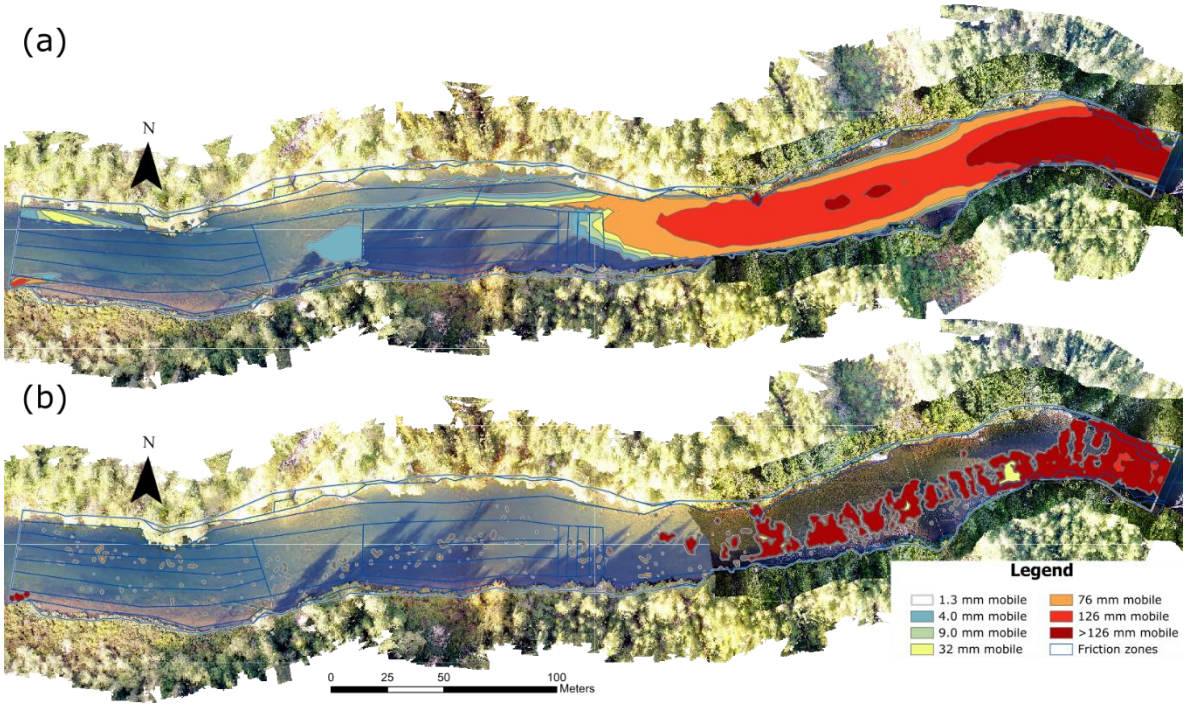


Figure 41 Gravel mobility predictions for the 20-year return flow by the initial model using the (a) classical friction method and (b) Saint-Venant momentum equation method.

The SVE mobility results shown in Figure 41b are clearly independent of the calibration roughness zones, especially when compared to Figure 41a. However, the mobility gradient following the flow acceleration manifests through the density of the discontinuous dark red patches representing the mobility of grains sized over 126 mm, instead of the continuous increase in shear stress represented by the friction method. The SVE method is highly sensitive to local slope-based parameters, including the surface water, velocity, and bathymetric slopes, thus the averaging tool used to calculate the slopes is expected to impact the results of this method. Additional pre- or post-processing is likely required to achieve a more continuous mobility pattern.

Given the need for further research to validate the SVE method, the mobility predictions in the remainder of this thesis employed the friction method. A constant in-channel friction value was used

in the updated model to avoid the artificial shear velocity patterns induced by the friction zones and provide more confidence in the validity of the results than the original model.

4.3.2 Predicted gravel mobility under select design flow rates

The mobility of each gravel mix size class was predicted for the six return period design flows. The 2-year, 20-year and 100-year return flows were used as representative flows to show the progression of mobility patterns through increasingly high flows. These results are presented in Figure 42.

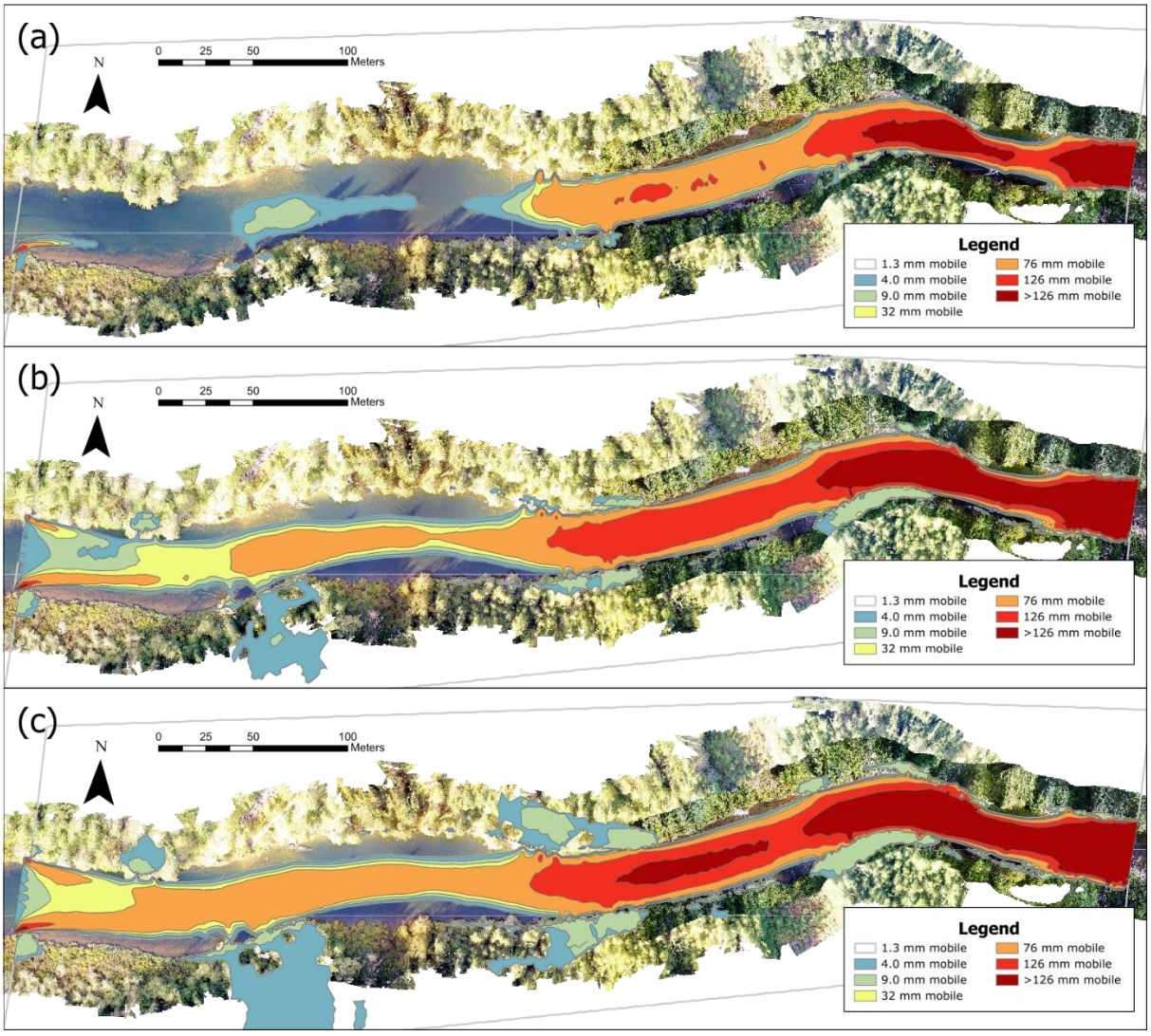


Figure 42 Gravel mobility predictions using the updated model for the (a) 2-year, (b) 20-year and (c) 100-year return flows.

Under the 2-year return flow, mobility of the spawning sizes (13-150 mm, represented by the yellow and two orange colours) is predicted only in the downstream half of the study reach. The largest size class in this range is predicted to start undergoing significant mobility near the crest, with some small zones of predicted mobility in the transition section preceding of the power line. Cobbles exceeding this size are predicted to mobilize only in the section past the crest. A small section of mobility for the smallest gravel sizes is predicted in the upstream section, stemming from the vegetative bed rise.

At the higher return flows, flooding effects start to become apparent, as there are areas of non-zero velocity and shear velocity in the floodplain. A corridor of mobility for the gravel sizes of interest extends to the previously disconnected mobility zone over the vegetative bed rise in the 20-year return flow, while the mobility of smaller sizes is shown to extend to the upstream boundary. The gravel mobility corridor extends to the boundary and fills out more fully through the 100-year return flow, as the cobble-sized substrate also begins to mobilize in the transition section.

4.4 Tracer stone recovery

4.4.1 Tracer recovery rates

A total of 158 of the 168 seeded tracers were recovered during WFT2, representing an overall recovery rate of 92%. Compared to typical recovery rates of 10-90% for most RFID tracer studies (Liébault et al., 2023), the high recovery rate likely resulted from relatively low tracer mobility which was the result of an unusually dry winter which led to a lower freshet peak than historical averages. The surveyed locations of the tracers are shown in Figure 43.

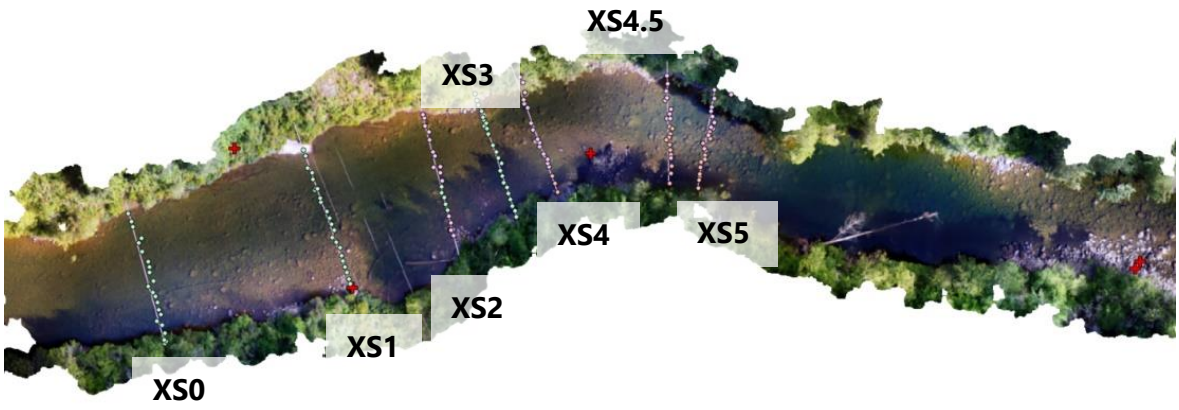


Figure 43 Recovered tracer stone locations shown as coloured points. Red crosses denote BM locations, while the transect lines are shown as white lines.

The recovery rates for individual size classes range from 89% for the small (45-64 mm) stones to 95% for the other two sizes (64-90 mm and 90-128 mm). Larger stones were overall more easily found, either owing to relatively lower mobility or being more visible in the channel. Although stones that were not found may have been buried, mobilized, or moved by wildlife, the recovery rate was also influenced by the level of effort put into the recovery at each transect. The level of effort was dependent on the hydraulic conditions at each transect and the time of day the recovery effort occurred. The transects (e.g., XS0 and XS4) completed at midday and in the afternoon were subject to higher wind conditions which affected the navigability of the canoe and led to greater swimmer fatigue. Figure 44 shows the recovery rates at each transect by size.

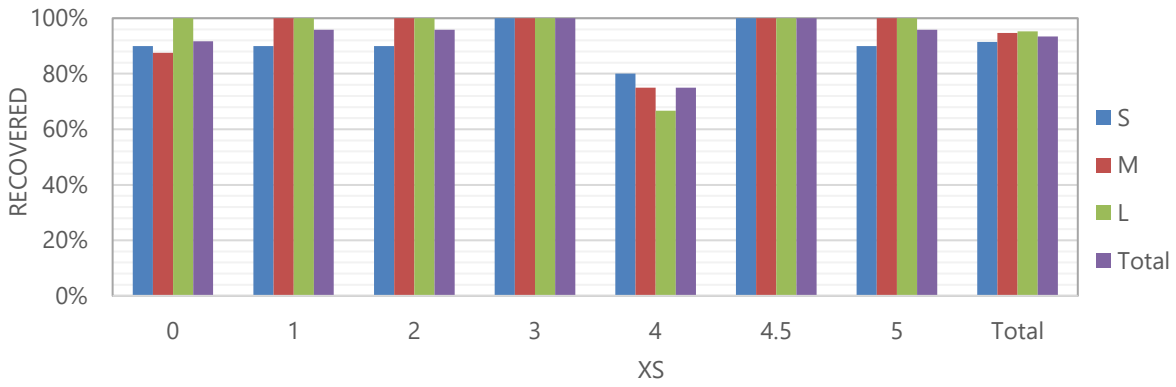


Figure 44 Percentage of recovered stones by cross-section and size. Medium (M) and large (L) stones were generally more readily found than small (S) stones.

Figure 45 summarizes the rates by position. The recovery rates in the outer side of the bend of the channel were notably lower than the inner half of the bend. These results agree with the intuitive understanding that mobility should be higher in the channel thalweg through which most of the flow is routed. However, these findings disagree with the modelled shear velocities, which predicted higher mobility on the inner side of the bend.

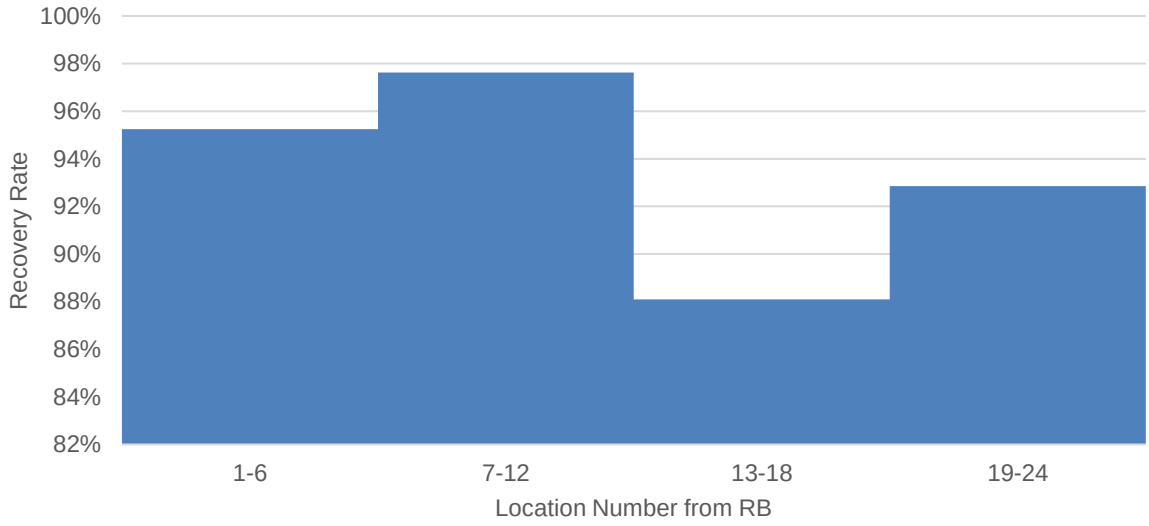


Figure 45 Recovery rate by lateral seeded location in the channel.

4.4.2 Tracer mobility patterns

Since the initial positions of the stones were marked based on relative distances across a transect line, the transect lines representing the initial positions were delineated based on the locations of the stones found on the banks, as these stones were least likely to move. The distance from each point to their respective transect of origin was calculated and grouped into three classes (0.0-0.5 m, 0.5-1.0 m and >1.0 m). The upper threshold of the first class was selected to account for error while seeding the tracers because the exact locations of the tracers were not recorded during WFT1. The limit of the second class was selected based on the expected antenna read range to account for stones that were detected by the antenna but whose location could not be visually verified. Generally, most tracers were discernible by eye in the river, hence the surveyed locations should represent the precise location of the stone (with error on the order of ±0.5 m due to the need for the swimmer to hold the prism pole steady while treading water). Three stones were found once via the antenna but were not surveyed as they could not be located again (tracer IDs 553, 413, and 452). The overall mobility pattern is plotted in Figure 46.

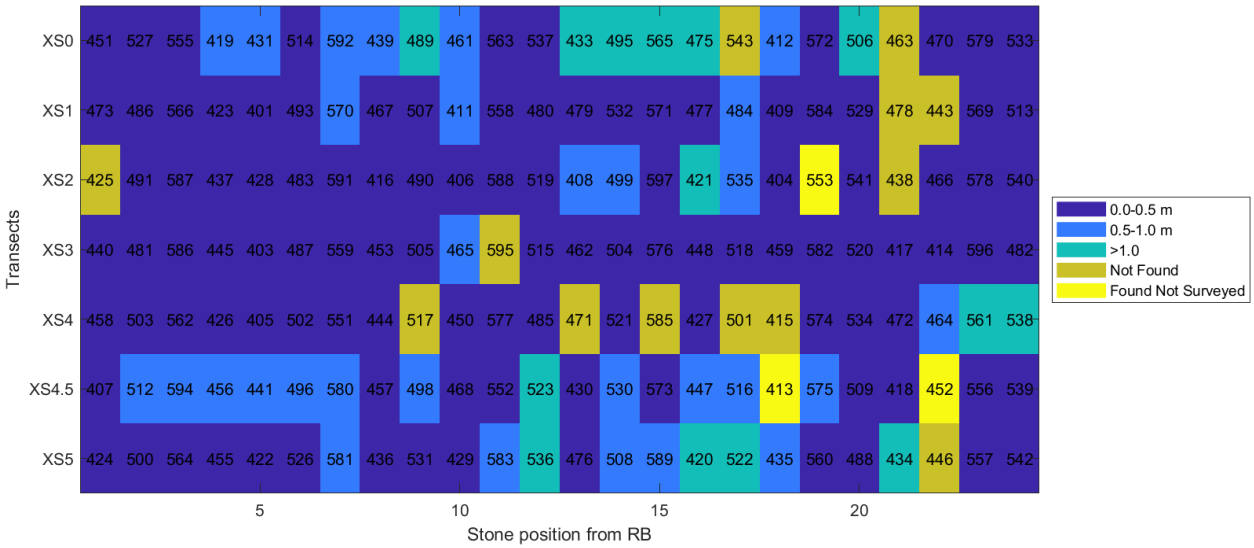


Figure 46 Mobility pattern based on seeding location, with the numbers in each cell representing the last three digits of the tracer's unique tag number.

The greatest mobility appears to be observed in XS0, with half of the stones appearing to deviate significantly from the transect line. The results contradict the hypothesis that the stones should remain generally immobile at this transect due to the relatively deeper and slower flow. Other than XS0, the

remaining transects show a general pattern of increasing mobility from upstream to downstream, especially on the left side of the channel. The mobility patterns in Figure 45 and Figure 46 reveal that the stones are near the threshold of mobility through the thalweg of the channel but are generally stable on the right side of the reach. The high recovery rate indicates that the 2023 freshet was incapable of fully mobilizing gravels in most of the reach where the tracers were placed.

4.4.3 General mobility validation by size class

The tracer movements were compared with the gravel mobility predicted by the updated model in Figure 47. Some coherent patterns are observed—most notably that mobile tracers in XS4.5 and XS5 appear to agree with the predicted areas of higher mobility—however, the model appears to be generally overpredicting mobility through most of the reach. Assuming that that the three tracer sizes can be represented by the "32 mm mobile", "76 mm mobile" and "126 mm mobile" categories, greater tracer mobility should be observed XS3 and XS4. However, the small tracers in these transects were generally found to be immobile, even in the center of the channel where they were predicted to mobilize. Nonetheless, given the relatively lower recovery rate at XS4 (75%), it is possible that more stones did mobilize at this transect, but were not found during the recovery effort.

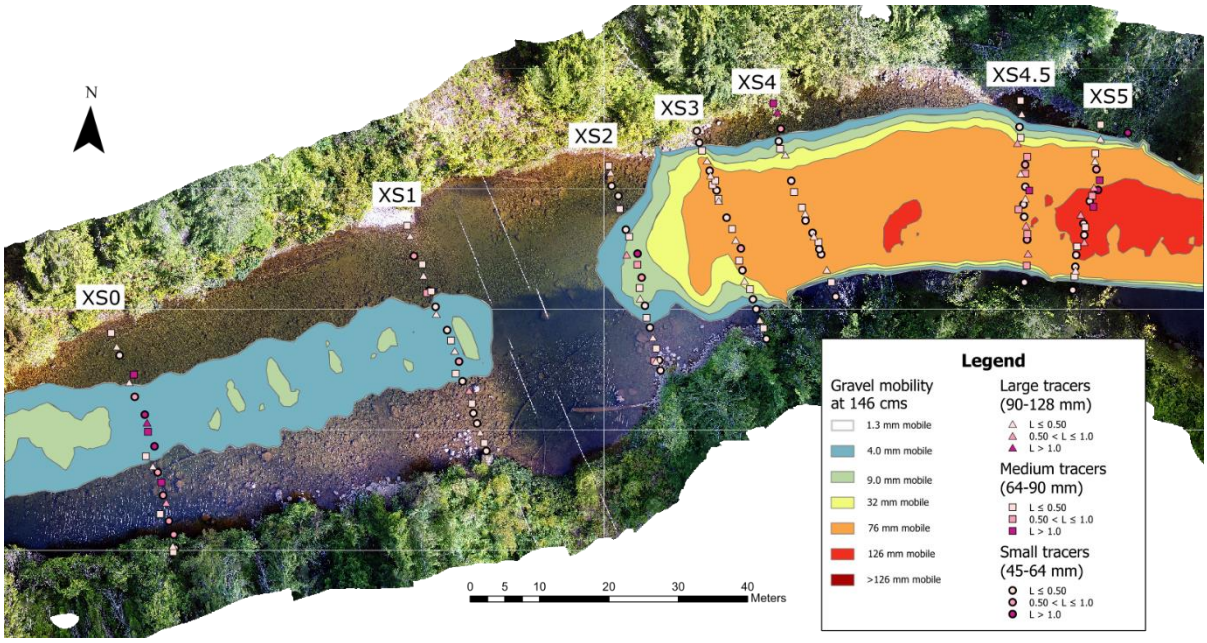


Figure 47 Comparison of the modeled gravel mobility predictions under the peak 2023 flow (146 m^3/s) with recovered tracer stone locations, categorized by size and travel distance, *L* (m).

Although XS0 appears to show significant mobility compared to the model predictions, these results are anomalous when compared with the tracer movements in the other transects. The flow is considerably deeper and slower at this cross-section and is thus expected to experience lower shear stress and reduced mobility. However, the tracers were placed at XS0 by dropping the stones from a boat, while placement at other transects were completed by either wading or swimming. The deep flow and high wind loading at this transect also created difficulties in navigating the stream when surveying the locations of the found tracers. The compound error from the placement and recovery at XS0 likely exceed 1 m, and thus leads to inconclusive results in this section of the channel.

The limited movements of the tracers suggests that the grain sizes represented by the tracer stones were near the threshold of mobility under the peak flow during the seeding year. The peak flow during the freshet flood in 2023 was lower than typical levels due to the relatively dry fall and winter that resulted in less snow storage and consequently snowmelt. Calibrating the sediment transport model by varying the Shields parameter to a reach-appropriate value was therefore not possible, as the limited tracer movements did not provide sufficient information on the mobility patterns in the reach. As the model appears to be overpredicting the field conditions, omitting the calibration is expected to result in a more conservative estimate of areas that are likely resistant to scour.

4.4.4 Direct mobility validation by tracer characteristics

The high-level comparison in the previous section is useful for validating the sediment transport predictions for the assessment of design criteria since it uses the same method as the one applied for the engineering analysis. However, it does not provide an exact validation, as individual particle characteristics such as density, size and shape can influence its susceptibility to incipient motion. A direct comparison between modeled shear stress and observed mobility using clast-specific parameters provides a better understanding of the performance of the sediment transport model.

The tracer stones seeded at XS0 were omitted from this analysis due to the high uncertainty associated with their initial positions, which resulted in apparent anomalous patterns. The initial positions of the remaining found tracer stones were approximated based on the delineated transect lines and field notes on the relative distance between adjacent stones. The modeled shear velocities were interpolated at each initial position and converted to shear stress values.

The equation for the expanded Shields criterion that accounts for the full force ratio was used to obtain the modeled dimensionless shear stress, τ^*, acting on each particle:

$$\tau^* = \frac{load}{strength} = \frac{\tau A_{s,i}}{(\rho_{s,i} - \rho)g\forall_i} = \frac{\tau r_{A,i} r_{B,i} \pi}{m_{s,i} g} \quad [32]$$

Where $A_{s,i}$ is the projected area of the particle exposed to flow (m^2), m_s is the submerged mass of the particle, $\rho_{s,i}$ (kg/m^3) and $\forall_i$ (m^3) are the clast-specific density and volume of the i^{th} tracer. The typical equation for dimensionless shear stress (i.e., the Shields parameter, Equation [25]) assumes that the ratio between the projected area $A_{s,i}$ and the particle volume can be approximated by the B-axis radius r_B due to the lack of knowledge on particle characteristics. However, the expanded criterion is more accurate, since it uses the first-principles definitions of the forces which account for the clast-specific dimensions along all three axis and particle density.

The clast-specific reference shear stress was then calculated using the Wilcock & Crowe (2003) equations (Equations [23] to [27]) (assuming a $\tau^*_{rm} = 0.045$), and converted to dimensionless values:

$$\tau^*_{r,i} = \frac{\tau_{r,i}}{(\rho_{s,i} - \rho)g d_{b,i}} \quad [33]$$

where $\tau_{r,i}$ is the reference shear stress (N/m^2), $\tau^*_{r,i}$ is the reference dimensionless shear stress, $\rho_{s,i}$ is the density (kg/m^3) and $d_{b,i}$ is the diameter in the B-dimension (m) for the i^{th} tracer.

The ratio between the shear stress exerted on each tracer and their critical thresholds was calculated as $T = \tau^*/\tau^*_{ri}$ and plotted in Figure 48. Tracers that moved over 1.0 m were classified as mobile since the assumed error associated with recovering RFID tracers based on past studies was expected to be approximately 1 m (Chapuis et al., 2014). Under a deterministic interpretation, the dimensionless shear stress ratio can be considered a predicted mobility ratio, where $T < 1$ means that the particle is predicted to remain stationary and $T \geq 1$ means that particle movement is predicted. A unity ratio on the x-axis indicates that the shear stress acting on the particle was equal to its critical threshold. Given the uncertainty on the median reference Shields parameter, an expected error range for the unity line based on an assumed range $0.030 \leq \tau^*_r \leq 0.086$ is shown with the shaded area. The upper and lower bounds of this threshold was obtained from the range of incipient motion thresholds for gravel, as reported by Buffington & Montgomery (1997).

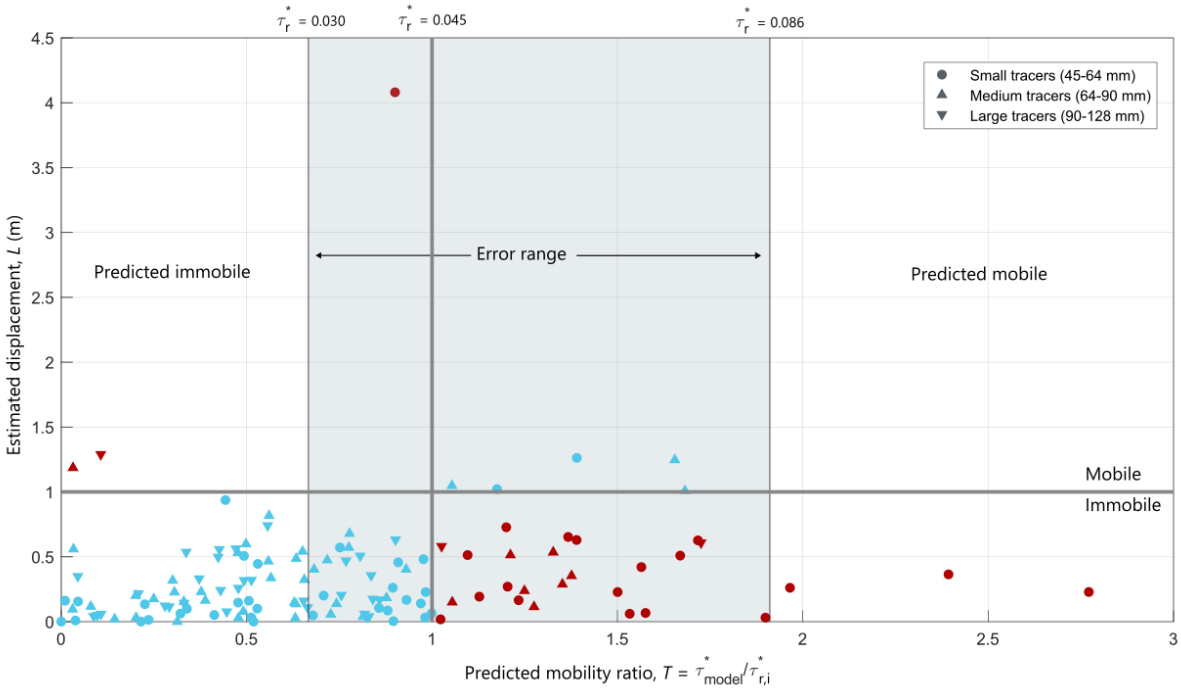


Figure 48 Tracer displacement lengths relative to predicted mobility ratios based on an assumed reference Shields parameter of 0.045. Tracer motion or stability correctly predicted by the model are shown in blue, while those that were incorrectly predicted are shown in red. Expected error of the Shields parameter threshold is shown by the shaded area.

The model performance can vary based on the selected reference Shields parameter. Increasing this value would increase the number of stones predicted to remain immobile. This change would improve the overall number of correct predictions due to the higher number of stones that were immobile, however the model would fail to capture a significant portion of the stones that did show movement. Decreasing the threshold would increase the number of stones predicted to be mobile but would only capture one other moved stone that was already shown to be near the threshold. Varying the reference shear stress to improve apparent model performance requires trade-offs that do not benefit general model predictions, thus 0.045 is adequate to represent incipient motion in the channel.

Overall, the model correctly predicted the mobility status of 77% of the tracers. Five of the eight stones that moved over 1.0 m were accurately predicted to mobilize. One of the stones predicted to be immobile moved over 4 m, but the shear stress acting on it was only slightly under the threshold. The remaining two stones that were incorrectly predicted to remain stationary were both at the left bank of

XS4. These stones appear anomalous, as they were modeled to be under near-zero shear stress, but the discrepancy may have resulted from an inaccurate stone placement. Most of the stones predicted to be stable remained relatively immobile, with strong clustering occurring in the lower left quadrant. 20.3% of the stones were predicted to mobilize but did not move. The breakdown by quadrant is shown in Table 18.

Table 18 Comparison of percentage of predicted and actual mobility

Actual \ Predicted	Predicted immobile	Predicted mobile
Mobile	2.26%	3.76%
Immobile	73.7%	20.3%

4.5 Evaluation of engineering design criteria for spawning gravel placement

4.5.1 Habitat suitability

The flow depth and velocity HSI results for the Chinook spawning (October average) and Coho spawning (November average) flows are shown in Figure 49. The depth HSI is consistently high (0.90-1.0) throughout the reach for both spawning periods. The extent of suitable area is therefore velocity-limited for Chinook, as the areas near the banks and in the upstream half of the channel where velocity is slower is shown to have lower HSI values. Despite peak spawning happening in October, the simulated velocity under the November average flow shows better HSI due to the increased velocity at the higher flow rate. Most of the reach—excluding the near-bank regions—therefore meets the minimal acceptable HSI threshold (0.5) under the November average flow, while the suitable area under the October average flow is limited to downstream half and the upstream thalweg region over the vegetative bed rise. Nonetheless, the October spawning flow was retained for evaluating the design criteria, as it presents a more conservative approach and is supported by historical precedence as the peak Chinook spawning period.

Compared to Chinook which prefer deeper and faster flow, sockeye preferentially spawn in shallower and slower streams. The HSI results for sockeye spawning under the October average are presented in Figure 50, where it is shown that velocity HSI is adequate high through most of the reach. However, the depth HSI for sockeye spawning is consistently 0 throughout the reach, except

for some downstream near-bank areas, indicating that spawning suitability is depth-limited for sockeye in this reach. The gravel placement is thus unlikely to directly improve sockeye spawning in this reach, but the addition of a gravel source in the river system is expected to allow for the creation of future spawning habitat further downstream as the gravel gradually migrates through the system.

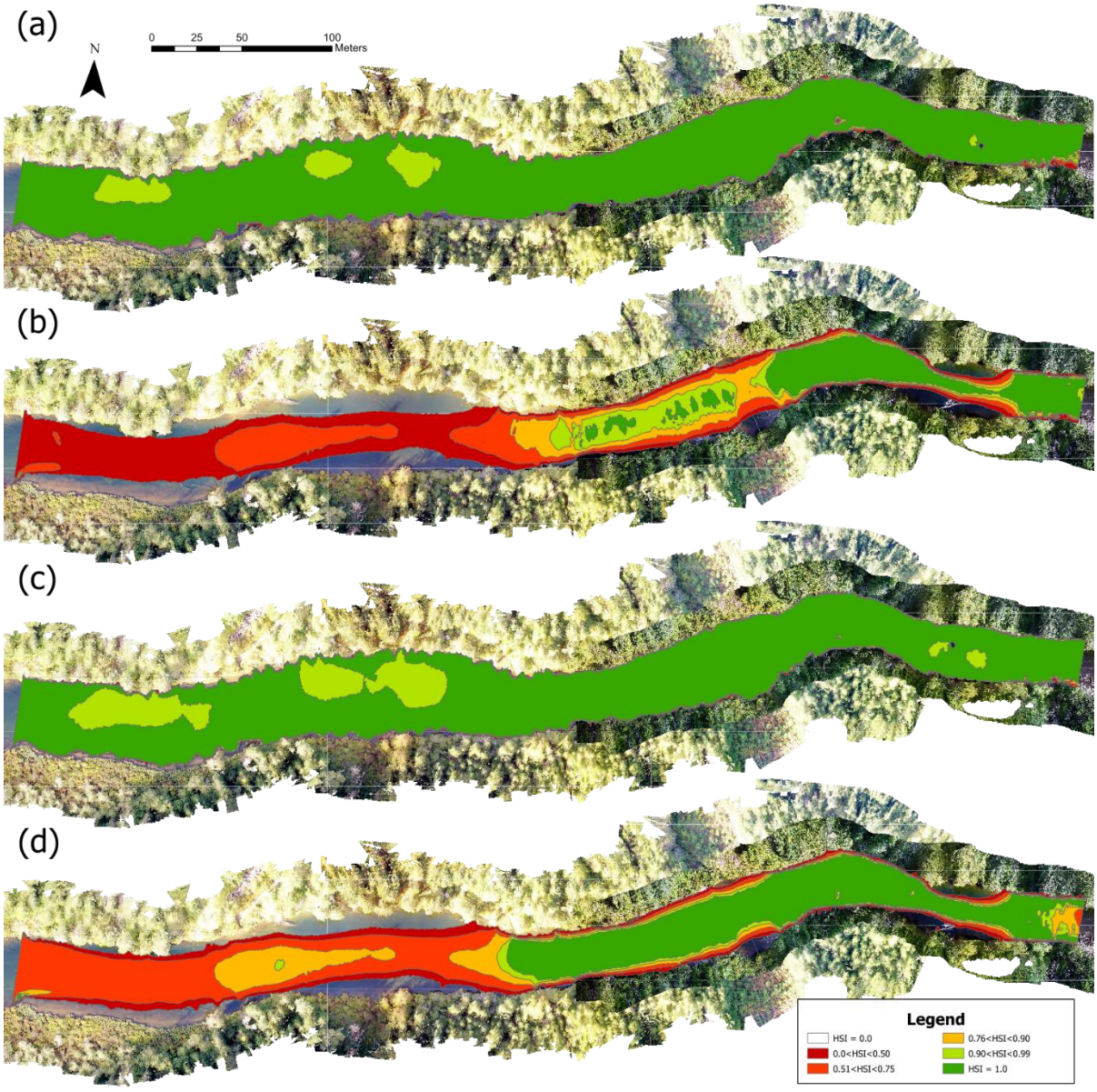


Figure 49 Chinook HSI for (a) depth and (b) velocity under peak Chinook spawning flow (Oct average), and (c) depth and (d) velocity under peak Coho spawning flow (Nov average).

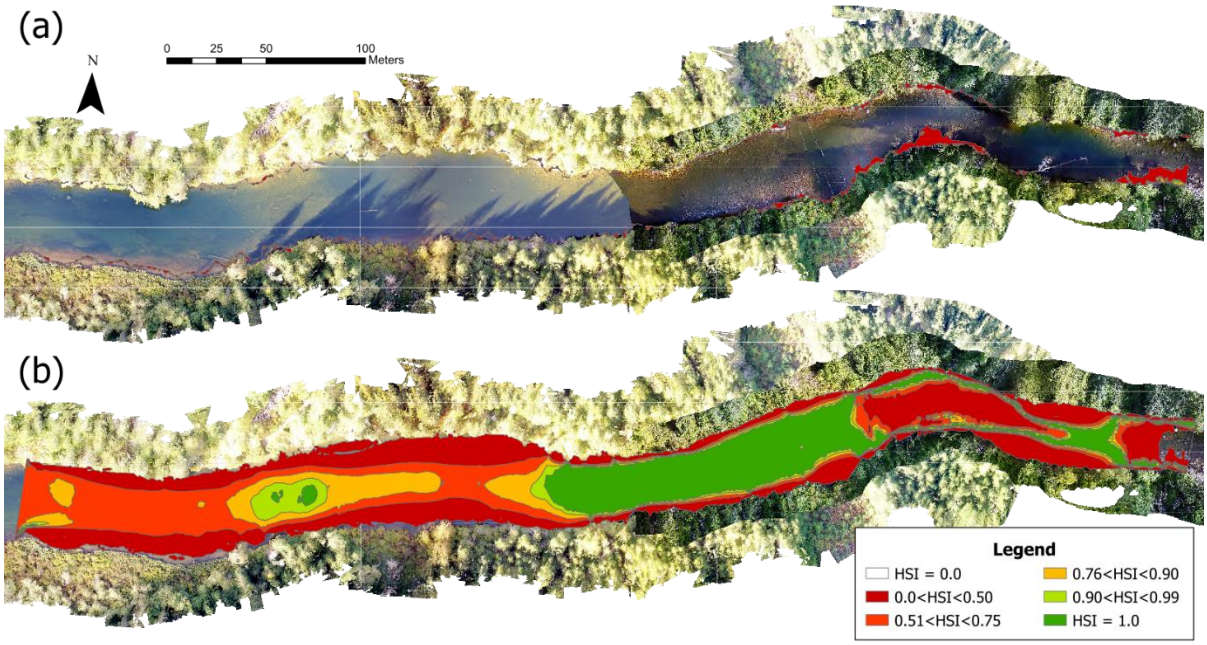


Figure 50 Sockeye HSI for (a) depth and (b) velocity under peak spawning flow (Oct average).

4.5.2 Fines deposition and flushing

The area predicted to be at risk of fines deposition under 7Q10 is shown in Figure 51 (black hatched area), along with the areas where fines are likely to flush under the 400% MAD (pink area).

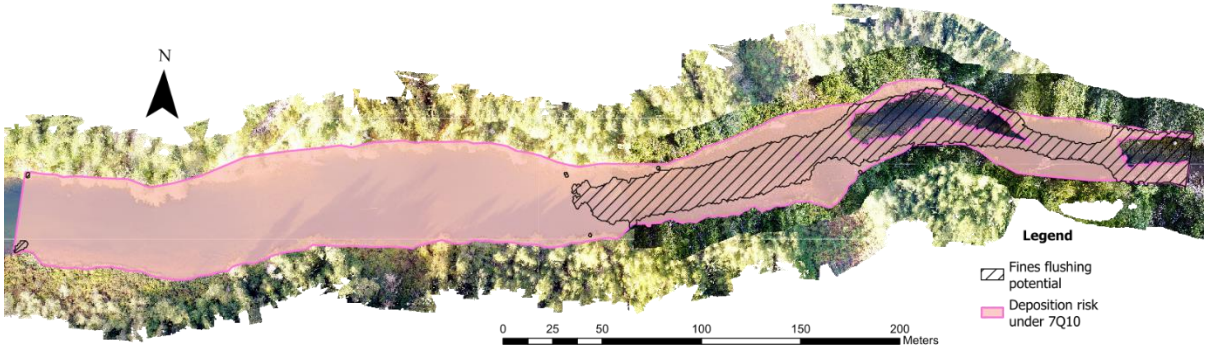


Figure 51 Areas at risk of fines deposition under 7Q10 flow and areas where fines are likely to flush under 400% MAD.

The entire reach is predicted to be at risk for fines deposition at the 7Q10 flow except for the areas of higher velocity around the crest and a small area near the downstream boundary. Inclusion of this design criteria is therefore expected to severely limit the available placement area. Conversely, any

fines that settle through the central strip of the downstream half are likely to remobilize under the flushing flow.

4.5.3 Optimal areas for placement

The comparison of areas fulfilled by each design criterion shown in Figure 52 is used to identify the zone where all criteria are fulfilled (bright orange zone).

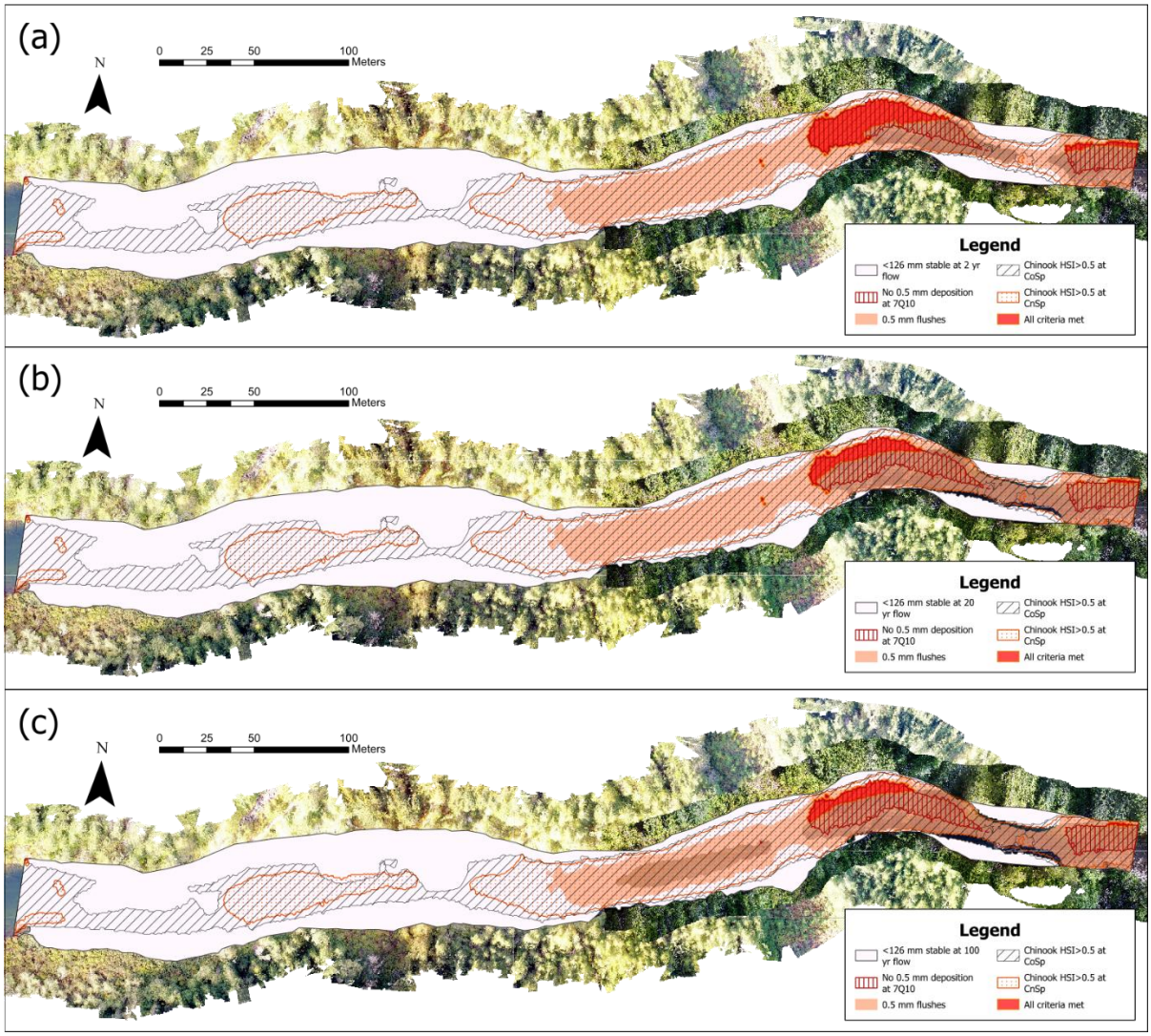


Figure 52 Areas fulfilling all design criteria based on gravel mobility under the (a) 2-year, (b) 20-year and (c) 100-year return flows.

The correlation of shear velocity with flow velocity means that the areas predicted to have high velocity HSI, and good flushing potential is also likely to see greater gravel mobility. Figure 52 indicates that a limited area on the outer section of the bend presents the optimal location for the placement of spawning pads, as it is predicted to have stable 126 mm particles under the design return flows, have adequate spawning habitat suitability, minimal fines deposition risk and a high likelihood for fines flushing. Under progressively higher design flow rates, the extent of the suitable area becomes increasingly smaller, but a 5-10 m wide strip of area remains predicted to fulfill these criteria even under a 100-year return flow.

The fines deposition and flushing criteria were the primary agents restricting the suitable area—without these criteria, the areal extent of the suitable area expands to include the transition section where gravel is shown to be stable in the three return flows and adequate HSI can be achieved under the spawning flows. Given the upstream lake which can presumably act as a sediment trap and reduce the suspended sediment input at the outlet, the importance of fines infiltration in the spawning pads may not be significant enough to warrant its inclusion as a critical design criterion. Figure 53 shows how the extent of optimal area can vary depending on whether fines are considered.

The exclusion of fines deposition as a design criterion considerably expands the apparent suitable area from the bend to the transition section, while the exclusion of both fines deposition and flushing expands this area to small portions of the lake section. The progression in Figure 53 represents a range of risk tolerances regarding fines intrusion as a possible point of failure for the design. Proceeding with any of these options depends on the priorities and the success metrics of the restoration project. While the inclusion of both criteria, as shown in Figure 53a may appear to be a more conservative approach, the placement of a small gravel pad in the identified optimal area is likely not financially or environmentally cost-effective, particularly given the habitat disruption that will occur during the construction process. Conversely, excluding both criteria (Figure 53c) requires accepting a greater risk of low utilization by the salmon due to the poor substrate quality. Thus, excluding only the fines deposition criterion (Figure 53b) likely provides the greatest benefits and best balance between these competing considerations.

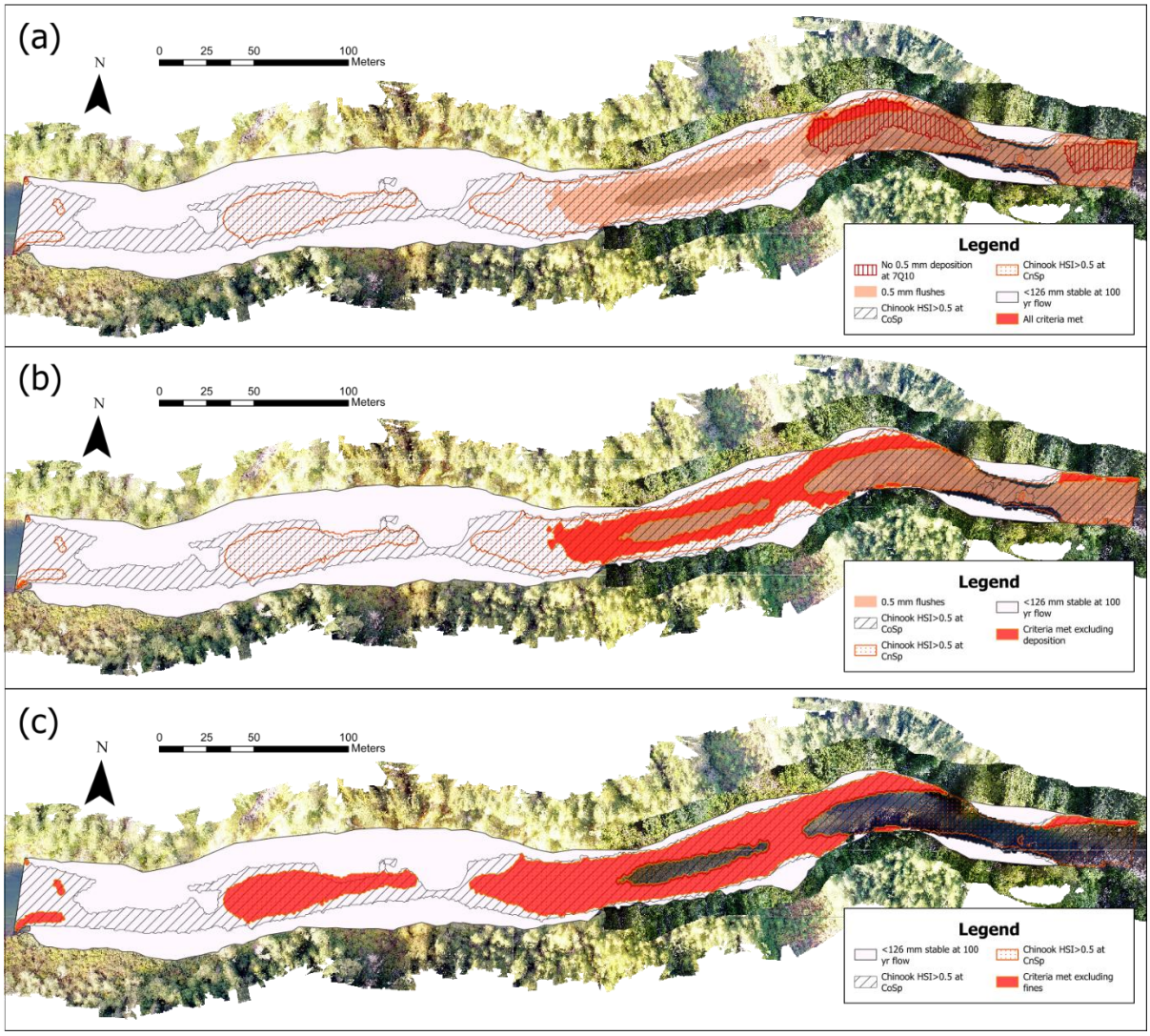


Figure 53 Areas fulfilling the design criteria based on gravel mobility under the 100-year return flow when (a) considering fines deposition and flushing potential, (b) disregarding fines deposition and (c) excluding all consideration of fines.

Chapter 5
Discussion

The goal of this study was to advance the engineering methodology of designing gravel augmentation strategies at lake outlets. In this study, the utility of 2D hydrodynamic models for modeling lake outlet hydraulics and sediment transport was assessed using hydraulic and tracer stone data. The model was then used to identify optimal areas for placing gravel. The primary points of discussion are the limitations and uncertainty of using 2D models to represent lake outlet hydraulics and sediment transport, the significance of the tracer stone results for characterizing sediment transport regimes, and uncertainty in the evaluation of the design criteria. Finally, additional research gaps identified in this study are highlighted.

5.1 Hydraulics

In this study, a 2D hydrodynamic model was used to simulate the steady flow hydraulics at a lake outlet and derive sediment transport predictions from the calculated shear stresses. The assumptions used to develop the model can affect the validity of the conclusions drawn from the model results and govern the level of uncertainty associated with these conclusions.

The coarse bed composition at the site results in a range of relative submergence and roughness conditions throughout the year. Of note, the water depth can be less than boulders and large wood during low flow periods. The variable submergence, adverse slope and wind-driven currents at the water surface are expected to cause wake and dip effects by encouraging secondary currents, thereby resulting in non-standard distributions that may be less suitable for modeling using 2D equations.

5.1.1 Representation of hydraulics in accelerating flow using 2D models

The depth-averaging in 2D models typically assume logarithmic velocity profiles in the fluid layer—such profiles are proven under idealized uniform flow conditions but deviate under certain conditions. As discussed in Section 2.3, the velocity profiles deviate under accelerating flow due to secondary currents which create dip and wake effects. Wake effects can vary depending on the relative roughness and submergence of the channel, but relative roughness and submergence are not spatially constant in lake outlets due to the adverse bed slope and convectively accelerating flow. These parameters are also not temporally constant over moderate time scales due to seasonal variations in

flow rate and stage, which suggests that the accuracy of the 2D model varies between simulations of different discharges. However, engineering analysis typically focuses on predicting points of failure over extreme events where the validity of the model assumptions become increasingly suspect. In this study, the accuracy of model predictions over lower flows (e.g., 7Q10) and higher flows (e.g., 100-year return period) differ drastically, but observation data at these different flows are required to quantify their error.

Furthermore, the importance of the vertical secondary currents that generate the dip phenomenon in accelerating flow is not captured in 2D models, as the velocity is vertically averaged. Consequently, shear stress may be underestimated in areas subject to vertical eddies where the upper flow layer travels in an opposing direction to the lower layer, and the average velocity is near-zero. Under a strong circulatory cell, the shear stress acting on the bed may be higher than would be predicted by a low apparent average velocity if the near-bed velocity is significant.

The extent and direction of the deviations depend on numerous parameters that can be difficult to quantify in field conditions and is further complicated by a poor understanding of the impact of high relative roughness on turbulence characteristics. The depth-averaged velocity calculated by 2D models may not be realistic in accelerating flows, as it is unknown whether the relationship between the shape of the velocity profile and the average velocity holds true in non-idealized scenarios.

5.1.2 Uncertainty on the effect of algal biofilm on hydraulics

Algal biofilm likely affects critical shear stress thresholds for sediment, but the mechanisms and impacts of these impacts depend on grain size. For fines, biofilm has been shown in previous studies to have a biostabilizing effect, but this effect does not necessarily scale up to gravel- or cobble-sized grains. Instead, the effects of algae may instead be linked to impacts to the inner layer of the velocity profile and overall turbulence characteristics due to the reduction in skin friction. These impacts may be exacerbated by a concurrent decrease in drag-based roughness, as the algae appears to cover the entire bed like a cloth, and thereby reduce the bumps and holes from the interstices of the bed surface. There has yet to be any research on how algae and biofilm affects gravel transport or hydraulics, and is a research gap that requires further study.

5.1.3 Uncertainty on the effect of wind-driven currents on hydraulics

The importance of wind-driven currents was more pronounced at this site due to the upstream lake. The wind effects created observable diurnally varying surface velocity, which may also have implications for the validity of steady state flow assumptions for this site. The velocity profile of the flow is likely affected, which can have important implications for the logarithmic velocity profile assumption applied in most hydrodynamic models. The alterations to the velocity profile likely have compounding effects with the deviations caused by accelerating flow, as discussed in Section 5.1.1.

TELEMAC-2D allows for the consideration of wind loading on flow, but such considerations are rarely applied for 2D fluvial models. The wind loading likely also varies seasonally and may be a governing factor in the hydraulics during relatively shallow flows, which may contribute to the poor model performance at low flows. To obtain a more accurate representation of the fluvial hydraulics, the numerical model should ideally be formulated in conjunction with a coupled coastal model of the lake. The wind loading on the lake would be formulated with historical wind direction and magnitude records from a nearby weather station, and the lake outflow would be used to define the boundary condition of the fluvial hydraulic model. Unfortunately, such a model would require detailed bathymetry data of the lake, which would be cost-prohibitive for a project of this scale.

5.2 Sediment transport

5.2.1 Limitations in the classic shear velocity calculation method

The non-uniformity of flow presents complications in assumptions on the best method of calculating shear stress from depth-averaged values in these conditions. Modifications were required to some of the existing 3D methods discussed in Section 2.3, but little research has been done on how these alterations translate to 2D applications. The classic method for calculating shear velocity in 2D hydrodynamic models relies on the product of a skin friction value and the modeled velocity at a node. This method is derived based on a force balance under uniform flow, where the sum of forces would equal zero. Evidently, such an assumption is invalid in non-uniform flow, hence the degree of confidence in obtaining bed shear stress and bedload transport rate is uncertain.

Another barrier for the use of this method for applications related to sediment transport is a flawed circular analysis in 2D models. The modeled hydraulics and flow are calibrated using the skin friction coefficient, and the calibration parameter is then directly used to obtain shear stress and sediment

transport predictions. Due to the simplifying assumptions of 2D models, the calibrated friction value is often artificially inflated, since the skin friction is the sole resistive force in the model formulation and must therefore overcompensate for other types of drag that are not well-captured in these models.

Furthermore, local hydraulic conditions are typically more important for predicting sediment motion than reach-averaged values. Consequently, sediment transport models employing the friction method (which tends to yield continuous shear stress gradients) may provide limited spatial precision in their predictions. The limitations related to this method lead us to question its utility to this application where spatial gradients in the bed condition and flow parameters are critical for model results. However, the results obtained using this method are interpreted as a deterministic predictor for grain mobility in 2D models. Alternative methods would be preferred, but the lack of feasible alternatives has resulted in the continued widespread use of this approach despite its flaws. Ideally, a more fundamental framework should be adopted, wherein the flow resistance parameter which is used for calibration is not then directly applied to transport predictions.

5.2.2 Proposed method for calculating shear velocity

The proposed SVE momentum method shows promise as a novel approach of calculating shear stress from 2D models, as it does not directly incorporate skin friction as a parameter in the equation and is instead reliant on modeled hydraulic parameters. While the use of the SVE momentum equation is not new, the proposed separation of the depth based on the position of the fluid layer above or below the crest of the crest is novel in its unique relevance to lake outlets.

Unfortunately, this method is still limited by its high sensitivity to bathymetry inputs which creates local shear stress peaks. This sensitivity precludes the use of this approach as a deterministic predictor for grain mobility when high-quality bathymetry data is not available. With the progressive advances in collecting high-resolution bathymetry through RPAS and SfM methods, the uncertainty associated the SVE momentum method is decreased. The combination of RPAS-SfM methods with the momentum approach shows promise as a viable alternative to the friction method, especially in reaches with spatially varying roughness. Further validation work using a physical or 3D model is still required to verify that the accuracy of this method before it can be used in any practical application. However, this method may be suitable for a developing stochastic approach to identify the fraction of area within a region of interest that might be expected to mobilize.

5.2.3 Sensitivity to critical shear stress thresholds

The calculation of the critical shear stress threshold for each particle size classes depends on the selection of a site-appropriate reference Shields parameter for the median grain size. Many of the studies on incipient motion thresholds reviewed by Buffington & Montgomery (1997) were conducted for channels with low relative roughness (≤ 0.2), which may affect their utility in channels with high relative roughness and partial or low submergence.

The adverse bed slope through most of the reach and the high armouring in the bed are expected to result in a higher critical shear stress threshold for gravel than literature values. However, these effects may be likely offset by the presence of algae and small-scale spawning activity in the reach.

Although the selected reference Shields parameter in this study appeared to be relatively representative from the direct comparison of the modeled and actual shear stresses, the lack of significant tracer movements during the study year limits this conclusion. Conversely, the comparison of the tracer stone results with the general modeled mobility patterns appeared to indicate an overprediction of mobility by the numerical model. The results support the selection of a higher reference Shields parameter and suggest that the slope or biofilm likely dominate in the competition between the mobility-promoting and mobility-impeding factors. This parameter may be subject to change post-construction due to the time required for the biofilm layer to redevelop on the newly placed gravel and the bed disturbances from increased spawning activity.

5.2.4 Size-dependency for critical shear stress thresholds

The critical shear threshold depends on the particle size being evaluated and thus on the assumptions of the correct representative particle size for the size class. For a given Shields parameter, the absolute value of the shear threshold in N/m^2 is directly proportional to the particle size in m based on Equation [25]. However, sediment sizes are commonly represented and classified based on a logarithmic scale with a base value of 2 (also commonly referred to as the Wentworth phi scale). The variability of the critical shear stress within each category is therefore not constant, as the shear stress thresholds for the median and the maximum grain size within the size class can differ by an order of magnitude for gravels but be virtually the same for sands. The mobility of the median of each size class does not necessarily represent the actual criteria of movement but may be useful only to predict general trends on which areas may be subject to relatively more scour. An example is shown in Table

19, where the difference critical shear stresses for the median and maximum grain sizes in two size classes are compared for a critical Shields parameter of 0.045.

Table 19 Example of the difference in scales for calculated shear stress for different size classes

Size class	Grain size		Shear stress (N/m^2)	
	(ϕ)	(mm)	Critical	Difference
Coarse sand	-0.5	1.41	1.03	0.43
	-1	2.00	1.46	
Gravel	-5.5	45.25	32.96	13.65
	-6	64.00	46.62	

Evaluating gravel mobility for size classes can yield vastly different results depending on the selected representative grain size. For example, the minimum and maximum critical shear stress thresholds for the 100-150 mm size class varies by 30 N/m^2. A comparison of the predicted size class mobility patterns using the median and maximum sizes in each category is shown in Figure 54.

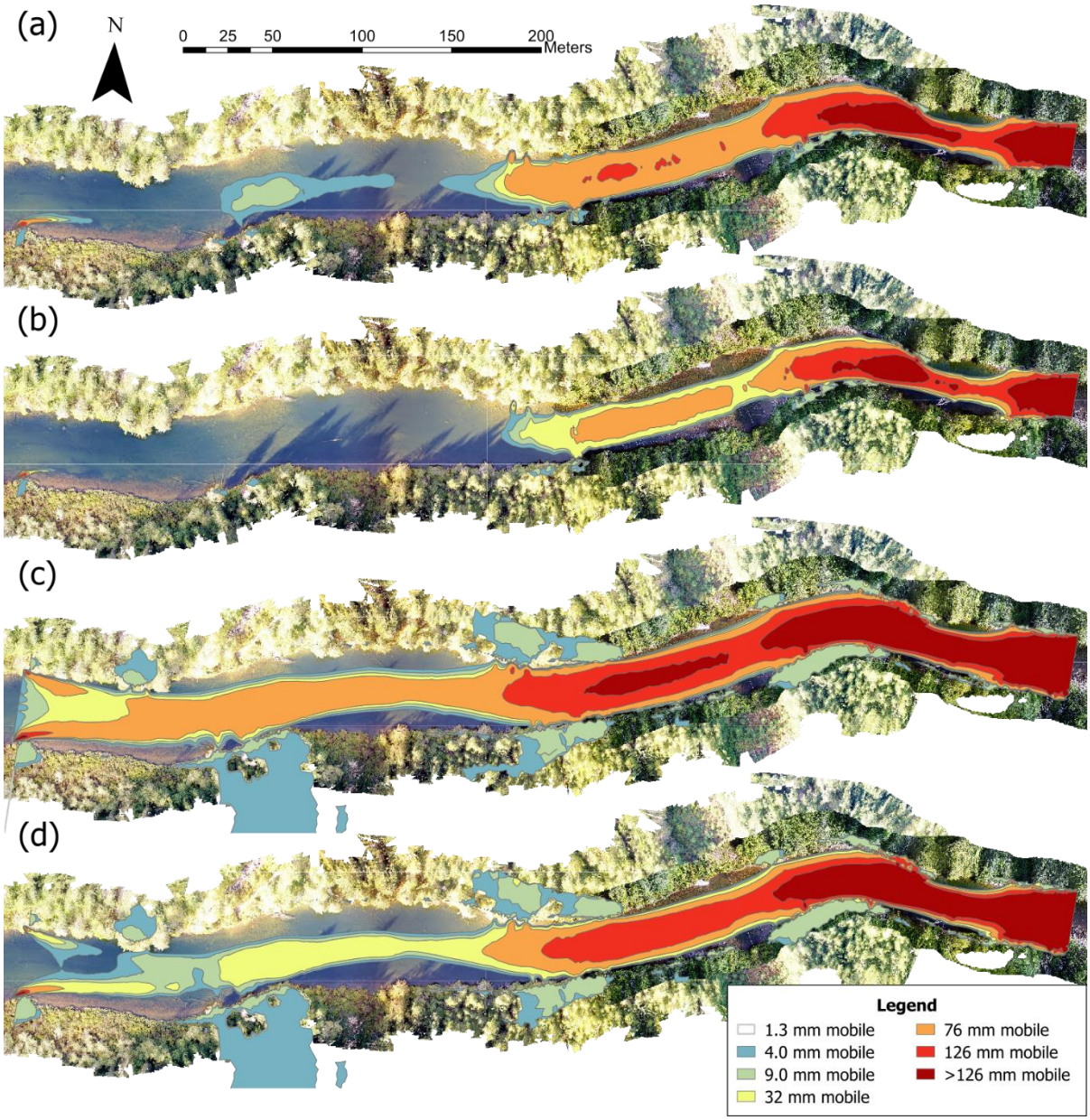


Figure 54 Predicted mobility patterns for the (a, b) 2-year and the (c, d) 100-year return flows using the median and maximum grain sizes in each size class.

From the figure, the use of the median as the representative size yields higher mobility predictions than the maximum. The tracer results showed that the model predictions obtained using the median particle sizes overpredicted mobility. Conversely, the use of the maximum size risks underpredicting scour and is less conservative. The differences in the figure highlight the importance of using actual

particle sizes when evaluating incipient motion, however this is often not feasible in practice. The selection of a different representative size—such as the D_{60} or D_{84} of each size class—may yield improved predictions but cannot yet be determined without further tracer data.

5.2.5 Implications for engineering applications

This study employed a static approach of estimating sediment transport, where modeled shear stresses were converted directly to mobility maps. Another common approach is to dynamically couple the hydrodynamic model with a sediment transport module. Coupled models apply sediment transport equations to predict areas of erosion and deposition and update the topography at each time step. With such approaches, errors resulting from unrealistic shear stress calculations risks compounding and leading to incorrect conclusions on geomorphic responses. Regardless of approach, the factors affecting the uncertainty of the sediment transport models can result in vast differences in predicted areas of stability, erosion, and deposition. Consequently, conclusions on bed stability drawn from 2D sediment transport models must be approached with caution.

The intended outcomes of a project should be evaluated while considering the balance of opposing criteria. Adopting a conservative design based on a single factor can lead to failure on other factors. Despite the uncertainty and risk associated with interpreting the sediment transport model results, overdesigning for stability by adopting an excessively conservative approach on the threshold of movement results in a structural design that is likely to fail in forming usable spawning habitat.

5.3 Tracer stones

5.3.1 Partial tracer mobility

The high number of immobile stones over a range of mobility ratios reveal that particles can remain stable under a wide range of shear stresses and that entrainment depends on more than critical shear stress. The density of the points in the lower right quadrant (i.e., predicted mobile/actual immobile) of Figure 48 decreases with increasing shear stress, with most of these points remaining in the $1 \leq T \leq 1.5$ range. This observation aligns with the understanding that stones are less likely to remain stationary with increasing shear stress.

The results Figure 48 confirm the importance of distinguishing between partial and full mobilization, which is determined based on whether the proportion of mobilized grains in a given size

fraction exceeds its proportion on the bed surface (Wilcock & McArdell, 1993). The mobility of three tracers with $T < 1$ shows that partial mobility occurs even below the reference entrainment threshold, while immobility of stones with $T > 1$ indicates that full mobility is not attained under this flow rate. The likelihood of a particle entraining at a higher or lower shear stress than its reference value depends on the specific mechanics related to its density, shape, volume, position, packing with adjacent grains, hydraulic variables, and their interactions with each other. These parameters are evidently impractical to model at such a fine scale and so would be likely better represented by a stochastic model.

5.3.2 Cumulative transport fractions

The fraction of particles above a given critical shear stress threshold is described by:

$$F(T) = \frac{n(T)}{n_T} \quad [34]$$

where $n(T)$ is the number of tracer stones above the mobility ratio T and n_T is the total number of tracers. Defining F based on immobile tracers only and plotting against the mobility ratio reveals a negative-slope logistic-type relationship in the form:

$$F(T) = \frac{a_F}{1 + \exp\left(b_F(T - c_F)\right)^{d_F}} \quad [35]$$

where a_F, b_F, c_F and d_F are curve-fitting parameters. From Figure 55, 50th percentile value of the immobile and mobile stones occur at approximately $T = 0.62$ and $T = 1.24$, respectively.

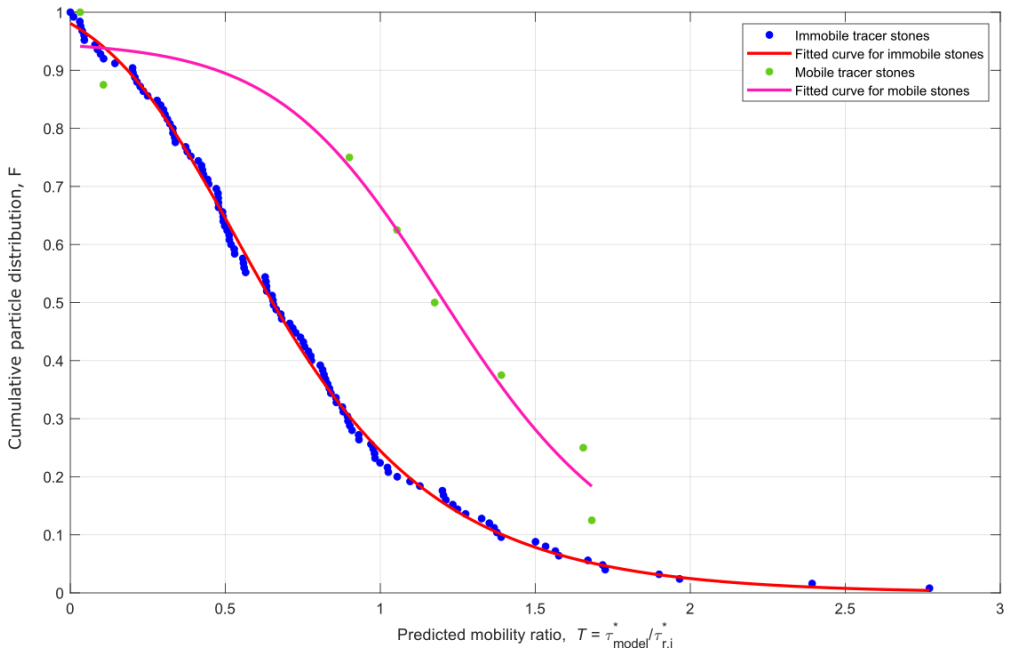


Figure 55 Distribution of mobile and immobile tracers with mobility ratios.

Figure 55 shows the distribution of shear stresses on the mobile and immobile particles during a single flood event. The slope at the inflection points for the two curves are similar but deviate at low and high T-values. A steeper slope is observed at low T for the immobile curve than the mobile curve, thus suggesting a higher concentration of immobile stones which agrees with the intuitive understanding that grains are less likely to be mobile at low T. Conversely, the opposite is observed at high T, where a steeper slope is observed for the mobile curve despite being truncated due to the lack of data points. The logistic distribution aligns with previous findings by Hodge & Buechel (2022) who found that the distribution of critical shear stress in individual geomorphological units (e.g., pool, riffle, etc.) also follows a positive-sloped S-shaped pattern. A similar plot for a flood of a different magnitude is expected to follow a similar shape but with different inflection points.

The figure also highlights the limitations of the current mobility model based on critical incipient motion thresholds. Under the deterministic mobility method for evaluating sediment movement, the mobility ratio would be restricted to $0 \leq T < 1$, since $T \geq 1$ represents the condition for movement. The median values still agree with this approach, showing that the deterministic method can predict mobility in the reach on average. However, the range of T-values in Figure 55 show that particles can remain immobile even for shear stresses up to 2.8 times greater than the reach-averaged reference

value. This value is slightly higher than the $1.8 < T < 2.4$ full mobilization thresholds for the full channel that were observed by Wilcock & McArdell (1993). Nonetheless, the comparison of these thresholds with the curves in Figure 55 clearly show that the channel is in a partial mobility condition.

Interestingly, when isolating the points above $T = 1$ by setting n_T to the number of immobile tracers above $T = 1$, the cumulative frequency of stones in this quadrant plotted against the mobility ratio yields a negative exponential relationship (Figure 56). The relationship is given by:

$$F_{im}(T|T \geq 1) = P_{im}e^{-\lambda_{im}T} \quad [36]$$

where P_{im} and λ_{im} are curve-fitting coefficients.

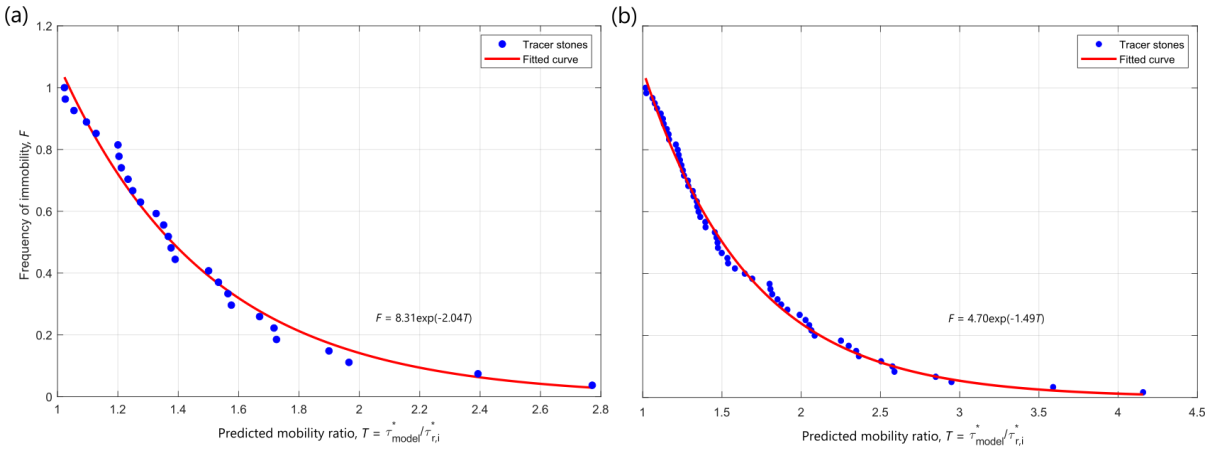


Figure 56 Fraction of tracers that were immobile above the predicted mobility threshold based on assumed reference Shields parameters of (a) 0.045 and (b) 0.030.

For a reference Shields parameter of 0.045, coefficients of $P = 8.31$ and $\lambda = 2.04$ had the best fit with the data (Figure 56a) with $R^2 = 0.98$. Conversely, using $\tau_r^* = 0.030$ yielded $P = 4.70$, $\lambda = 1.49$ and $R^2 = 0.99$ (Figure 56b). These high R^2 values indicate that the strong exponential relationship exists irrespective of the selected reference Shields parameter, but that the coefficients are threshold-dependent. The strong trends support the existence of a stochastic relation between shear stress and static particles that can be represented by an exponential distribution.

This mobility model follows the work of Arnaud et al. (2023) who observed the importance of including stochastic relationships when modeling the dispersion of sediment tracer clouds. Although exponential distributions of particle travel distances have previously been linked with flow variables (e.g., Hassan et al., 2013; Papangelakis et al., 2022; Papangelakis & Hassan, 2016), further work is

required to establish similar probabilistic link between incipient motion and flow variables. One study comparing tracer stones with a 2D numerical model attempted to relate mobility probability and flow velocity using a logistic regression on binary points of observed mobility (i.e., where a mobile stone would be represented by a value of 1 and an immobile stone by 0) (Chardon et al., 2021). Despite the logistic curve-fitting, the trends between mobility probability and flow velocity in Chardon et al. (2021) appeared to follow the shape of a vertically flipped exponential curve in the form:

$$F_m(V) = 1 - P_m e^{-\lambda_m V} \quad [37]$$

where $F_m(T)$ is the probability of mobility, and P_m and λ_m are curve-fitting coefficients. As T is a function of shear stress which is itself a function of flow velocity, it follows that Equation [36], which relates an immobility fraction with shear stress, and Equation [37], which relates a mobility fraction with flow velocity, are flipped relationships.

Unfortunately, the regression analysis completed by Chardon et al. (2021) cannot be replicated for this study due to the relatively few tracer movements and lack of full mobilization under the observed peak flow. These results highlight the benefit of using 2D hydrodynamic models for analysing tracer data, especially if data can be obtained for multiple events of varying magnitudes. The comparison of tracer movements and recreations of flood events using 2D models provide the opportunity to relate sediment responses to hydraulic patterns and describe bed responses to shear stress. Further mobility analysis would be facilitated with additional years of data under higher peak flows.

5.3.3 Tracer stone mobility definition

A primary limitation of the tracer stone study was the equipment failure on WFT1 that resulted in a lack of measurement of the initial seeded locations of the tracers. Tracer mobility at each transect was instead estimated by drawing an approximate straight line connecting the stones closest to the banks to represent the transect and calculating the perpendicular distance between the found tracers and the line. The locations of some of the tracers were mapped upstream of the line; this discrepancy may be due to error during the placement or from the total station survey of the found tracers. The placement during WFT1 and the survey during WFT2 were completed by swimmers who were treading water against the river current to remain as stationary as possible, thus error up to at least 0.5 m is expected.

As the perpendicular distance was used to evaluate movement and lateral movements were not considered, it is likely that actual travel distances were greater than calculated, especially if the tracers

had displaced in a diagonal direction. For longer travel distances, such as those recorded by MacVicar & Papangelakis (2022), the transverse displacement is inconsequential but for the limited mobility observed at this site, the transverse movements were at times larger than the streamwise motion. However, as the primary design outcome is to minimize gravel exported from the reach and the tracer movements were not significant, the exact determination of travel distance was not a major concern.

5.3.4 Tracer stone monitoring for restoration projects

The use of tracer stones to monitor restoration projects is a relatively new endeavour, much less for a priori analysis of restoration efforts, but it presents an opportunity to evaluate designs using a relatively short-term and cost-effective method. Many monitoring programs employ DoD methods or reach-scale erosion assessments to assess areas of aggradation or degradation, however such methods can only be implemented after large-scale transport. These methods are unable to quantify partial transport and fail to verify relationships between the flow and sediment transport regimes. Conversely, tracer stones can be tracked frequently and intermittently through a wide range of floods, therefore requiring a shorter monitoring period before scour risk can be identified. Restoration outcomes can therefore be more readily attained as an earlier anticipation of failure provides opportunity for more effective mitigation with adaptive management strategies.

The validation of sediment transport models using sediment tracers is rarely completed, especially in field sites where non-uniform flow is present. The calculation of shear stress—on which sediment transport predictions are based—is uncertain due to the uncertainty surrounding turbulence and velocity profiles in these environments. Sediment tracers can be useful to assess whether assumptions in the sediment transport model (e.g., related to surficial GSD, critical shear stress thresholds, shear stress calculations) are able to adequately represent actual transport patterns in the field without requiring significant topographic changes during the study period (as would be required for DoD methods). Sediment tracers are also useful as a validation tool, as mobility assessments can be conducted on a clast-by-clast basis (Section 4.4.4), which is more accurate than the generalized method presented in Section 4.4.3. Particle-based tracking of mobility also allows for the comparison of sediment transport predictions methods, as was done by Arnaud et al. (2023). The utility of comparing tracer data with 2D or 3D hydrodynamic models makes this approach a promising and increasingly popular in gravel bed research (Liébault et al., 2024).

5.4 Uncertainty in the design evaluation

5.4.1 Consideration of fines

In an undisturbed watershed, it is likely reasonable to exclude the consideration of fines in the design evaluation. However, the presence of fine sediment input from logging (such as at the west delta formation near the mouth of the outlet described in Section 4.1) creates considerable uncertainty in the true sediment load, and therefore in the evaluation of deposition risk. It is important to note that fines deposition is not always an issue and is only of concern when there is risk of clogging in the gravel interstices while the eggs are buried in their redds.

The risk of fines deposition was evaluated under a steady low flow since deposition was evaluated based on a comparison of the flow and settling velocities. However, the sediment load from the lake is likely positively related to discharge, as higher flows would be required to transport fines to the outlet or to flush fines from lacustrine sources. Evaluation of the risk of deposition should therefore be accompanied by a knowledge of the local sediment rating curve since deposition cannot happen without sediment load. However, these rating curves can be difficult to quantify due to hysteretic effects between discharge and sediment load. Sediment deposition is more likely to occur on as flow decelerates on the falling limb of a flood rather than an equivalent flow rate on the rising limb.

The knowledge gap on sediment load hysteresis creates uncertainty on the areas identified to be at risk of deposition. This uncertainty is compounded by the uncertainty of accuracy of the hydrodynamic model at low flows, particularly given the poor calibration results at the MeFT flow. The model performance is expected to deteriorate further under increasingly low flows; the extent of deterioration is especially uncertain for the 7Q10 scenario which is two orders of magnitude smaller than the MeFT flow.

These geophysical considerations of uncertainty surrounding the behaviour of fine sediment at the lake outlet become further complicated when including biological elements like algal growth and biostablization. The accumulation of fines may be affected by algae which can increase sediment deposition by limiting the resuspension of deposited material. The area at risk of deposition may therefore be larger than predicted, while the area where flushing can occur may be smaller. The algae may create a cover blocking the fines from infiltrating to the eggs but may also contribute to clogging itself. The interactions between biofilm, fine sediment and hyporheic flow is complex and not well-understood. Measures of dissolved oxygen concentrations in the hyporheic flow may provide better

estimates on the impacts of clogging on the gravel interstices, but such measurements can be difficult to conduct in the field.

The uncertainties on the accuracy of the hydrodynamic model at low flows, the suspended solid load under low flows and algal effects on fines support the exclusion of fines deposition risk as a key design criterion for gravel augmentation at lake outlets. These factors are compounded by the low likelihood for deposition to occur under low flow due to the presumed lack of sediment load under these conditions. Although deposition is more likely to occur on the falling limbs of floods, there is still a research gap on how this hysteresis translates to a wide range of environments. This gap therefore precludes the utility of modeling unsteady flows, as it is not known which equations and coefficients would be most appropriate to apply at this site. Visual observations in the field can serve to justify decisions on the inclusion or exclusion of fines as a design criterion, but such decisions should be supported with turbidity or total suspended solids (TSS) data. If continuous TSS monitoring is not possible, the collection of TSS data should be conducted on the falling limb of a hydrograph to best characterize deposition risk.

5.4.2 Implications for gravel augmentation at lake outlets

Gravel augmentation is a procedure that is inherently fraught with uncertainty. Hydrodynamic modelling is often used as a predictive tool to assess the hydraulic and geomorphic response of the channel, but outcomes produced by such models rely on imperfect assumptions and formulations. The lack of standards and a systematic framework for gravel augmentation design necessitates judgement on best practices and tolerances for design criterion thresholds which can at times appear arbitrary.

Recognizing these limitations, it is imperative to remain conservative where possible, however these efforts are counterpointed by the need to balance demands from competing design requirements. These design requirements may stem from financial, ecological, geographic, or social constraints—like any engineering design, understanding these constraints is critical to achieving success, in whichever way success is defined. For lake outlets, defining a successful restoration as one that is stable for decades can result in a design that exposes the installed spawning pads to threats of fines infilling or low utilization due to unsuitable hydraulic conditions. Remaining excessively conservative when designing for stability exacerbates exposure of the spawning pad to these other risks. Selecting the level to which the risk of fines infilling is considered or the thresholds at which a design criterion is considered fulfilled can drastically change analysis results—a balance must

therefore be struck between remaining conservative for the primary design criterion—however this is defined—without overly compromising the outcomes of the other criteria. This balance, depicted conceptually in Figure 57, must be maintained in consideration of site-specific elements that can cause the design to tend towards being more static or mobile and is achieved by varying design parameters such as the location along the stream and GSD of the gravel placement mixture. Prioritizing structural stability aligns with the form-based restoration ideology, but overdesigning in this way can lead the design to fail through interstitial clogging or low utilization by the target fish species, thereby contradicting with the original intentions of the restoration project. Conversely, designing with the intent for gravel to mobilize recognizes that sediment transport is a natural fluvial process, and thus follows a more process-based approach. However, designing for mobility without any constraints may risk excessive erosion and may thus fail to have a financially justifiable lifespan within the target reach. Ideally, the placed gravel should be continuously maintained by refreshing the gravel supply when necessary. Unfortunately, the feasibility of this adaptive management strategy is heavily project- and funding-dependent, thus a balance optimized for financial effectiveness is not always preferred ecologically.

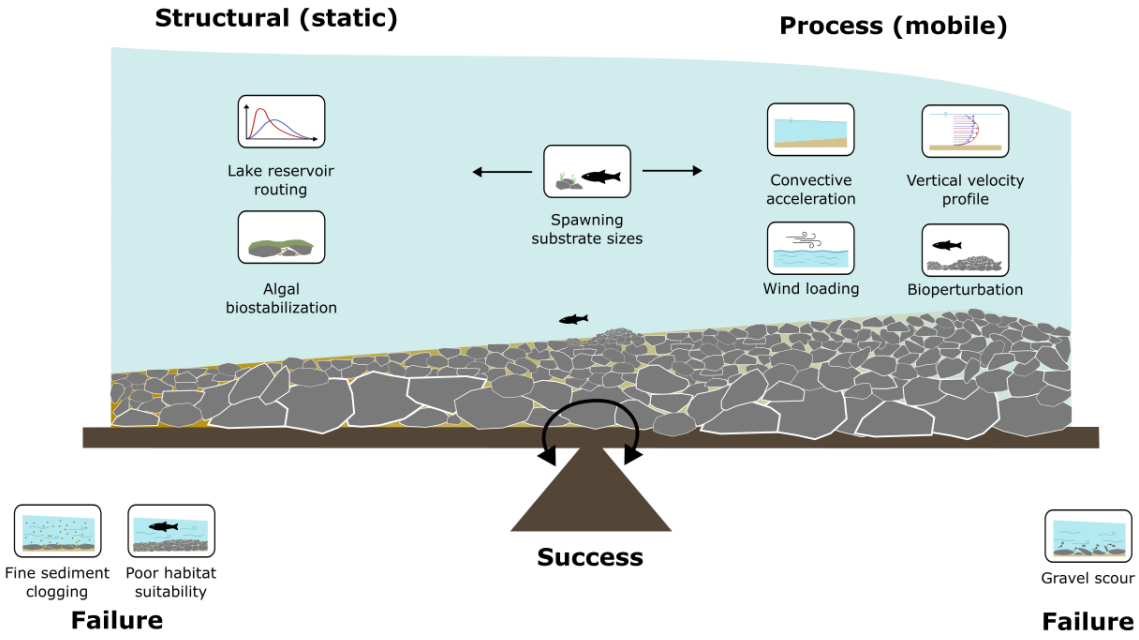


Figure 57 Achieving balance for gravel augmentation at a lake outlet.

As highlighted by Papangelakis et al. (2022) and Papangelakis & MacVicar (2020), designing restoration strategies exclusively for stability ignores the inherently mobile and dynamic nature of gravel-bed rivers. To properly restore sediment fluxes, gravel augmentation design should strive to restore the sediment transport regime to allow the river to recreate its natural morphologies and re-establish fish habitat instead of creating static bedforms. Sediment should therefore be capable of mobilizing short distances (e.g., the length of one channel width) without fully exporting from the reach of interest. A more appropriate design criteria for evaluating sediment transport may be to set a desired mean annual grain velocity. The design life of the gravel placement would then depend on the length of time it takes for sediment to travel outside of the target restoration site. Designing to restore morphological processes is more likely to likewise achieve biological targets related to spawning. However, employing this strategy assumes mobility and therefore requires periodic replenishment of the gravel supply, which is a considerable barrier for funding-limited projects.

It may be therefore more conservative to design for wider range of scenarios by placing gravel over a larger area than the optimal area identified in the analysis. Different areas of the placed gravel would have varying levels of risk to each of the three points of failure, thereby increasing the risk tolerance of the entire design. Following the seesaw analogy, this strategy would be equivalent to spreading a larger and flatter weight or multiple counterweights along the length of the beam rather than one weight at a single point. Doing so would increase the likelihood of balancing the beam, while also providing additional parameters to complete fine adjustments in such a way that decreases the sensitivity to failure of each design choice.

5.5 Research gaps for further study

Through this study, it was apparent that further research in understanding the applicability of fundamental hydraulics and sediment transport assumptions is needed for lake outlet settings. The impact of epilithic biofilm, accelerating flow, wind loading, and high relative roughness on velocity profiles and turbulence characteristics may have previously been studied to various degrees in isolation, but there is a knowledge gap on how these effects interact with each other in a single setting. Of these elements, the most research has been conducted on accelerating flow due to its relevance to pool-riffle morphologies, but even these studies have largely been conducted in idealized laboratory settings with a limited range in bed slope ranges and width-depth ratios.

There is an opportunity for further research to be conducted to model lake outlet morphologies in using physical or 3D modelling. The development of a 3D model would require collecting better field characterization data including detailed bathymetry, a survey of high water marks and calibration data. Conversely, a physical model can be used to model adverse-slope accelerating flows, while isolating the effects of variable width (narrowing from upstream to downstream), GSD gradients (coarsening from upstream to downstream), redd-shaped bedforms and biofilm. Understanding these impacts can lead to better characterization of velocity profiles, turbulence, shear stress and sediment transport in lake outlets, and elucidate the applicability of 2D models in these environments.

Collecting additional years of tracer stone data is expected to reduce the uncertainty of the analysis, especially as the freshet flow in the upcoming year is expected to be higher than last year and provide clearer mobility patterns. These tracer results can also be further analysed with a long-term hydrologic model to simulate continuous discharges over a design period. The discharge provides a basis for calculating excess stream power which can in turn be related to particle travel distances using the relationship proposed by Papangelakis et al. (2022). This approach can be combined with multi-dimensional hydraulic models to identify active areas of transport and aid the advancement of a stochastic approach to modeling sediment transport.

Finally, a post-construction tracer and infilling monitoring study to evaluate the success of the design and validate model results would be useful to improve the methods and assumptions employed in the pre-construction analysis and serve to inform adaptive management strategies at this site.

Chapter 6
Conclusions

In this study, analysis and modelling was completed to assess the design criteria of a gravel augmentation project at a lake outlet. The study was intended to further research on designing salmon spawning habitat restorations at lake outlets and provide support to a current restoration project undertaken by the industry partner, Ecofish Research Ltd., and their clients NSWS and MMFN. The study objectives were to (1) specify a gravel spawning pad placement strategy for Chinook and sockeye salmon in the Muchalat Lake outlet, (2) validate the strategy using sediment tracers in the pre-construction condition, and (3) assess the viability of using two-dimensional models to model lake outlet hydraulics. The results of this thesis highlighted the importance of assessing restoration priorities and identifying clear outcomes to achieve a balance between competing design criteria.

6.1 Objective 3: Application of 2D models for lake outlets

The 2D hydrodynamic model developed using TELEMAC-2D was found to accurately represent the measured velocities at the highest measured discharge (123 m^3/s) but showed limited ability to reproduce the velocities at the two lower measured flows (10.2 m^3/s and 1.17 m^3/s). The RMSE of the modeled velocities were similar across the three calibration scenarios, indicating that the difference in model performance between the different discharges was likely partially attributed to inherent model inaccuracies at low flows. Other sources of error stem from the poor ADCP data quality at shallow flows and the inability of the model to capture flows under high relative roughness.

The sediment transport predictions using the initial model that was calibrated with spatially varying friction zones showed discontinuous mobility patterns that resulted as an artefact of the prescribed friction zones. These results reveal that 2D models rely on a circular reasoning to obtain sediment transport predictions, wherein the hydrodynamic model is calibrated with friction, which is then a direct dependent variable for shear stress. A 2D interpretation of the Saint-Venant momentum conservation equation that is independent of friction was proposed as a novel method of calculating shear stress. This formulation is uniquely applicable to lake outlets, as it separates the layers of flows based on the relative height to a crest. This method requires additional refining in the post-processing steps to render the results useful for analysis. The issue in the shear stress calculations was rectified

by extending the downstream boundary of the model to the Solinst gauge, which allowed for greater certainty on the boundary conditions and the use of a constant roughness value throughout the reach.

The overall results from this study highlight the importance of post-construction monitoring of stability and fines to validate the a priori analysis and implement adaptive management strategies. The future steps for this study are the continuing of the tracer monitoring for at least one additional study year, and the development of a 3D or physical model to verify the accuracy of the 2D model.

6.2 Objective 2: Sediment tracer validation

The results from the tracer study suggested that the class-based mobility patterns produced by the sediment transport model overpredicted actual movements. However, a clast-based direct comparison using the measured particle characteristics showed improved alignment between the model predictions and observed movements, and indicated that the model agreed with the tracer results on average, but failed to predict the mobility of individual grains. The relative lack of tracer movements indicate that the observed peak flow event was insufficient to fully mobilize the bed, and that full mobility is not attained even in areas of the channel with shear stresses exceeding 2.8 times the reference entrainment value. Mobility, or conversely stability, was shown to follow a probabilistic distribution and aligns with findings in a similar study by Chardon et al. (2021).

6.3 Objective 3: Gravel placement strategy

A 2D model was used to develop a priori evaluations of the gravel augmentation design. The model was calibrated using friction based on the velocity measured by an ADCP. The calibrated model was used to predict shear stresses over key design flows, which were then converted to predictions of gravel mobility. The sediment transport analysis was compared to the movements of 168 tracer stones after one year of monitoring. The numerical model was used to evaluate a set of design criteria, including gravel stability under various design flows, hydraulic habitat suitability for Chinook spawning, the risk of fines deposition and the potential for deposited fines to flush from the bed.

Evaluation of the design criteria using the numerical model showed that gravel is most stable along the banks and in the upstream half of the reach where velocity and shear stresses for the return period flows are lowest. However, fines are likely to deposit in these areas under the 7Q10 flow and be resistant to flushing under the 400% MAD. Conversely, Chinook spawning habitat suitability is highest in areas predicted to scour.

A small area on the outside of the bend located at the crest was shown to be fulfill all the design criteria and is expected to be stable up to 100-year flows. However, placing gravel in a small area is not expected to be financially or environmentally cost-effective, as the level of effort required would far exceed potential benefits. Gravel should therefore also be placed outside of this ideal zone, which is primarily limited by the two fines criteria. A lenient consideration of the fines criteria leads to a significant expansion of the suitable area and may be justified given the assumed low sediment input from the upstream lake.

To maximize design effectiveness, a two-pronged approach may be recommended, wherein separate spawning pads are placed in areas of varying adherence to each design criteria, such that the spawning gravel placed further downstream would be in areas of high habitat suitability and high erosion likelihood and gravel placed further upstream would be in areas of low habitat suitability and high stability. The former can provide immediate benefits to Chinook spawners in the reach and to smaller-bodied salmonid spawners further downstream, as the gravel will be well-positioned to mobilize to other high productivity spawning sections. Conversely, the upstream gravel ensures that there is a long-term gravel source in the channel that can undergo a more progressive migration to spawning-suitable areas.

References

Afzalimehr, H. (2010). Effect of non-uniformity of flow on velocity and turbulence intensities over a cobble-bed. *Hydrological Processes*, *24*(3), 331–341. https://doi.org/10.1002/hyp.7495

Afzalimehr, H., & Anctil, F. (2000). Accelerating shear velocity in gravel-bed channels. *Hydrological Sciences Journal*, *45*(1), 113–124. https://doi.org/10.1080/02626660009492309

Alfadhli, I., Yang, S., & Sivakumar, M. (2013). Velocity distribution in non-uniform/unsteady flows and the validity of log law. *13th International Multidisciplinary Scientific Geoconference*, 425–432. https://doi.org/10.5593/SGEM2013/BC3/S12.054

Almeida, J. R. M. de, & Ota, J. J. (2020). Comparative study between turbulence models in curved channels. *RBRH*, *25*, e21. https://doi.org/10.1590/2318-0331.252020190050

Arnaud, F., Paquier, A., Vázquez-Tarrío, D., Camenen, B., Le Coz, J., Michel, K., Naudet, G., Pella, H., & Piégay, H. (2023). Comparing Field, Probabilistic, and 2D Numerical Approaches to Assess Gravel Mobility in a Gravel-Bed River. *Water Resources Research*, *59*(9), e2022WR034127. https://doi.org/10.1029/2022WR034127

Arnaud, F., Piégay, H., Béal, D., Collery, P., Vaudor, L., & Rollet, A. (2017). Monitoring gravel augmentation in a large regulated river and implications for process-based restoration. *Earth Surface Processes and Landforms*, *42*(13), 2147–2166. https://doi.org/10.1002/esp.4161

Arp, C. D., Schmidt, J. C., Baker, M. A., & Myers, A. K. (2007). Stream geomorphology in a mountain lake district: Hydraulic geometry, sediment sources and sinks, and downstream lake effects. *Earth Surface Processes and Landforms*, *32*(4), 525–543. https://doi.org/10.1002/esp.1421

Artelia Eau et Environnement. (2021). *PostTelemac* (1.2.1) [Computer software]. Artelia Eau et Environnement; QGIS Python Plugins Repository. https://plugins.qgis.org/plugins/PostTelemac/

Baptist, M. J., Babovic, V., Uthurburu, J. R., Keijzer, M., Uittenbogaard, R. E., Mynett, A., & Verwey, A. (2007). On inducing equations for vegetation resistance. *Journal of Hydraulic Research*, *45*(4), 435–450. Scopus. https://doi.org/10.1080/00221686.2007.9521778

Beechie, T. J., Sear, D. A., Olden, J. D., Pess, G. R., Buffington, J. M., Moir, H., Roni, P., & Pollock, M. M. (2010). Process-based Principles for Restoring River Ecosystems. *BioScience*, *60*(3), 209–222. https://doi.org/10.1525/bio.2010.60.3.7

Benson, T. (2011, September 13). *Telemac Tools*. MATLAB Central File Exchange. https://www.mathworks.com/matlabcentral/fileexchange/25021-telemac-tools

Bernhardt, E. S., & Palmer, M. A. (2011). River restoration: The fuzzy logic of repairing reaches to reverse catchment scale degradation. *Ecological Applications*, *21*(6), 1926–1931. https://doi.org/10.1890/10-1574.1

Biron, P. M., Carver, R. B., & Carré, D. M. (2012). Sediment Transport and Flow Dynamics Around a Restored Pool in a Fish Habitat Rehabilitation Project: Field and 3d Numerical Modelling Experiments. *River Research and Applications*, *28*(7), 926–939. https://doi.org/10.1002/rra.1488

Brown, R. A., & Pasternack, G. B. (2009). Comparison of methods for analysing salmon habitat rehabilitation designs for regulated rivers. *River Research and Applications*, *25*(6), 745–772. https://doi.org/10.1002/rra.1189

Buffington, J. M., & Montgomery, D. R. (1997). A systematic analysis of eight decades of incipient motion studies, with special reference to gravel-bedded rivers. *Water Resources Research*, *33*(8), 1993–2029. https://doi.org/10.1029/96WR03190

Bunn, S. E., & Arthington, A. H. (2002). Basic Principles and Ecological Consequences of Altered Flow Regimes for Aquatic Biodiversity. *Environmental Management*, *30*(4), 492–507. https://doi.org/10.1007/s00267-002-2737-0

Buscombe, D. (2013). Transferable wavelet method for grain-size distribution from images of sediment surfaces and thin sections, and other natural granular patterns. *Sedimentology*, *60*(7), 1709–1732. https://doi.org/10.1111/sed.12049

Buscombe, D. (2020). SediNet: A configurable deep learning model for mixed qualitative and quantitative optical granulometry. *Earth Surface Processes and Landforms*, *45*(3), 638–651. https://doi.org/10.1002/esp.4760

Buxton, T. H., Buffington, J. M., Tonina, D., Fremier, A. K., & Yager, E. M. (2015). Modeling the influence of salmon spawning on hyporheic exchange of marine-derived nutrients in gravel stream beds. *Canadian Journal of Fisheries and Aquatic Sciences*, *72*(8), 1146–1158. https://doi.org/10.1139/cjfas-2014-0413

Buxton, T. H., Buffington, J. M., Yager, E. M., Hassan, M. A., & Fremier, A. K. (2015). The relative stability of salmon redds and unspawned streambeds: STABILITY OF SALMON REDDS. *Water Resources Research*, *51*(8), 6074–6092. https://doi.org/10.1002/2015WR016908

Cardoso, A. H., Graf, W. H., & Gust, G. (1991). Steady gradually accelerating flow in a smooth open channel. *Journal of Hydraulic Research*, *29*(4), 525–543. https://doi.org/10.1080/00221689109498972

Cassel, M., Lavé, J., Recking, A., Malavoi, J.-R., & Piégay, H. (2021). Bedload transport in rivers, size matters but so does shape. *Scientific Reports*, *11*(1), 508. https://doi.org/10.1038/s41598-020-79930-7

Cassel, M., Piégay, H., Fantino, G., Lejot, J., Bultingaire, L., Michel, K., & Perret, F. (2020). Comparison of ground-based and UAV a-UHF artificial tracer mobility monitoring methods on a braided river. *Earth Surface Processes and Landforms*, *45*(5), 1123–1140. https://doi.org/10.1002/esp.4777

Chapuis, M., Bright, C. J., Hufnagel, J., & MacVicar, B. (2014). Detection ranges and uncertainty of passive Radio Frequency Identification (RFID) transponders for sediment tracking in gravel rivers and coastal environments. *Earth Surface Processes and Landforms*, *39*(15), 2109–2120. https://doi.org/10.1002/esp.3620

Chardon, V., Schmitt, L., Arnaud, F., Piégay, H., & Clutier, A. (2021). Efficiency and sustainability of gravel augmentation to restore large regulated rivers: Insights from three experiments on the Rhine River (France/Germany). *Geomorphology*, *380*, 107639. https://doi.org/10.1016/j.geomorph.2021.107639

Chen, J. M., Pavlic, G., Brown, L., Cihlar, J., Leblanc, S. G., White, H. P., Hall, R. J., Peddle, D. R., King, D. J., Trofymow, J. A., Swift, E., Van Der Sanden, J., & Pellikka, P. K. E. (2002). Derivation and validation of Canada-wide coarse-resolution leaf area index maps using high-resolution satellite imagery and ground measurements. *Remote Sensing of Environment*, *80*(1), 165–184. https://doi.org/10.1016/S0034-4257(01)00300-5

Chiew, Y.-M., & Parker, G. (1994). Incipient sediment motion on non-horizontal slopes. *Journal of Hydraulic Research*, *32*(5), 649–660. https://doi.org/10.1080/00221689409498706

Chow, V. T. (2009). *Open-channel Hydraulics*. Blackburn Press. https://books.google.ca/books?id=JAj7swEACAAJ

Church, M., & Ferguson, R. I. (2015). Morphodynamics: Rivers beyond steady state. *Water Resources Research*, *51*(4), 1883–1897. https://doi.org/10.1002/2014WR016862

Church, M., & Hassan, M. A. (2002). Mobility of bed material in Harris Creek. *Water Resources Research*, *38*(11), 19-1-19–12. https://doi.org/10.1029/2001WR000753

Cienciala, P., & Hassan, M. A. (2013). Linking spatial patterns of bed surface texture, bed mobility, and channel hydraulics in a mountain stream to potential spawning substrate for small resident trout. *Geomorphology*, *197*, 96–107. https://doi.org/10.1016/j.geomorph.2013.04.041

Clauser, F. H. (1956). The Turbulent Boundary Layer. In *Advances in Applied Mechanics* (Vol. 4, pp. 1–51). Elsevier. https://doi.org/10.1016/S0065-2156(08)70370-3

Coleman, H. W., Moffat, R. J., & Kays, W. M. (1977). The accelerated fully rough turbulent boundary layer. *Journal of Fluid Mechanics*, *82*(3), 507–528. https://doi.org/10.1017/S0022112077000810

Coleman, S. E., & Smart, G. M. (2011). Fluvial sediment-transport processes and morphology. *Journal of Hydrology (NZ)*, *50*(1), 37–58.

COSEWIC. (2021, October 12). *Chinook Salmon (Oncorhynchus tshawytscha): COSEWIC assessment and status report 2020* [Featured articles]. Environment and Climate Change Canada. https://www.canada.ca/en/environment-climate-change/services/species-risk-public-registry/cosewic-assessments-status-reports/chinook-salmon-2020.html

Costello, A. B. (2008). The Status of Coastal Cutthroat Trout in British Columbia. In P. J. Connolly, T. H. Williams, & R. E. Greswell (Eds.), *The 2005 Coastal Cutthroat Trout Symposium: Status, Management, Biology, and Conservation* (pp. 24–36). Oregon Chapter, American Fisheries Society. https://web.unbc.ca/~costel0/Publications/Costello_2008.pdf

Cuttler, M. V. W., Lowe, R. J., Falter, J. L., & Buscombe, D. (2017). Estimating the settling velocity of bioclastic sediment using common grain-size analysis techniques. *Sedimentology*, *64*(4), 987–1004. https://doi.org/10.1111/sed.12338

De Jong, J. (2005). *Modelling the influence of vegetation on the morphodynamics of the river Allier* [MSc Thesis, TU Delft]. http://resolver.tudelft.nl/uuid:ac3b5947-11e4-46f9-9e07-66f93d075518

Demir, T., & Walsh, R. P. D. (2005). Shape and Size Characteristics of Bedload Transported During Winter Storm Events in the Cwm Treweryn Stream, Brecon Beacons, South Wales. *Turkish Journal of Earth Sciences*, *14*(1), 105–121.

DeVries, P. (1997). Riverine salmonid egg burial depths: Review of published data and implications for scour studies. *Canadian Journal of Fisheries and Aquatic Sciences*, *54*(8), 1685–1698. https://doi.org/10.1139/f97-090

Dey, S. (2003). Threshold of sediment motion on combined transverse and longitudinal sloping beds. *Journal of Hydraulic Research*, *41*(4), 405–415. https://doi.org/10.1080/00221680309499985

Dey, S., & Debnath, K. (2000). Influence of Streamwise Bed Slope on Sediment Threshold under Stream Flow. *Journal of Irrigation and Drainage Engineering*, *126*(4), 255–263. https://doi.org/10.1061/(ASCE)0733-9437(2000)126:4(255)

Dey, S., & Lambert, M. F. (2005). Reynolds Stress and Bed Shear in Nonuniform Unsteady Open-Channel Flow. *Journal of Hydraulic Engineering*, *131*(7), 610–614. https://doi.org/10.1061/(ASCE)0733-9429(2005)131:7(610)

DFO. (n.d.). *Vancouver Island Hydromet Stations*. Pacfish. Retrieved January 2, 2024, from http://www.pacfish.ca/wcviweather/Content%20Pages/Muchalaht/WaterLevel.aspx

Dietrich, J. T. (2017). Bathymetric Structure-from-Motion: Extracting shallow stream bathymetry from multi-view stereo photogrammetry. *Earth Surface Processes and Landforms*, *42*(2), 355–364. https://doi.org/10.1002/esp.4060

Dodangeh, E., & Afzalimehr, H. (2022). Incipient motion of sediment particles in the presence of bed forms under decelerating and accelerating flows. *Journal of Hydrology and Hydromechanics*, *70*(1), 89–102. https://doi.org/10.2478/johh-2022-0002

Droppo, I. G. (2009). Biofilm structure and bed stability of five contrasting freshwater sediments. *Marine and Freshwater Research*, *60*(7), 690. https://doi.org/10.1071/MF08019

Dusterhoff, S. r., Sloat, M. r., & Ligon, F. k. (2017). The influence of coarse particle mobility on scour depth in salmonid spawning habitat. *River Research and Applications*, *33*(8), 1306–1314. https://doi.org/10.1002/rra.3178

Dysarz, T. (2018). Development of RiverBox—An ArcGIS Toolbox for River Bathymetry Reconstruction. *Water*, *10*(9), Article 9. https://doi.org/10.3390/w10091266

Emadzadeh, A., Chiew, Y. M., & Afzalimehr, H. (2010). Effect of accelerating and decelerating flows on incipient motion in sand bed streams. *Advances in Water Resources*, *33*(9), 1094–1104. https://doi.org/10.1016/j.advwatres.2010.06.014

Esri. (2022). *ArcGIS Pro* (3.0.0) [Computer software]. Esri. https://www.esri.com/en-us/arcgis/products/arcgis-pro/overview

Fang, H. W., Lai, H. J., Cheng, W., Huang, L., & He, G. J. (2017). Modeling sediment transport with an integrated view of the biofilm effects. *Water Resources Research*, *53*(9), 7536–7557. https://doi.org/10.1002/2017WR020628

Ferguson, R. (2007). Flow resistance equations for gravel- and boulder-bed streams: FLOW RESISTANCE EQUATIONS FOR GRAVEL- AND BOULDER-BED STREAMS. *Water Resources Research*, *43*(5). https://doi.org/10.1029/2006WR005422

Ferguson, R. (2010). Time to abandon the Manning equation? *Earth Surface Processes and Landforms*, *35*(15), 1873–1876. https://doi.org/10.1002/esp.2091

Finnigan, J. (2000). Turbulence in plant canopies. *Annual Review of Fluid Mechanics*, *32*, 519–571. Scopus. https://doi.org/10.1146/annurev.fluid.32.1.519

Füstös, V., Erős, T., & Józsa, J. (2021). 2D vs. 3D Numerical Approaches for Fish Habitat Evaluation of a Large River—Is 2D Modeling Sufficient? *Periodica Polytechnica Civil Engineering*. https://doi.org/10.3311/PPci.17788

García, J. H., Ollero, A., Ibisate, A., Fuller, I. C., Death, R. G., & Piégay, H. (2021). Promoting fluvial geomorphology to “live with rivers” in the Anthropocene Era. *Geomorphology*, *380*, 107649. https://doi.org/10.1016/j.geomorph.2021.107649

Geist, D. R., & Dauble, D. D. (1998). Redd Site Selection and Spawning Habitat Use by Fall Chinook Salmon: The Importance of Geomorphic Features in Large Rivers. *Environmental Management*, *22*(5), 655–669. https://doi.org/10.1007/s002679900137

Geist, D. R., Hanrahan, T. P., Arntzen, E. V., McMichael, G. A., Murray, C. J., & Chien, Y.-J. (2002). Physicochemical Characteristics of the Hyporheic Zone Affect Redd Site Selection by Chum Salmon and Fall Chinook Salmon in the Columbia River. *North American Journal of Fisheries Management*, *22*(4), 1077–1085. https://doi.org/10.1577/1548-8675(2002)022<1077:PCOTHZ>2.0.CO;2

Gottesfeld, A. S., Hassan, M. A., & Tunnicliffe, J. F. (2008). Salmon Bioturbation and Stream Process. In School of Geography, University of Southampton Highfield, Southampton, Hampshire SO17 1BJ, UK, D. A. Sear, P. DeVries, & R2 Resource Consultants, Inc. 15250 NE 95th Street, Redmond, Washington 98052, USA (Eds.), *Salmonid Spawning Habitat in Rivers: Physical Controls, Biological Responses, and Approaches to Remediation* (pp. 175–193). American Fisheries Society. https://doi.org/10.47886/9781934874035

Gottesfeld, A. S., Hassan, M. A., Tunnicliffe, J. F., & Poirier, R. W. (2004). SEDIMENT DISPERSION IN SALMON SPAWNING STREAMS: THE INFLUENCE OF FLOODS AND SALMON REDD CONSTRUCTION [1]. *JAWRA Journal of the American Water Resources Association*, *40*(4), 1071–1086. https://doi.org/10.1111/j.1752-1688.2004.tb01068.x

Graba, M., Moulin, F. Y., Boulêtreau, S., Garabétian, F., Kettab, A., Eiff, O., Sánchez-Pérez, J. M., & Sauvage, S. (2010). Effect of near-bed turbulence on chronic detachment of epilithic biofilm: Experimental and modeling approaches. *Water Resources Research*, *46*(11). https://doi.org/10.1029/2009WR008679

Graf, W. H., & Song, T. (1995). Bed-shear stress in non-uniform and unsteady open-channel flows. *Journal of Hydraulic Research*, *33*(5), 699–704. https://doi.org/10.1080/00221689509498565

Harrison, L. R., Legleiter, C. J., Sridharan, V. K., Dudley, P. N., & Daniels, M. E. (2022). Evaluating the Sensitivity of Multi-Dimensional Model Predictions of Salmon Habitat to the Source of Remotely Sensed River Bathymetry. *Water Resources Research*, *58*(12), e2022WR033097. https://doi.org/10.1029/2022WR033097

Hassan, M. A., Gottesfeld, A. S., Montgomery, D. R., Tunnicliffe, J. F., Clarke, G. K. C., Wynn, G., Jones-Cox, H., Poirier, R., MacIsaac, E., Herunter, H., & Macdonald, S. J. (2008). Salmon-driven bed load transport and bed morphology in mountain streams. *Geophysical Research Letters*, *35*(4), 2007GL032997. https://doi.org/10.1029/2007GL032997

Hassan, M. A., Petticrew, E. L., Montgomery, D. R., Gottesfeld, A. S., & Rex, J. F. (2011). Salmon as Biogeomorphic Agents in Gravel Bed Rivers: The Effect of Fish on Sediment Mobility and Spawning Habitat. In A. Simon, S. J. Bennett, & J. M. Castro (Eds.), *Geophysical Monograph Series* (pp. 337–352). American Geophysical Union. https://doi.org/10.1029/2010GM000968

Hassan, M. A., Tonina, D., & Buxton, T. H. (2015). Does small-bodied salmon spawning activity enhance streambed mobility?: SOCKEYE SALMON AND SEDIMENT MOBILITY. *Water Resources Research*, *51*(9), 7467–7484. https://doi.org/10.1002/2015WR017079

Hassan, M. A., Voepel, H., Schumer, R., Parker, G., & Fraccarollo, L. (2013). Displacement characteristics of coarse fluvial bed sediment. *Journal of Geophysical Research: Earth Surface*, *118*(1), 155–165. https://doi.org/10.1029/2012JF002374

Hauer, C., Pulg, U., Gabrielsen, S.-E., & Barlaup, B. T. (2015). Application of step-backwater modelling for salmonid spawning habitat restoration in Western Norway. *Ecohydrology*, *8*(7), 1239–1261. https://doi.org/10.1002/eco.1578

Hauer, C., Pulg, U., Reisinger, F., & Flödl, P. (2020). Evolution of artificial spawning sites for Atlantic salmon (Salmo salar) and sea trout (Salmo trutta): Field studies and numerical modelling in Aurland, Norway. *Hydrobiologia*, *847*(4), 1139–1158. https://doi.org/10.1007/s10750-019-04173-1

Helm, C. (2019). *A rapid and objective characterization of channel morphology in a small, forested channel using a remotely piloted aircraft.* [MSc, University of British Columbia]. https://open.library.ubc.ca/media/stream/pdf/24/1.0380361/4

Helm, C., Hassan, M. A., & Reid, D. (2020). Characterization of morphological units in a small, forested stream using close-range remotely piloted aircraft imagery. *Earth Surface Dynamics*, *8*(4), 913–929. https://doi.org/10.5194/esurf-8-913-2020

Hervouet, J.-M. (1991). Telemac, a fully vectorised finite element software for shallow water equations. *Proceedings of the 2nd International Conference on Computer Methods in Water Resources*, 147–158. Scopus. https://www.scopus.com/inward/record.uri?eid=2-s2.0-0026393160&partnerID=40&md5=c447d1b40046ae3e23e9309cf2dd171d

Hervouet, J.-M. (1994). Computation of 2D free surface flows: The state of the art in the TELEMAC system. *Hydroinformatics '94. Proc. 1st International Conference, Delft, 1994. Vol. 1*, *1*, 301–306. Scopus. https://www.scopus.com/inward/record.uri?eid=2-s2.0-0028578304&partnerID=40&md5=854b1b7084eed8fe40b8793b2b6ee148

Hervouet, J.-M. (1999). TELEMAC, a hydroinformatic system. *La Houille Blanche*, *85*(3–4), 21–28. https://doi.org/10.1051/lhb/1999029

Hervouet, J.-M. (2007). *Hydrodynamics of free surface flows: Modelling with the finite element method*. Wiley. https://onlinelibrary-wiley-com.proxy.lib.uwaterloo.ca/doi/book/10.1002/9780470319628

Hodge, R. A., & Buechel, M. E. H. (2022). The influence of bedrock river morphology and alluvial cover on gravel entrainment. Part 2: Modelling critical shear stress. *Earth Surface Processes and Landforms*, *47*(14), 3348–3360. https://doi.org/10.1002/esp.5462

Humphries, R., Venditti, J. G., Sklar, L. S., & Wooster, J. K. (2012). Experimental evidence for the effect of hydrographs on sediment pulse dynamics in gravel-bedded rivers. *Water Resources Research*, *48*(1). https://doi.org/10.1029/2011WR010419

Iannetta, M. (2020). *Monitoring Station and Application in a Rural Stream in Southern Ontario* [MASc]. University of Waterloo.

Juez, C., Battisacco, E., Schleiss, A. J., & Franca, M. J. (2016). Assessment of the performance of numerical modeling in reproducing a replenishment of sediments in a water-worked channel. *Advances in Water Resources*, *92*, 10–22. https://doi.org/10.1016/j.advwatres.2016.03.010

Kironoto, B. A., & Graf, W. H. (1995). TURBULENCE CHARACTERISTICS IN ROUGH NON-UNIFORM OPEN-CHANNEL FLOW. *Proceedings of the Institution of Civil Engineers - Water, Maritime and Energy*, *112*(4), 336–348. https://doi.org/10.1680/iwtme.1995.28114

Kondolf, G. M., & Wolman, M. G. (1993). The sizes of salmonid spawning gravels. *Water Resources Research*, *29*(7), 2275–2285. https://doi.org/10.1029/93WR00402

Lane, S. N., Bradbrook, K. F., Richards, K. S., Biron, P. A., & Roy, A. G. (1999). The application of computational fluid dynamics to natural river channels: Three-dimensional versus two-dimensional approaches. *Geomorphology*, *29*(1–2), 1–20. https://doi.org/10.1016/S0169-555X(99)00003-3

Lennox, R. J., Pulg, U., Malley, B., Gabrielsen, S.-E., Hanssen, E. M., Cooke, S. J., Birnie-Gauvin, K., Barlaup, B. T., & Vollset, K. W. (2021). The various ways that anadromous salmonids use lake habitats to complete their life history. *Canadian Journal of Fisheries and Aquatic Sciences*, *78*(1), 90–100. https://doi.org/10.1139/cjfas-2020-0225

Liébault, F., Piégay, H., Cassel, M., & Arnaud, F. (2023). Bedload tracing with RFID tags in gravel-bed rivers: Review and meta-analysis after 20 years of field and laboratory experiments. *Earth Surface Processes and Landforms*, esp.5704. https://doi.org/10.1002/esp.5704

Liébault, F., Piégay, H., Cassel, M., & Arnaud, F. (2024). Bedload tracing with RFID tags in gravel-bed rivers: Review and meta-analysis after 20 years of field and laboratory experiments. *Earth Surface Processes and Landforms*, *49*(1), 147–169. https://doi.org/10.1002/esp.5704

Liedermann, M., Tritthart, M., & Habersack, H. (2013). Particle path characteristics at the large gravel-bed river Danube: Results from a tracer study and numerical modelling. *Earth Surface Processes and Landforms*, *38*(5), 512–522. https://doi.org/10.1002/esp.3338

Lisle, T. E. (1989). Sediment transport and resulting deposition in spawning gravels, north coastal California. *Water Resources Research*, *25*(6), 1303–1319. https://doi.org/10.1029/WR025i006p01303

López, R., & Barragán, J. (2008). Equivalent Roughness of Gravel-Bed Rivers. *Journal of Hydraulic Engineering*, *134*(6), 847–851. https://doi.org/10.1061/(ASCE)0733-9429(2008)134:6(847)

MacVicar, B., Chapuis, M., Buckrell, E., & Roy, A. (2015). Assessing the Performance of In-Stream Restoration Projects Using Radio Frequency Identification (RFID) Transponders. *Water*, *7*(10), 5566–5591. https://doi.org/10.3390/w7105566

MacVicar, B. J., & Papangelakis, E. (2022). Lost and found: Maximizing the information from a series of bedload tracer surveys. *Earth Surface Processes and Landforms*, *47*(2), 399–408. https://doi.org/10.1002/esp.5255

MacVicar, B. J., & Roy, A. G. (2007). Hydrodynamics of a forced riffle pool in a gravel bed river: 1. Mean velocity and turbulence intensity. *Water Resources Research*, *43*(12). https://doi.org/10.1029/2006WR005272

Milhous, R. T. (1998). Modelling of instream flow needs: The link between sediment and aquatic habitat. *Regulated Rivers: Research & Management*, *14*(1), 79–94. https://doi.org/10.1002/(SICI)1099-1646(199801/02)14:1<79::AID-RRR478>3.0.CO;2-9

Milhous, R. T., & Waddle, T. J. (2012). *Physical Habitat Simulation (PHABSIM) Software for Windows* [Computer software]. USGS Fort Collins Science Center. https://www.sciencebase.gov/catalog/item/56bcd45ae4b08d617f66aa42

Miller, J. R., & Kochel, R. C. (2010). Assessment of channel dynamics, in-stream structures and post-project channel adjustments in North Carolina and its implications to effective stream restoration. *Environmental Earth Sciences*, *59*(8), 1681–1692. https://doi.org/10.1007/s12665-009-0150-1

Moir, H. J., & Pasternack, G. B. (2010). Substrate requirements of spawning Chinook salmon (Oncorhynchus tshawytscha) are dependent on local channel hydraulics. *River Research and Applications*, *26*(4), 456–468. https://doi.org/10.1002/rra.1292

Montgomery, D. R., Buffington, J. M., Peterson, N. P., Schuett-Hames, D., & Quinn, T. P. (1996). Stream-bed scour, egg burial depths, and the influence of salmonid spawning on bed surface mobility and embryo survival. *Canadian Journal of Fisheries and Aquatic Sciences*, *53*(5), 1061–1070. https://doi.org/10.1139/f96-028

Mörtl, C., & De Cesare, G. (2021). Sediment Augmentation for River Rehabilitation and Management—A Review. *Land*, *10*(12), 1309. https://doi.org/10.3390/land10121309

Mörtl, C., Schroff, R., Stähly, S., & De Cesare, G. (2023). Influence of channel geomorphic units on bedload transport and river morphology during low-magnitude bed-forming floods coupled with sediment augmentation. *Earth Surface Processes and Landforms*, *48*(12), 2395–2409. https://doi.org/10.1002/esp.5635

Mueller, D. S., & Wagner, C. R. (2013). Techniques and Methods 3-A22: Measuring Discharge with Acoustic Doppler Current Profilers from a Moving Boat. In *Book 3, Application of Hydraulics: Section A: Surface-Water Techniques*. https://pubs.usgs.gov/tm/3a22/pdf/tm3a22.pdf

Myers, A. K., Marcarelli, A. M., Arp, C. D., Baker, M. A., & Wurtsbaugh, W. A. (2007). Disruptions of stream sediment size and stability by lakes in mountain watersheds: Potential effects on periphyton biomass. *Journal of the North American Benthological Society*, *26*(3), 390–400. https://doi.org/10.1899/06-086.1

Najafabadi, E. F., & Afzalimehr, H. (2020). Comparison of Two- and Three-Dimensional Flow and Habitat Modeling in Pool–Riffle Sequences. *Iranian Journal of Science and Technology, Transactions of Civil Engineering*, *44*(3), 991–1000. https://doi.org/10.1007/s40996-019-00298-4

Nezu, I. (2005). Open-Channel Flow Turbulence and Its Research Prospect in the 21st Century. *Journal of Hydraulic Engineering*, *131*(4), 229–246. https://doi.org/10.1061/(ASCE)0733-9429(2005)131:4(229)

Nichols, G. (2010). *Sedimentology and stratigraphy* (2. ed., [Nachdr.]). Wiley-Blackwell.

Nikuradse, J. (1930). Untersuchungen über turbulente Strömungen in nicht kreisförmigen Rohren. *Ingenieur-Archiv*, *1*(3), 306–332. Scopus. https://doi.org/10.1007/BF02079937

NRCan CGS. (n.d.-a). *GPS·H*. Government of Canada. Retrieved April 25, 2023, from https://webapp.csrs-scrs.nrcan-rncan.gc.ca/geod/tools-outils/gpsh.php

NRCan CGS. (n.d.-b). *Precise Point Positioning*. Government of Canada. Retrieved January 2, 2024, from https://webapp.csrs-scrs.nrcan-rncan.gc.ca/geod/tools-outils/ppp.php

Olden, J. D., Poff, N. L., & Bestgen, K. R. (2006). LIFE-HISTORY STRATEGIES PREDICT FISH INVASIONS AND EXTIRPATIONS IN THE COLORADO RIVER BASIN. *Ecological Monographs*, *76*(1), 25–40. https://doi.org/10.1890/05-0330

Palmer, M. A., Bernhardt, E. S., Allan, J. D., Lake, P. S., Alexander, G., Brooks, S., Carr, J., Clayton, S., Dahm, C. N., Follstad Shah, J., Galat, D. L., Loss, S. G., Goodwin, P., Hart, D. D., Hassett, B., Jenkinson, R., Kondolf, G. M., Lave, R., Meyer, J. L., … Sudduth, E. (2005). Standards for ecologically successful river restoration. *Journal of Applied Ecology*, *42*(2), 208–217. https://doi.org/10.1111/j.1365-2664.2005.01004.x

Papangelakis, E., & Hassan, M. A. (2016). The role of channel morphology on the mobility and dispersion of bed sediment in a small gravel-bed stream. *Earth Surface Processes and Landforms*, *41*(15), 2191–2206. https://doi.org/10.1002/esp.3980

Papangelakis, E., & MacVicar, B. (2020). Process-based assessment of success and failure in a constructed riffle-pool river restoration project. *River Research and Applications*, *36*(7), 1222–1241. https://doi.org/10.1002/rra.3636

Papangelakis, E., MacVicar, B. J., Montakhab, A. F., & Ashmore, P. (2022). Flow Strength and Bedload Sediment Travel Distance in Gravel Bed Rivers. *Water Resources Research*, *58*(7), e2022WR032296. https://doi.org/10.1029/2022WR032296

Parker, C., Clifford, N. J., & Thorne, C. R. (2011). Understanding the influence of slope on the threshold of coarse grain motion: Revisiting critical stream power. *Geomorphology*, *126*(1–2), 51–65. https://doi.org/10.1016/j.geomorph.2010.10.027

Pasternack, G. B., Wang, C. L., & Merz, J. E. (2004). Application of a 2D hydrodynamic model to design of reach-scale spawning gravel replenishment on the Mokelumne River, California. *River Research and Applications*, *20*(2), 205–225. https://doi.org/10.1002/rra.748

Pike, R. G., Bennett, K. E., Redding, T. E., Werner, A. T., Spittlehouse, D. L., Murdock, T. Q., Beckers, J., Smerdon, B. D., Bladon, K. D., Foord, V. N., Campbell, D. A., & Tschaplinski, P. J. (2010). Climate Change Effects on Watershed Processes in British Columbia. In R. G. Pike, T. E. Redding, R. D. Moore, R. D. Winkler, & K. D. Bladon (Eds.), *Compendium of forest hydrology and geomorphology in British Columbia*. Forest Science Program / FORREX.

Poff, N. L., Allan, J. D., Bain, M. B., Karr, J. R., Prestegaard, K. L., Richter, B. D., Sparks, R. E., & Stromberg, J. C. (1997). The Natural Flow Regime. *BioScience*, *47*(11), 769–784. https://doi.org/10.2307/1313099

Poirier, R. (2003). *The effects of floods and sockeye salmon on streambed morphology*. [Master of Science, University of Northern British Columbia]. https://doi.org/10.24124/2005/bpgub298

Ptolemy, R. (2001). *Water use planning (WUP) Delphi curves*. B.C. Ministry of Environment.

Ptolemy, R., & Lewis, A. (2002). *Rationale for Multiple British Columbia Instream Flow Standards to Maintain Ecosystem Function and Biodiversity*. Ministry of Water, Land and Air Protection. https://a100.gov.bc.ca/pub/acat/documents/r18275/Instreamflowstandards_1275074130922_78cea088131303970ff0b3ff48ffbcf79ded1493229dd7763a6ba073499a3e22.pdf

Purinton, B., & Bookhagen, B. (2019). *Introducing PebbleCounts: A grain-sizing tool for photo surveys of dynamic gravel-bed rivers* [Preprint]. Physical: Geomorphology (including all aspects of fluvial, coastal, aeolian, hillslope and glacial geomorphology). https://doi.org/10.5194/esurf-2019-20

QGIS Development Team. (2022). *QGIS Geographic Information System* (3.26.2-Buenos Aires) [Computer software]. Open Source Geospatial Foundation Project. http://qgis.osgeo.org/

Rastogi, A. K., & Rodi, W. (1978). Predictions of Heat and Mass Transfer in Open Channels. *Journal of the Hydraulics Division*, *104*(3), 397–420. https://doi.org/10.1061/JYCEAJ.0004962

Rathburn, S., & Wohl, E. (2003). Predicting fine sediment dynamics along a pool-riffle mountain channel. *Geomorphology*, *55*(1–4), 111–124. https://doi.org/10.1016/S0169-555X(03)00135-1

Reiser, D. W., Ramey, M. P., & Lambert, T. R. (1985). *Review of Flushing Flow Requirements in Regulated Streams, Completion Report, Pacific Gas and Electric Company, Department of Engineering Research, San Ramon, California* (p. 97).

Rosgen, D. L. (1994). A classification of natural rivers. *CATENA*, *22*(3), 169–199. https://doi.org/10.1016/0341-8162(94)90001-9

Rosgen, D. L. (2021). Comment on "Promoting fluvial geomorphology to 'live with rivers' in the Anthropocene Era" by J.H. García et al. (2021). *Geomorphology*, *389*, 107754. https://doi.org/10.1016/j.geomorph.2021.107754

Rotta, J. C. (1962). Turbulent boundary layers in incompressible flow. *Progress in Aerospace Sciences*, *2*(1), 1–95. https://doi.org/10.1016/0376-0421(62)90014-3

Rounds, S. A., Pilson, S. L., Sullivan, A. B., & Stonewall, A. J. (2020). *Evaluation of Restoration Alternatives Using Hydraulic Models of Lake Outflow at Wapato Lake National Wildlife Refuge, Northwestern Oregon:* (2020–5014; U.S. Geological Survey Scientific Investigations Report). U.S. Geological Survey. https://doi.org/10.3133/sir20205014

Saldi-Caromile, K., Bates, K. K., Skidmore, P., & Barenti, J. (2004). *Stream Habitat Restoration Guidelines*. Washington Department of Fish & Wildlife. https://wdfw.wa.gov/publications/00043

Scheurer, K., Alewell, C., Bänninger, D., & Burkhardt-Holm, P. (2009). Climate and land-use changes affecting river sediment and brown trout in alpine countries—A review.

Environmental Science and Pollution Research, *16*(2), 232–242. https://doi.org/10.1007/s11356-008-0075-3

Schmidt, K.-H., & Ergenzinger, P. (1992). Bedload entrainment, travel lengths, step lengths, rest periods—Studied with passive (iron, magnetic) and active (radio) tracer techniques. *Earth Surface Processes and Landforms*, *17*(2), 147–165. https://doi.org/10.1002/esp.3290170204

Sear, D. A., Frostick, L. E., Rollinson, G., & Lisle, T. E. (2008). The significance and mechanics of fine-sediment infiltration and accumulation in gravel spawning beds. In D. A. Sear & P. DeVries (Eds.), *Salmonid Spawning Habitat in Rivers: Physical Controls, Biological Responses and Approaches to Remediation.*

Shrivastava, S., Stewardson, M. J., & Arora, M. (2020). Understanding streambeds as complex systems: Review of multiple interacting environmental processes influencing streambed permeability. *Aquatic Sciences*, *82*(4), 67. https://doi.org/10.1007/s00027-020-00741-z

Slaney, P. A., & Zaldokas, D. (Eds.). (1997). *Fish Habitat Rehabilitation Procedures Watershed Restoration Technical Circular No. 9*.

Song, T., & Chiew, Y. M. (2001). Turbulence Measurement in Nonuniform Open-Channel Flow Using Acoustic Doppler Velocimeter (ADV). *Journal of Engineering Mechanics*, *127*(3), 219–232. https://doi.org/10.1061/(ASCE)0733-9399(2001)127:3(219)

Song, Y., Huang, J., Toorman, E., & Yang, G. (2020). Reconstruction of River Topography for 3D Hydrodynamic Modelling Using Surveyed Cross-Sections: An Improved Algorithm. *Water*, *12*(12), 3539. https://doi.org/10.3390/w12123539

Staentzel, C., Kondolf, G. M., Schmitt, L., Combroux, I., Barillier, A., & Beisel, J.-N. (2020). Restoring fluvial forms and processes by gravel augmentation or bank erosion below dams: A systematic review of ecological responses. *Science of The Total Environment*, *706*, 135743. https://doi.org/10.1016/j.scitotenv.2019.135743

Stone, M., Emelko, M. B., Droppo, I. G., & Silins, U. (2011). Biostabilization and erodibility of cohesive sediment deposits in wildfire-affected streams. *Water Research*, *45*(2), 521–534. https://doi.org/10.1016/j.watres.2010.09.016

Sturm, T. W. (2010). *Open Channel Hydraulics* (2nd ed.). McGraw-Hill. https://books.google.ca/books?id=eQh8nQAACAAJ

Sweeney-Bergen, E. K., Macintyre, D., & Moore, J. W. (2021). Ontogenetic habitat shifts and vulnerability: Lake-outlet-spawning sockeye salmon (Oncorhynchus nerka) sensitivity to habitat connectivity and hydrologic change. *Environmental Biology of Fishes*, *104*(4), 383–399. https://doi.org/10.1007/s10641-021-01071-1

The Mathworks Inc. (2022). *MATLAB version 9.12.0.2327980 (R2022a) Update 7* [Computer software]. The MathWorks Inc. https://www.mathworks.com

Tonina, D., & Buffington, J. M. (2009). A three-dimensional model for analyzing the effects of salmon redds on hyporheic exchange and egg pocket habitat. *Canadian Journal of Fisheries and Aquatic Sciences*, *66*(12), 2157–2173. https://doi.org/10.1139/F09-146

USGS. (2021). *OSW Hydroacoustics: WinRiver II* (2.24) [Computer software]. United States Geological Survey. https://hydroacoustics.usgs.gov/movingboat/WinRiverII.shtml

Washington State Department of Ecology. (2021). *Salmon Spawning Habitat Protection Rule: Preliminary Technical Support Document* (Preliminary Rule Implementation Plan 21-10–049). Washington State Department of Ecology. https://apps.ecology.wa.gov/publications/summarypages/2110050.html

Webb, J. A., Guo, D., Koster, W. M., Lauchlan-Arrowsmith, C., & Vietz, G. J. (2022). Can hydraulic measures of river conditions improve our ability to predict ecological responses to changing flows? Flow velocity and spawning of an iconic native Australian fish. *Frontiers in Environmental Science*, *10*, 882495. https://doi.org/10.3389/fenvs.2022.882495

West, D. T., Greenacre, D., Girard, I., Marriner, A., Li, P., Iun, M. R., MacVicar, B. J., Sheng, M., & Hocking, M. D. (2023). *Muchalat Lake Outlet Gravel Placement – Detailed Design Report* (Consultant's Report Prepared for the Nootka Sound Watershed Society 1463–03). Ecofish Research Ltd.

Wheaton, J. M., Brasington, J., Darby, S. E., Merz, J., Pasternack, G. B., Sear, D., & Vericat, D. (2010). Linking geomorphic changes to salmonid habitat at a scale relevant to fish. *River Research and Applications*, *26*(4), 469–486. https://doi.org/10.1002/rra.1305

White, F. M. (1991). *Viscous fluid flow* (2nd ed). McGraw-Hill.

Whiting, P. J. (1997). The Effect of Stage on Flow and Components of the Local Force Balance. *Earth Surface Processes and Landforms*, *22*(6), 517–530. https://doi.org/10.1002/(SICI)1096-9837(199706)22:6<517::AID-ESP707>3.0.CO;2-M

Whiting, P. J., & Dietrich, W. E. (1991). Convective accelerations and boundary shear stress over a Channel Bar. *Water Resources Research*, *27*(5), 783–796. https://doi.org/10.1029/91WR00083

Wilcock, P. R. (2012). Stream Restoration in Gravel-Bed Rivers. In M. Church, P. M. Biron, & A. G. Roy (Eds.), *Gravel-Bed Rivers* (1st ed., pp. 135–149). Wiley. https://doi.org/10.1002/9781119952497.ch12

Wilcock, P. R., & Crowe, J. C. (2003). Surface-based Transport Model for Mixed-Size Sediment. *Journal of Hydraulic Engineering*, *129*(2), 120–128. https://doi.org/10.1061/(ASCE)0733-9429(2003)129:2(120)

Wilcock, P. R., & McArdell, B. W. (1993). Surface-based fractional transport rates: Mobilization thresholds and partial transport of a sand-gravel sediment. *Water Resources Research*, *29*(4), 1297–1312. https://doi.org/10.1029/92WR02748

Winkler, R. D., Redding, T. E., Spittlehouse, D. L., Smerdon, B. D., & Carlyle-Moses, D. E. (2010). The Effects of Forest Disturbance on Hydrologic Processes and Watershed Response. In R. G. Pike, T. E. Redding, R. D. Moore, R. D. Winkler, & K. D. Bladon (Eds.), *Compendium of forest hydrology and geomorphology in British Columbia*. Forest Science Program / FORREX.

Wohl, E. (2005). Compromised Rivers: Understanding Historical Human Impacts on Rivers in the Context of Restoration. *Ecology and Society*, *10*(2), art2. https://doi.org/10.5751/ES-01339-100202

Wohl, E., Lane, S. N., & Wilcox, A. C. (2015). The science and practice of river restoration. *Water Resources Research*, *51*(8), 5974–5997. https://doi.org/10.1002/2014WR016874

Xiao, Y., Yuan, K., Zhang, T., & Zhou, J. (2023). Analytical and experimental study of velocity distribution in adverse-slope channel flow. *Journal of Hydraulic Research*, *61*(4), 437–451. https://doi.org/10.1080/00221686.2023.2231396

Yang, S.-Q., & Chow, A. T. (2008). Turbulence structures in non-uniform flows. *Advances in Water Resources*, *31*(10), 1344–1351. https://doi.org/10.1016/j.advwatres.2008.06.006

Yang, S.-Q., & Lee, J.-W. (2007). Reynolds shear stress distributions in a gradually varied flow in a roughened channel. *Journal of Hydraulic Research*, *45*(4), 462–471. https://doi.org/10.1080/00221686.2007.9521780

Yang, S.-Q., Xu, W.-L., & Yu, G.-L. (2006). Velocity distribution in a gradually accelerating free surface flow. *Advances in Water Resources*, *29*(12), 1969–1980. https://doi.org/10.1016/j.advwatres.2006.02.002

Zeug, S. C., Sellheim, K., Watry, C., Rook, B., Hannon, J., Zimmerman, J., Cox, D., & Merz, J. (2014). Gravel Augmentation Increases Spawning Utilization by Anadromous Salmonids: A

Case Study from California, Usa. *River Research and Applications*, *30*(6), 707–718. https://doi.org/10.1002/rra.2680

Zhang, W., Qi, J., Wan, P., Wang, H., Xie, D., Wang, X., & Yan, G. (2016). An Easy-to-Use Airborne LiDAR Data Filtering Method Based on Cloth Simulation. *Remote Sensing*, *8*(6), 501. https://doi.org/10.3390/rs8060501

Zhang, X.-F., Yang, W.-T., & Xia, J.-Q. (2016). Bed shear stress in non-uniform flow. *Environmental Fluid Mechanics*, *16*(4), 777–792. https://doi.org/10.1007/s10652-016-9448-1

Zingg, T. (1935). *Beitrag zur Schotteranalyse* (p. 102 S.) [ETH Zurich; Application/pdf]. https://doi.org/10.3929/ETHZ-A-000103455

Appendices

Appendix A
Additional data and processing

A1) Watershed map

The Gold River watershed is shown in the following figure.

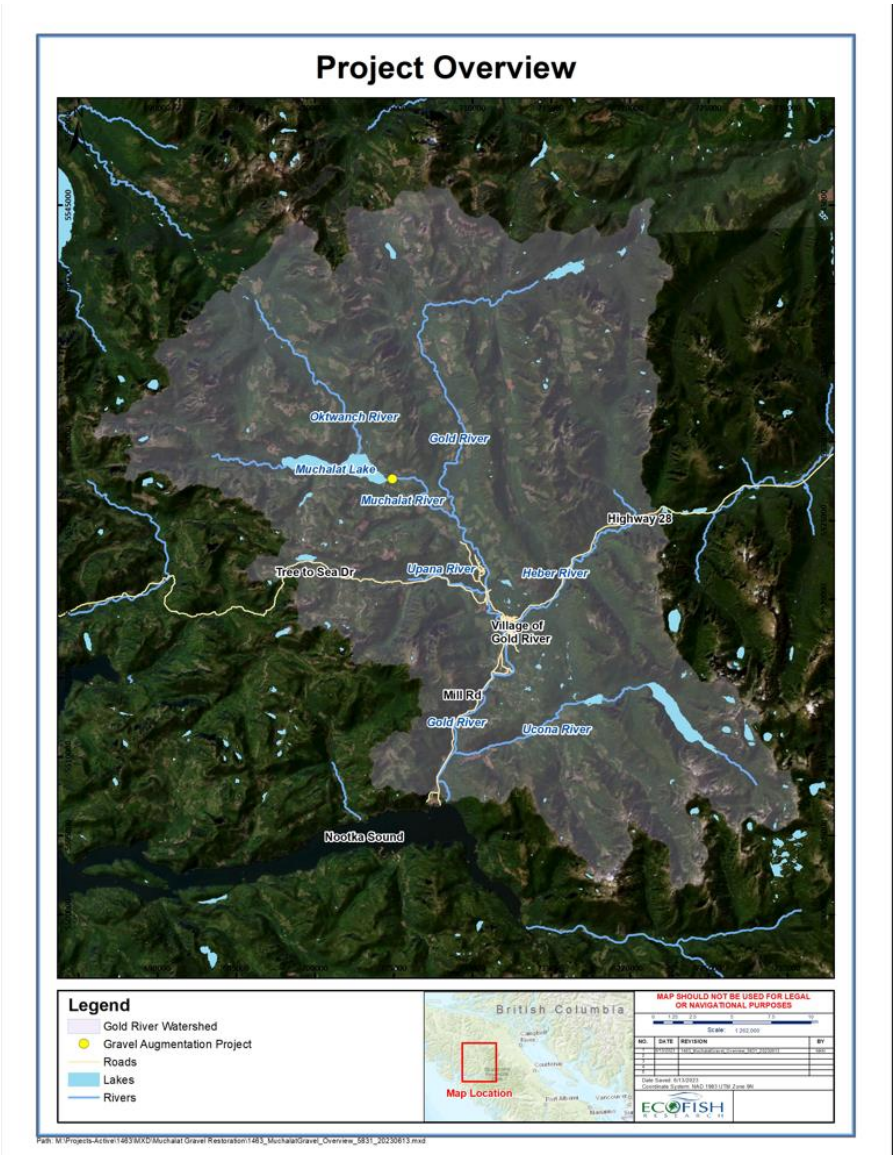


Figure A - 1 Map of the Gold River watershed. From West et al. (2023).

A2) Benchmark errors

The BM system established by Ecofish is summarized in Table A- 1.

Table A- 1 Coordinates of the benchmarks installed by Ecofish, from upstream to downstream

Station	Northing (m)	Easting (m)	Elevation (masl)	Notes
BM045	5528457.769	273478.752	196.279	
BM046	5528514.499	273660.345	197.508	
BM061	—	—	—	Adjacent to BM049
BM049	—	—	—	Upstream gauge
BM073	5528511.115	273825.794	195.762	
BM070	5528530.144	273903.886	197.571	
BM032	5528496.400	273932.560	196.521	
BM082	5528528.937	273990.506	196.012	
BM082 – WFT2	5528526.199	273994.274	199.840	Resurveyed by UW
BM052	5528501.058	274122.837	195.584	Adjacent to Solinst SP
Solinst SP	5528502.686	274124.073	194.874	Downstream gauge

BM082 was used as a base station by UW during WFT2 and was resurveyed with a 6h20m occupation using an RTK GPS. A temporary control point (TCP) was also surveyed during WFT2 near BM070. The GPS data was processed using the Canadian Spatial Reference System Precise Point Positioning (CSRS-PPP) webtool that is publicly available via the Canadian Geodetic Survey (CGS) website (NRCan CGS, n.d.-b). The resurveyed coordinates were used to tie the local coordinates of total station points measured during WFT2 to the project coordinate system.

Notably, 2-3 m of error in each of the x-, y- and z-directions was found between the GPS coordinates from the two measurements. The error between the measurements is expected to be caused by the difference in occupation times, as the BMs surveyed by Ecofish were only occupied for short durations.

A3) Total station survey transformations

Transformations of the coordinates measured by the total station during WFT2 were applied individually for each field day as different CPs were used. The transformation error was defined as

the difference between the project coordinates measured by Ecofish and the transformed data. The difference in northing and easting from the project values and the GPS occupation was quantified at BM032, then used to estimate “project-equivalent” coordinates at the TCP. The transformation error for each day is summarized in Table A- 2.

Table A- 2 Transformation error for total station set-ups on each field day

Date	CP1	CP2	CP2 Error (X / Y / Total) (m)
2023/08/04	BM082	TCP	0.161 / 0.017 / 0.162
2023/08/05	BM082	BM032	0.006 / 0.003 / 0.007
2023/08/06	TCP	BM032	0.064 / 0.024 / 0.069

The error was within 10 cm for each dataset except for the first day. Only tracer stone locations were surveyed on the first day (GCPs and the cross-section at BM052 were surveyed on the remaining days) and precise coordinates are not critical for determining mobility patterns, thus the margin of error for this day was considered acceptable.

A4) Water level gauge stages for design flows

The stage-discharge rating curve equations for the site gauges were used to calculate the WSEs at the gauges for each design flow. These values are listed in Table A- 3.

Table A- 3 Water surface elevations for design flows at the water level gauges

Flow scenario	Discharge (m^3/s)	Pacfish/MCH-LG01 gauge WSE (masl)	Solinst/MCH-LG02 gauge WSE (masl)
7Q10	0.55	194.97	194.80
LoFT	1.17	195.04	194.88
MeFT	10.2	195.50	195.30
Cnspawn	25.9	195.94	195.63
Cospawn	42.3	196.27	195.87
Flush	87.5	196.96	196.32
HiFT	123	197.38	196.58
2yr	474	197.63	198.07
10yr	759	200.09	198.81
20yr	866	201.60	199.05
50yr	1005	202.09	199.34
100yr	1112	202.70	199.54
200yr	1220	203.13	199.73

Appendix B
RPAS Photogrammetry process

B1) RPAS flights

Flight 1 was completed in the morning under no wind and bright light from the sun rising in the east. Shadows were cast on the left bank (LB), but right bank (RB) was well illuminated. The photos were primarily shot nadir for this flight.

Flight 2 consisted of one pass nadir and two oblique passes of each bank with the camera angled 20-30º from the vertical. The first pass was flown from upstream to downstream along the RB then towards the upstream along the LB. The oblique passes also first travelled downstream parallel to the bank before flying upstream, with the camera slightly oriented towards the direction of travel. Some eastward wind was present during the flight, which presented some reflective distortions on the water surface in the photos taken upstream of the crest. The bright lighting minimized shadows but resulted in significant reflection of the clouds in the sky on the water surface through the downstream pool, thus limiting visibility through the water surface.

Flight 3 was also subject to some wind effects, but the flight was primarily completed downstream of the crest which reduced the impact of the wind on the surface water. Flight 3 consisted of angled passes (15-25º) along the RB of the stream downstream of the control. Shadows were present along this bank, but the lower lighting condition resulted in minimal reflections.

B2) Structure-from-Motion data processing workflow

The workflow for extracting data from the RPAS images was loosely based on Dietrich (2017) and Helm et al. (2020), with some changes to account for the difference in GCP placement. The photos from the three RPAS flights were imported into the photogrammetry software Agisoft Photoscan. The GPS coordinates on the photo were converted to NAD83 UTM10 to align with the project coordinate system. The images with quality values below 0.70 were removed. The photos were aligned and used to generate a dense point cloud. Markers were added to the photos by selecting the center of the X's on the GCPs on at least one photo where the GCPs were visible. A list of the GCPs and their coordinates was imported into Agisoft, and each GCP was assigned to the corresponding marker. The GPS coordinates of the images were then cleared so that only the GCP coordinates would dictate the

reference system of the photogrammetry model. Six GCP points were also removed from the reference system to avoid overfitting the model and to provide validation points.

The marker locations were refined by filtering the photos by visible markers and manually parsing through each image to verify whether the projected marker location matched the center of the X. Marker locations were adjusted to the center where necessary, while keeping track of the absolute projection error. The markers were unpinned if the adjustment resulted in significantly higher error. The reference pane was updated, and the camera alignment re-optimized to recalculate the error.

B3) Structure-from-Motion model error

Most of the referenced GCPs had less than 0.05 m error between the measured and projected elevations. Seven of the 18 referenced GCPs had errors exceeding 0.05 m, with one anomalous point having error that exceeded 0.20 m. The root mean square (RMS) of the vertical projection errors from the 18 GCPs used in the alignment was 0.082 m, while the mean of the absolute values (MAV) of these errors was 0.058 m. Conversely, the RMS and MAV of the validation GCPs were 0.095 m and 0.084 m, respectively. A summary of the validation GCPs is shown in Table B- 1. The average errors for both the sets of GCPs and the overall set were less than 0.1 m, which was thought to be an acceptable threshold for the level of error due to the coarseness of the bed.

Table B- 1 Projection error between measured and estimated elevations of the validation GCPs

GCP	Measured elevation (masl)	Agisoft estimated elevation (masl)	Error (m)
1	194.205	194.250	0.045
7	193.679	193.811	0.132
14	194.175	194.186	0.011
18	193.821	193.930	0.110
19	194.515	194.385	-0.130
24	194.533	194.457	-0.076

A dense cloud with over 32,000 points was generated using the medium quality and aggressive filtering settings, following guidance from Helm et al. (2020). The dense cloud was exported from Agisoft and imported into Cloud Compare, a point cloud processing software, where the Cloth Simulation Filter (CSF) (W. Zhang et al., 2016) was applied to remove the influence of vegetation

obstructing bed points. Initially developed for treating LiDAR point clouds, the tool inverts the point cloud and drapes a simulated cloth over the inverted cloud, which allows it to smooth out the terrain and remove topographic sinks in the inverted surface (i.e., peaks in the original point cloud), making it effective for removing overhanging vegetation that were obstructing bed points (Helm et al., 2020). The cloth resolution was set to 0.1 m, while the classification threshold was set to 0.35 m. The use of a lower number was found to inadequately filter the vegetation points, while higher values were found to remove the top of protruding boulders.

Another check was completed again at this step by comparing the point cloud with the actual GCP coordinates. The estimated and measured coordinates were imported in Cloud Compare as separate point clouds. The elevation of the nearest point to each projected GCP coordinate was recorded to calculate the error between the processed model and the actual locations. The Align Point Cloud tool was then employed to realign the point cloud model with the measured coordinates by setting the measurements as the reference point cloud and enabling scale updating. The improvements to the projection for the validation GCPs are shown in Table B- 2.

Table B- 2 Projection error for the validation GCPs

GCP	Original Agisoft error (m)	Post-CSF error (m)	Post-alignment error (m)
1	0.045	0.037	0.033
7	0.132	0.148	0.129
14	0.011	-0.015	-0.001
18	0.110	0.071	0.104
19	-0.130	-0.108	-0.080
24	-0.076	-0.107	-0.081

Appendix C
Initial model development and formulation

C1) Model mesh and bathymetry

The initial study area comprises of a 550 m reach bounded by Muchalat Lake on the upstream end and 100 m downstream of the power line. The bounds of the model domain were set based on available ADCP data, with the upstream bound delineated along transect 002 from EFT1. The upstream and downstream domains are shown in the following figure.

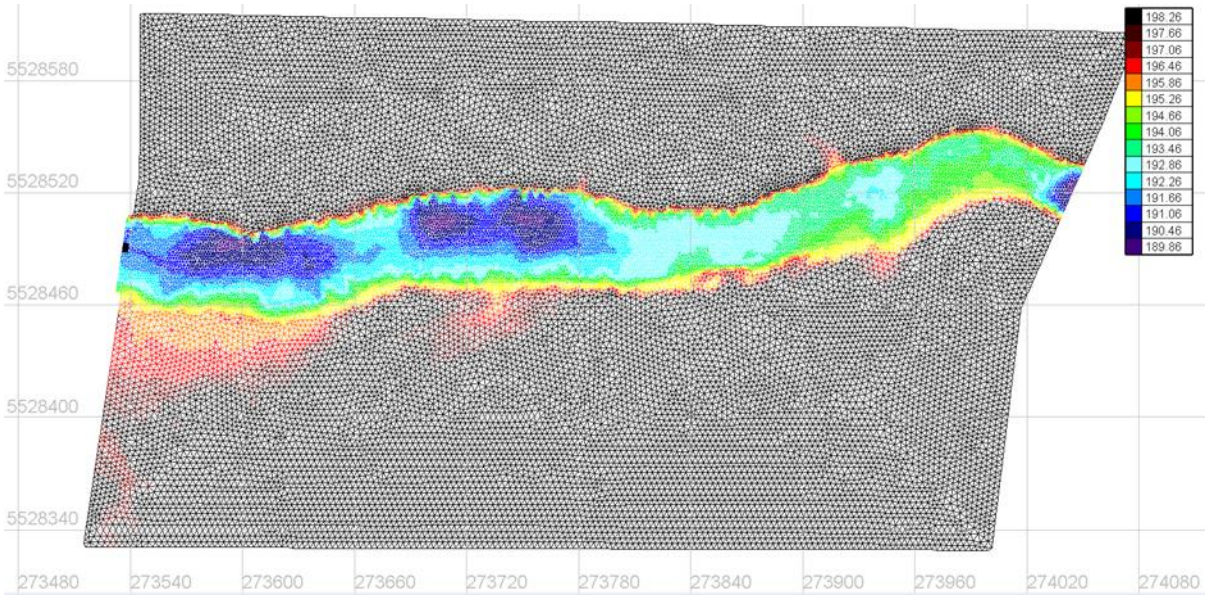


Figure C- 1 Interpolated bathymetry in Blue Kenue (values in masl)

C2) Downstream boundary condition

The stage at the downstream boundary condition was determined by curve-fitting water surface elevation profiles between the two gauges during the three field trips. It was assumed that the water surface would follow an M2-M2 profile between the two gauges, as described by Chow (2009). The M2-M2 profile is a convex downstream water surface profile curve that occurs as the channel transitions from a milder slope to a steeper mild slope.

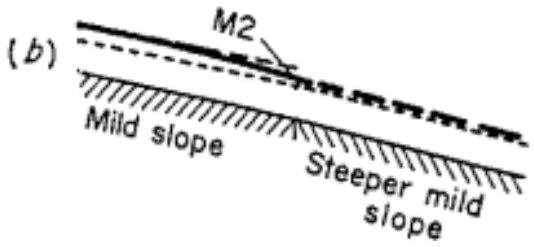


Figure C- 2 M2-M2 curve. From Chow (2009), fig. 9-6.

A sigmoid curve (i.e., an S-curve) was fit to the available WSE data at the benchmarks for the three field trips. The sigmoid Emax model was adopted as it provided a greater number of coefficients with which to calibrate. This model is represented by:

$$f(a) = a_{min} + \frac{(a_{max} - a_{min})a_{50}^{n}}{a_{50}^{n} + a^{n}} \quad \text{[C- 1]}$$

where a_{min} and a_{max} respectively represent the lower and upper horizontal asymptotes, a_{50} is the a-value corresponding to the inflection point of the sigmoid and the midpoint between the asymptotes, and n is the Hill parameter controlling the steepness at x_{50}.

As the downstream gauge cannot be assumed to represent normal depth at high flows, an additional parameter was introduced to shift the lower horizontal asymptote downwards to a lower depth. The water surface elevation at the downstream boundary was thus related to the gauge rating curves by:

$$Z_{BC} = Z_{Solinst} - \Delta H + \frac{\left(Z_{Pacfish} - Z_{Solinst} + \Delta H\right)s_{infl}^{n}}{s_{infl}^{n} + s^{n}} \quad \text{[C- 2]}$$

where ΔH is the vertical shift applied to the downstream gauge, s is the streamwise distance along the centreline (m) and s_{infl} is the position of the inflection point along the streamwise axis (m).

The inflection point, vertical shift and Hill parameter were used to manually calibrate curves between the two gauges based on the measured WSE near the benchmarks. The adopted parameters are presented in Table C- 1 and the curve-fit for the calibration scenarios are plotted in Figure C- 3.

Table C- 1 Curve fit parameters for the sigmoid Emax model applied to the EFT WSE profiles

Field trip	S_{inf} (m)	ΔH (m)	n
EFT1	560	0.05	9
EFT2	440	0.005	9.1
EFT3	720	1.35	6.2

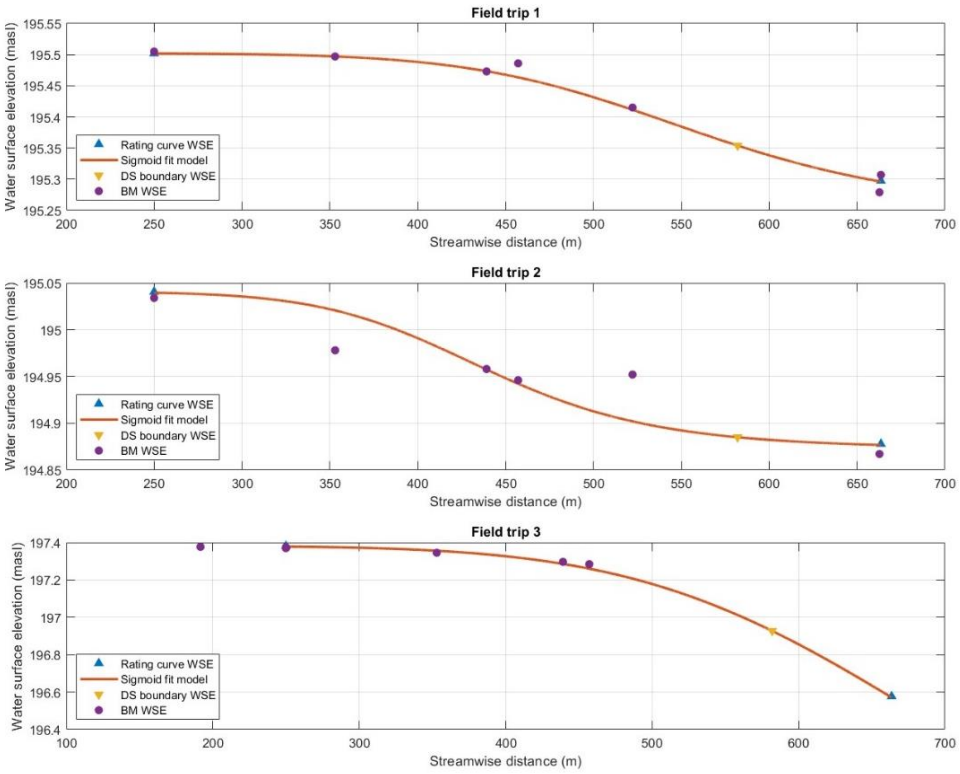


Figure C- 3 Curve fit of the sigmoid Emax model the BM WSE profiles from each field trip.

Although the curve fit reasonably well for FT1 and 3, the curve did not fit as well for FT2 due to the relatively shallow variation in the WSE profile. Nonetheless, fitting the FT2 with a straight line only resulted in a ~2 cm difference with the sigmoid and a negligible difference in the model results, thus the sigmoid model was still applied for this flow to facilitate extrapolation to other design flow scenarios. Each of the calibration parameters were related to the discharge through fitted power law or logarithmic equations and plotted in Figure C- 4.

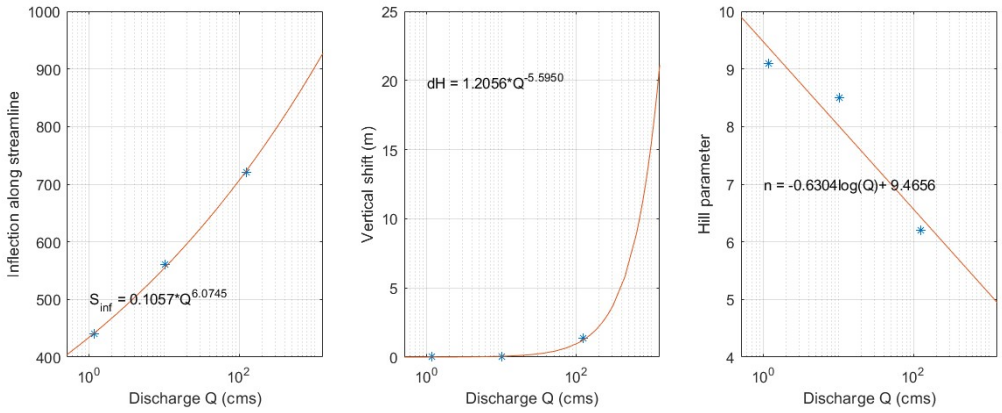


Figure C- 4 Power law or logarithmic fits for the sigmoid curve calibration parameters.

These equations were used in conjunction with the sigmoid equation to generate WSE profiles for each of the design flow scenarios (Figure C- 5). These curves were compared with the stages calculated from the rating curves at each design flow rate. The profiles show a 10 cm difference with the calculated stage at the downstream gauge for the 2- and 10- year flows, but otherwise differs from the downstream gauge by less than 5 cm, indicating that this method yields an adequate fit for the tested scenarios. The boundary conditions for each design flow are presented in Table C- 2.

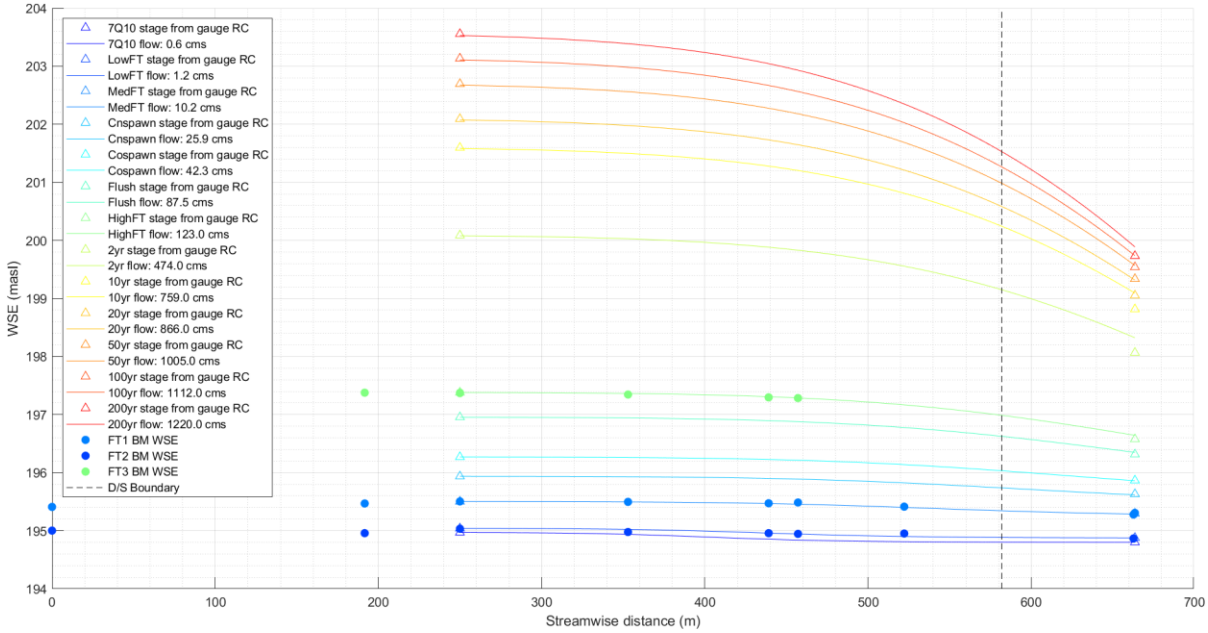


Figure C- 5 Interpolated water surface profiles (lines) plotted alongside the WSE at the gauges (triangles) and benchmarks during the three Ecofish field trips (circles).

Table C- 2 Boundary conditions for all design flow scenarios.

Flow scenario	Upstream boundary flow rate (m^3/s)	Downstream boundary stage (masl)
7Q10	0.55	194.80
LoFT	1.17	194.89
MeFT	10.2	195.34
Cnspawn	25.9	195.74
Cospawn	42.3	196.03
Flush	87.5	196.62
HiFT	123	196.98
2yr	474	199.11
10yr	759	200.17
20yr	866	200.50
50yr	1005	200.88
100yr	1112	201.15
200yr	1220	201.40

This method is subject to significant error and is not well-supported in literature through other studies. For the higher design flows, a steep water surface profile is present in the downstream section due to the increasing difference in calculated stages from the rating curves. This profile is highly dependent on the accuracy of the rating curve equations, which is limited by the short length of record from the gauge stations. Imperfect or unrealistic fitting of the calibration parameters also creates further uncertainty; however, it was a best guess of the field conditions for the initial model runs.

Appendix D
Gravel placement scenario

D1) Modeling bed rise

Placing a layer of gravel in the channel creates a bed rise over which velocity may increase and depth may decrease, particularly if the gravel pad spans the full width of the channel. Evaluating any changes in the hydraulics is therefore necessary to ensure that structural changes to the channel geometry through the design do not incite extensive geomorphic changes. A model scenario based on a proposed gravel spawning pad design that was developed through discussion with Ecofish was tested with the design criteria to evaluate how the stream may respond to the placement. This design was proposed based on preliminary results from the initial model, which had predicted greater gravel mobility than the updated model. Given the uncertain availability of future funding for gravel replenishment in the years following construction, this design was selected based on the need to prioritise the stability of the installation over the other design criteria.

The placement scenario was modeled by raising the bathymetry by 50 cm in separate placement pads with a 10^{o} slope at the edges of each area to transition back to the original bed elevation. The scenario, shown in Figure D- 1, features a raising of the bed over a vegetative bed rise in the upstream lake section and an 80 m stretch in the transition section. The downstream gravel pad was set at the limit of the area predicted by the initial model to experience gravel mobility while having adequate HSI. This pad therefore allows for the immediate benefits to the spawning salmon, as it is also well-positioned to disperse into areas of high HSI further downstream. The upstream pad is expected to remain more stable, therefore creating a longer-term gravel supply that may later travel to suitable spawning areas under higher floods. This scenario reflects approximately 2000 m^3 of gravel, which is the volume budgeted for the project.

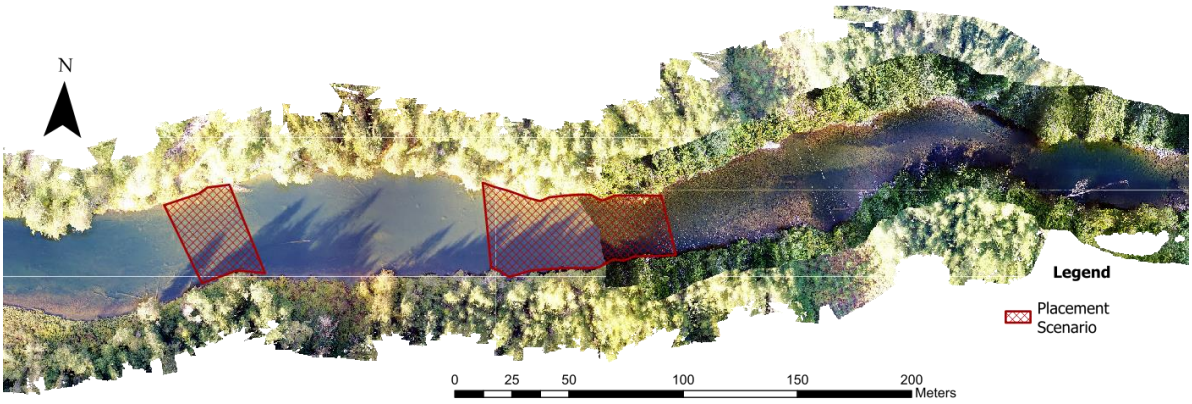


Figure D- 1 Spatial extents of the gravel placement design scenarios.

A polygon shapefile was used to delineate the placement zone, and the Distance Accumulation tool on ArcGIS was used to create a raster where each cell represented the distance from the cell to the polygon. The Raster Calculator tool was then employed to calculate the raised elevation of the placement zone and the sloped elevation surrounding its edges using Equation [D- 1].

$$Z_{placement} = Z_{original} + \Delta Z_{placement} - \frac{D_{accumulated}}{\Delta X} \quad \text{[D- 1]}$$

where $Z_{original}$ is the original topographic raster (masl), $\Delta Z_{placement}$ is the design thickness of the gravel layer (0.5 m), $D_{accumulated}$ is the raster defining the accumulated distance from the placement zone (m) and ΔX is the horizontal distance corresponding to a 10º slope (5.67 m). The final elevation raster was computed using a conditional evaluation, such that the larger of the placement elevation and the original bed elevation would be retained. It was assumed that the placed gravel would not significantly alter the reach-scale roughness value, thus the roughness over the modeled spawning pad was not changed.

D2) Modeling gravel placements in the initial model

The gravel placement design scenarios were modeled in the initial model by increasing the elevation of the bed over the spawning pad locations by 0.50 m as described in the previous section, and updating the roughness values within the placement zone to reflect the roughness of the placed material. For the Chinook and sockeye substrate mixes, the roughness values correspond to 0.25 m and 0.14 m, respectively.

D3) Gravel placement design scenario results for the updated model

The simulation results for the gravel placement scenario with updated bathymetry indicated that raising the bed slightly increases the velocity (and therefore shear velocity) throughout the reach, as shown in Figure D- 2. Consequently, gravel is predicted to be more mobile post-construction, particularly in the transition section. The location of the downstream pad was not expected to undergo significant scour under the 2-year return flow over the existing bed, but the velocity increase over the bedform in the design scenario shows that 1/3 of the pad may erode under this flow. The upstream pad, however, is expected to remain relatively stable under this flow despite the height increase. Conversely, there is little change in the predicted mobility patterns under the 100-year return flow, as the sensitivity of modeled velocity to the prescribed bathymetry is decreased at greater flow depths.

Under the gravel pad design scenario, the flushing mobility of fines and HSI values for Chinook spawning were found to have negligible change from the existing bed scenario despite the predicted increase in gravel mobility. As the proposed locations were developed independently from the updated optimization analysis and do not correspond with the identified optimal areas, the optimization analysis was not repeated for this scenario.

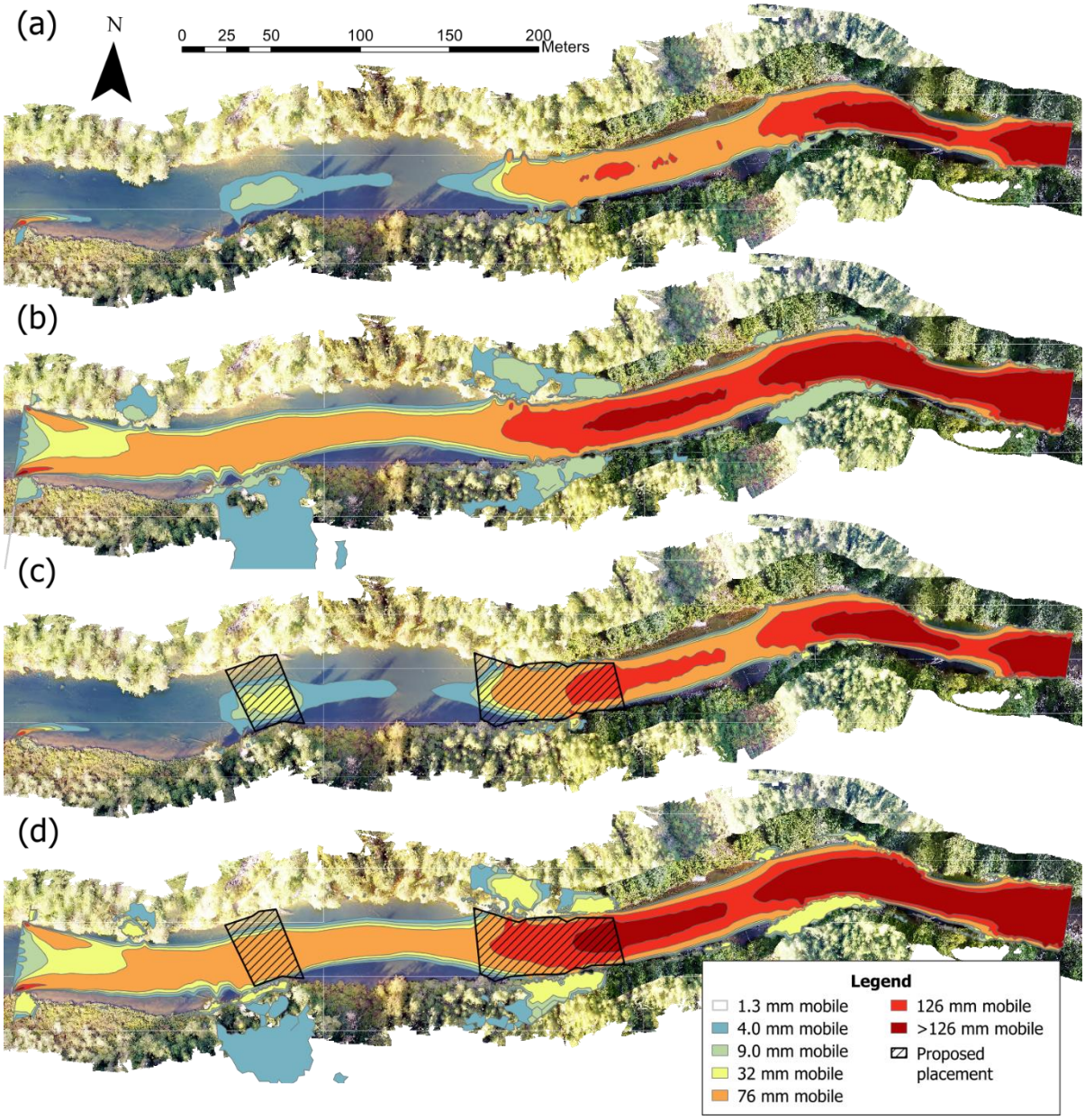


Figure D- 2 Comparison of the predicted mobility patterns for the (a) 2-year and (b) 100-year return flows over the existing bed and the (c) 2-year and (d) 100-year return flows over the bathymetry of the proposed placement.